# NOVEL CONDUCTIVE BIOMATERIALS INSPIRED BY MICROBIAL NANOWIRES

By

Krista Cosert

A DISSERTATION

Submitted to
Michigan State University
in partial fulfillment of the requirements
for the degree of

Microbiology and Molecular Genetics – Doctor of Philosophy

2018

ABSTRACT

NOVEL CONDUCTIVE BIOMATERIALS INSPIRED BY MICROBIAL NANOWIRES

By

Krista Cosert

Model microorganism *Geobacter sulfurreducens* extracellularly respires metal electron acceptors through conductive micron length pili appendages that are homopolymers of a single gene product, PilA. In this dissertation, I investigate the physical and electronic properties of a truncated pilin that retains all amino acids identified as critical to electron transfer, self-assembly and metal binding capacity.

Planar assemblies of recombinant peptides tagged with an amino-terminal (N-t) cysteine provide powerful platforms for investigating the mechanism and metal binding capacities of the pilins. Clustering of aromatic amino acids near the electrode surface mimic clustering in the pilus fiber, mechanistically stratifying electron transfer through the film. Multistep hopping occurs through the N-t region and interchain tunneling in the C-t region, with the aromatics near the electrode surface inducing rectifying behavior. These residues effectively dope the film, promoting electron transfer in the biologically relevant direction at the low voltages operating in cellular respiration.

The tilt angle of the pilins in these planar assemblies leaves the metal trap solvent exposed, making them an excellent platform for the rapid screening of cationic metal binding and reduction. I performed cyclic voltammetry with soluble iron analytes ferricyanide and ferric chloride, to demonstrate metal binding with the natural electron acceptor of *G. sulfurreducens*. The divalent cation, $Co^{2+}$, was investigated with cyclic voltammetry and step potential experiments, undergoing reductive mineralization whose

kinetic behavior is modulated by specific interaction with the pilin film at low scan speeds. These assemblies allow for the rapid screening of cationic metal acceptors that can be bound by the peptide.

The truncated pilins are able to form fibers *in vitro* through a controlled evaporative assembly process that I have optimized. As this truncation removes hydrophobic amino acid residues involved in *in vivo* assembly, it was necessary to provide hydrophobic nucleation sites to form fibers. Efficient access to nucleation sites was achieved via mixing during fiber elongation, producing micron length fibers. The conductive properties of the fibers are examined with conductive probe scanning microscopy, with resistances and electronic substructures similar to those found for native pili isolated from *G. sulfurreducens*. The recombinant nanowires suffered no loss in conductivity after chemical fixation, an important factor for future applications.

Together, these platforms shed light on the molecular mechanisms underlying the function of the *G. sulfurreducens* pilin peptide in the discharge of respiratory electrons to bound extracellular metals. Both planar assemblies and nanowires are able to efficiently assemble *in vitro* under mild aqueous conditions that are attractive for potential applications in bioremediation, sensing, or metal reclamation.

To my Family

# ACKNOWLEDGEMENTS

I would like to thank my friends, family, and colleagues, without whom this document and my graduate school journey would never have been possible.

First, I would like to thank Dr. Gemma Reguera for her guidance, mentorship, and support in making this dissertation come to fruition. You gave me a place to call home and apply the full breadth of my skills on a project I care deeply about. I have learned too many things to list regarding resilience, tenacity, and keeping the passion for science at the center of what we do.

Thank you to my committee members, Dr. Robert Hausinger, Dr. Claire Vieille, and Dr. Mark Worden, for your advice, guidance, and fresh perspectives on these projects over the years.

A special thank you to Dr. Reza Loloee for his expertise and tireless efforts on my behalf. Your encouragement and technical skills have been invaluable in this interdisciplinary project. Thank you for fulfilling all of my unique requests and teaching me new ways to use the AFM.

Thanks to all of the past and present members of the Reguera lab. From the past members, your guidance on prelims and in-depth knowledge of all things Geobacter were nothing short of miraculous. Specifically, I'd like to thank Becky Steidl for being a great source of information and genetic expertise, Mike Manzella whose patience in polishing my prelim presentation I never forgot, and Sanela Lampa-Pastirk for passing her expertise in CP-AFM and extremely potent Serbian Coffee to me. Bhushan Awate, who taught me how to do electrochemistry twice and joined me in my love of football. To

the current lab members, your energy and presence have kept me young and excited for the new directions you are pushing the lab in.

I am indebted to my colleagues on the 6th floor BPS, particularly to the Hausinger lab, your comradery and good humor in the face of my constant invasion of your biologic to elute my proteins and purification advice have been invaluable.

Thank you to Dr. Angelines Castro-Forero for laying the technical foundation of this work, I am proud to have taken this project a step further.

To my best friend Keara Grady, it's been a long time since I lost my luggage on interview weekend, but I wouldn't trade that nickname, or our friendship, for anything. You are an inspiration, my support, my laughter. Thank you for all the ways you've been there with me on this journey.

I would also like to acknowledge the following funding sources for their financial support of this dissertation: the fellowship from Graduate Assistance in Areas of National Need, that supported me for three years, Michigan State's College of Natural Sciences for a DuVall Family Award, a continuation fellowship and a dissertation completion fellowship.

To my parents and family, your support on this winding path has sustained me. From staring at ants in the driveway, to watching nature documentaries, to pushing me to pursue my dreams and my studies, you've stood by me through all of my trials and triumphs. Also, to my cat, who's furry presence always makes my days better.

TABLE OF CONTENTS

LIST OF TABLES

LIST OF FIGURES

# KEY TO SYMBOLS AND ABBREVIATIONS

A, alanine

AFM, atomic force microscopy

Ag/AgCl, silver/silver chloride reference electrode

C, cysteine

CBD, chitin binding domain

CP-AFM, conductive probe atomic force microscopy

CV, cyclic voltammetry

dd$H_2O$, doubly distilled water

*dI/dV*, differential conductance

DTT, dithiothreitol

E, glutamic acid

EDTA, ethylenediaminetetraacetic acid

$E_c$, crossover potential

$E_n$, nucleation overpotential

$E_{pa}$, anodic peak potential

$E_{pc}$, cathodic peak potential

ET, electron transfer

EXAFS, extended X-ray absorption fine structure

F, phenylalanine

GS, *Geobacter sulfurreducens* strain PCA

HOMO, highest occupied molecular orbital

HOPG, highly oriented pyrolytic graphite

*I*, current

$I_{pa}$, anodic peak current

$I_{pc}$, cathodic peak current

IPTG, isopropyl β-D-1-thiogalactopyranoside

IUPAC, union of pure and applied chemistry

LB, lysogeny broth media

LUMO, lowest unoccupied molecular orbital

MALDI-TOF, Matrix-Assisted Laser Desorption/Ionization Time-of-Flight Mass Spectrometry

MD, molecular dynamics

MM, molecular mechanics

PAK, *Pseudomonas aeruginosa* strain K

pSAM, pilin self-assembled monolayer

SAM, self-assembled monolayer

SDS-PAGE, sodium dodecyl sulfate polyacrylamide gel electrophoresis

STM, scanning tunneling microscopy

Tris, tris(hydroxymethyl)aminomethane hydrochloride

upd, underpotential deposition

uSAM, undecanethiol self-assembled monolayer

UV-vis, Ultraviolet-visible

*V*, voltage

Y, tyrosine

# Chapter 1.

# The biology and applications of microbial nanowires

## Background

The genus *Geobacter* is comprised of Gram-negative bacteria abundant in soils and sediments where iron (Fe[III]) oxides are available as electron acceptors for anaerobic respiration. Genes encoding acetate transporters and metabolic pathways for its oxidation are conserved in the genus (1), suggesting a critical role for these organisms in the removal of this fermentation product during organic matter decomposition (2). The oxidation of acetate by *Geobacter* is coupled to the extracellular reduction of iron oxides, a process that requires *c*-type cytochromes of the cell envelope and the assembly of conductive filaments of the Type IVa class (2). Most *Geobacter* genomes encode a great number of *c*-type cytochromes, yet sequence conservation among the genes is weak (1). The genome of the model representative *Geobacter sulfurreducens* (GS) encodes, for example, more than 100 *c*-type cytochromes but only a few of them (e.g., the periplasmic cytochromes PpcA and PpcB) are conserved in other sequenced genomes of *Geobacter* species (1). By contrast, genes encoding the pilin subunit (PilA) and all of the components of the biosynthetic Type IV pilus apparatus are conserved in *Geobacter* and other members of the order Desulfuromonadales (3-5). Furthermore, the *Geobacter* pilin gene is divergent and forms an independent line of descent with pilins from other Desulfuromonadales (4). This is consistent with the absolute requirement of *Geobacter* cells to assemble the conductive pilus appendages during the reduction of extracellular electron acceptors such as iron oxides (4) and the uranyl cation (6). The large quantity of *c*-type cytochromes in these bacteria has been proposed to permit the storage of up to one million respiratory electrons per cell, allowing cells to continue to metabolize the electron donor and generate energy to

support their maintenance metabolism for about 8 min (7). This result suggests that the major role of the many extracytoplasmic cytochromes is to function as a capacitor, accumulating respiratory electrons in the cell envelope and discharging them at the base of the pilus fibers once the filaments make electronic contact with the extracellular electron acceptor (8). The many pilus fibers that are assembled on one side of the cell increase the redox active surface area, promote improved access to the electron acceptors, and in the case of the uranyl cation, also prevent the permeation of the toxic radionuclide and its non-specific reduction inside the cell envelope (8). Critical to these functions is the ability of the pili to retract by depolymerizing the pilins and storing them in the inner membrane in a process energized by a conserved retraction ATPase protein (PilT4) (5). As shown in the model of Fig. 1.1, the retraction of the pili has been proposed to shed the reduced minerals, which remain bound to the fibers, and to allow the recycling of pilins to rapidly synthesize a new pilus fiber for a new round of metal binding and electron discharge (8).

The GS pilus, which serves as model representative for other *Geobacter* pili, is a homopolymer of a single pilin peptide, PilA (6). The PilA pilin is synthesized as a precursor peptide or prepilin carrying the conserved leader sequence of Type IVa pilins (4). As shown in Fig. 1.1, this leader peptide is recognized and cleaved by a dedicated prepilin peptidase (PilD) at the inner membrane. The mature pilin is also *N*-methylated at a conserved phenylalanine in position 1 (F1), a post-translational modification that is critical for alignment during assembly with a conserved glutamic residue in position 5 (E5) of a neighboring pilin at a conserved rise of 10.5 Å (9).

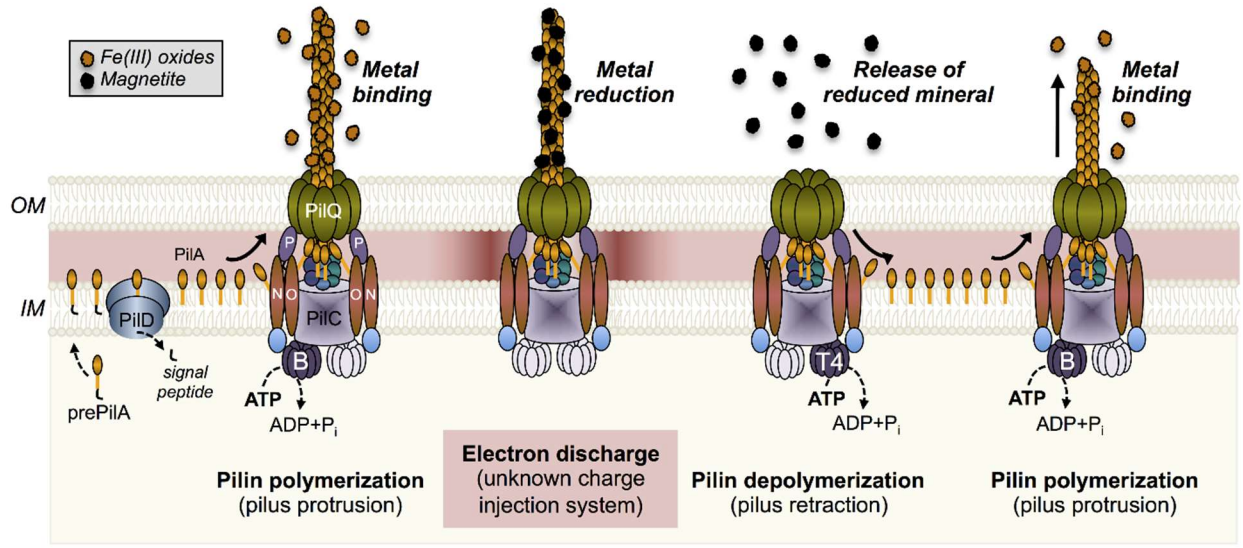


**Figure 1.1:** Steps in the assembly of GS pili during the reduction of iron oxides. The figure illustrates the processing of the prepilin precursor by PilD, the polymerization of the mature PilA peptide by a canonical Type IV pilus apparatus, electron discharge from presumably *c*-type cytochromes of the periplasmic space, and antagonistic cycles of pilus retraction and protrusion to release the magnetite from the pilus and initiate a new round of respiration. This figure is reproduced from open access article (8) under the terms of the Creative Commons Attribution License, which permits use, distribution and reproduction in any medium, provided the original work is properly cited.

Despite conservation of amino acids needed for assembly, the mature pilin is structurally divergent (Fig. 1.2). The most distinctive feature of *Geobacter* pilins is their small size of the peptide compared to other bacterial pilins (4). The structure of the mature GS pilin retains the $\alpha$-helix region ($\alpha$1 domain) that participates in assembly and replaces the conserved globular head of bacterial Type IV pilins with a short carboxy-terminal (C-t) random coil (Fig. 1.2) (10, 11). The predominantly helical structure and a

high concentration of aromatic residues (Fig. 1.2) confer on the GS pilin distinct electronic features that reduce the electron band gap of the peptide and create an environment optimal for charge transport (11).

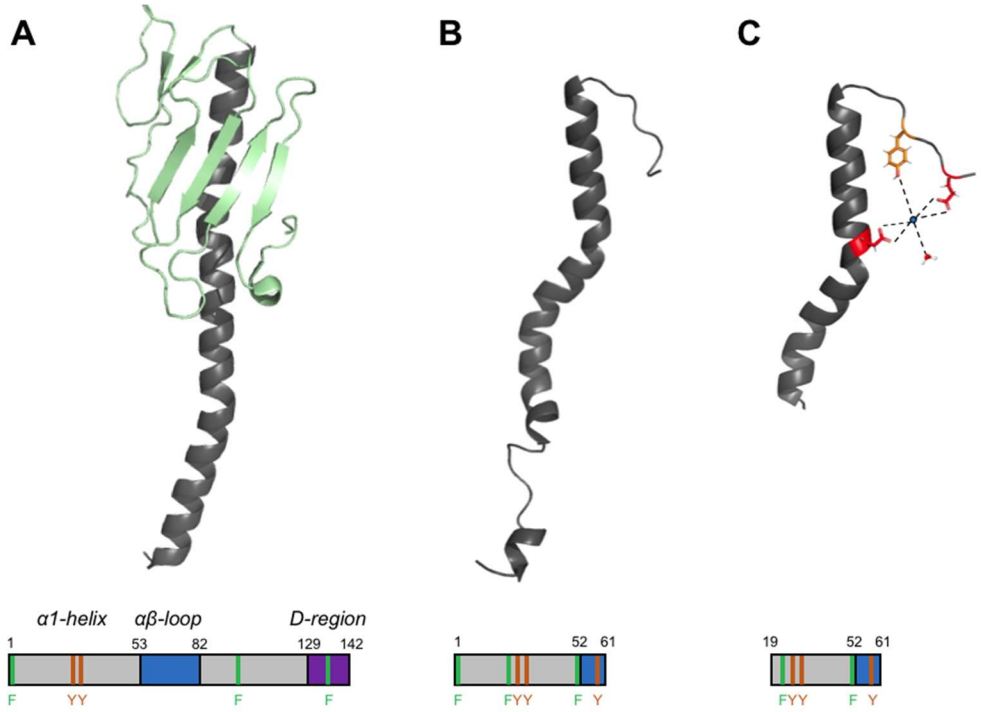


**Figure 1.2:** Molecular structure (top) and domain architecture (bottom) of pilins. The figure shows molecular models of the PAK pilin from *Pseudomonas aeruginosa* strain K (PDB, 1oqw), the GS pilin (PDB, 2m7g), and the truncated GS pilin $PilA_{19}$ generated with Pymol. The bottom panel shows the domain architecture of the pilin and the distribution of aromatic residues (F, phenylanine, in green; Y, tyrosine, in orange). A representation of metal binding is shown in C.

The aromatic residues of the GS pili also cluster during assembly to create paths for axial and transversal conductivity that are predicted to promote fast rates of charge

transport (12). Indeed, an alanine replacement of one tyrosine (Y27) predicted computationally to form half of the aromatic contacts in the pilus fiber increases the electrical resistance along the pilus 5-fold and decreases the pilus conductivity from 4.3 to 0.77 S/cm (13). Furthermore, the charge mobility, which measures how easily charges move through the pilus fiber, is one order of magnitude lower in pili with reduced aromatic contacts (13). The formation of aromatic contacts allows the aromatic side chains of phenylalanines and tyrosines of the pilins to get close together at 3-5 Å distances, but the contacts do not form simultaneously as in a wire (12). Furthermore, some aromatic side chains do not cluster so closely, keeping inter-aromatic distances that can reach 12 Å, and the geometry of the dimer is always displaced (12) (Fig. 1.3). The inter-aromatic distances and geometries of aromatic residues in the GS pilus are optimal for charge hopping, a mechanism of conductance that is only weakly dependent on distance and is thermally activated. Consistent with this mechanism, the conductivity of purified pilus fibers is sensitive to temperature in a way such that freezing the pilus fibers insulates the material at voltages in the $\pm$400 mV range (13). Yet at room temperature individual pilus fibers, purified free of redox and metal cofactors, transport charges at rates near 1 billion electrons per second at the differential voltages (100 mV) between the inner membrane electron carriers and iron oxides that serve as extracellular electron acceptors (13). The pilus charge transport rate far exceeds the almost 10 million respiratory electrons that are discharged by each cell during the respiration of iron oxides (13). This result suggests that pilus charge transport does not limit the rates of cellular respiration. Rather, the need to access and established electronic contact with the dispersed electron acceptors has been proposed to exert

evolutionary pressure for cells to produce several pili on one side of the cell and mechanisms to couple their dynamics (protrusion and retraction) to the rates of respiration (8). Furthermore, the many pili produced per cell also help bind and reduce toxic metals, such as the uranyl cation, extracellularly to mitigate their toxicity (6).

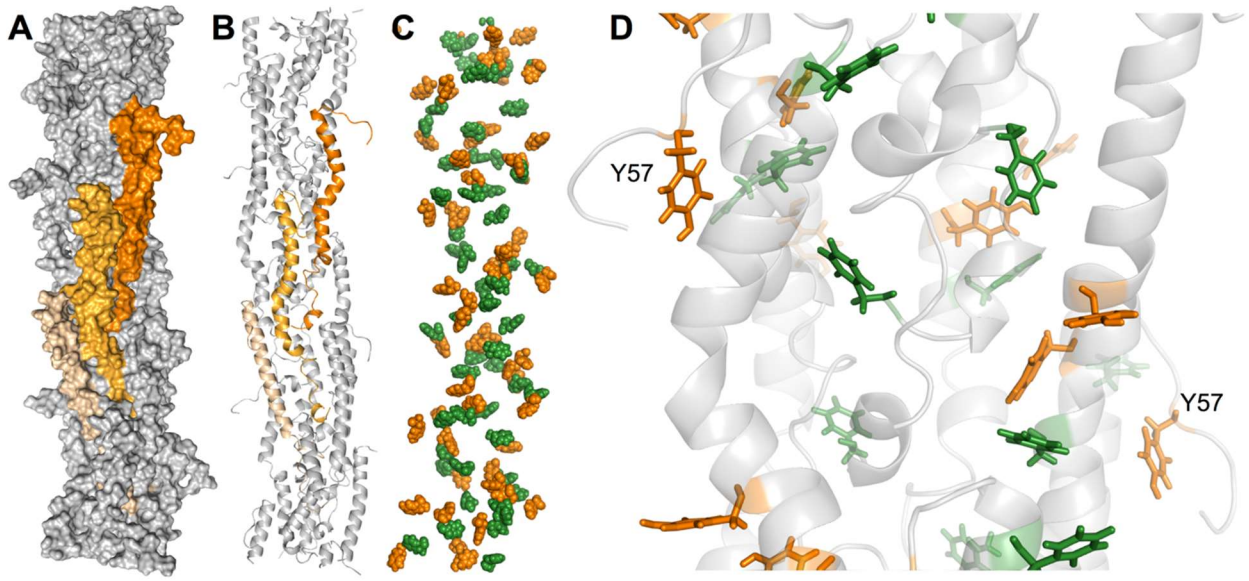


**Figure 1.3:** Computational model of the GS pilus optimized via molecular dynamics showing a surface map with 3 neighboring pilins highlighted (A), molecular structure (B), and aromatic paths (C-D). Tyrosines are shown in orange and phenylalanines, in green). Panel D also labels the terminal tyrosine (Y57), located in the C-t pilin segment. This figure is reproduced from open access article (8) under the terms of the Creative Commons Attribution License, which permits use, distribution and reproduction in any medium, provided the original work is properly cited.

## GS pilins and pili as paradigms in biological electron transfer

*Geobacter* bacteria are to date the only microorganisms known to produce conductive pili, a property that is related to the divergent structural features and unique electronic structure of the GS pilin. Metal-reducing bacteria such as *Shewanella oneidensis* MR-1 were proposed to use a similar mechanism for extracellular electron transfer (14, 15), however, pili sheared from MR-1 cultures are not conductive (4). Furthermore, extracellular electron transfer to iron oxides in this bacterium requires the secretion of soluble flavin mediators (16). It is not widely accepted that the so-called "nanowires" of *S. oneidensis* MR-1 were artifacts of chemical fixation of outer membrane extensions that cells formed by fusing membrane vesicles (17). Chemical fixation collapses the membrane structures and enables conductivity from *c*-type cytochromes embedded in the membrane of the extensions. It has been proposed that these cytochromes could diffuse freely through the membrane and participate in collision-exchange mechanisms and charge transport *in vivo,* but this model has not been demonstrated experimentally (18).

The ability of GS pili to function as protein nanowires offers opportunities to develop novel biomaterials for integration into electronic devices (8). These conductive properties arise from the unique structure of the GS pilin, most strikingly their reduced size (Fig 1.2). The conserved C-t globular domain typical of other Type IVa pilins (Fig 1.2A) is replaced by an 8 amino acid random coil segment (Fig 1.2B). The only conserved structural feature of the GS pilin is the amino-terminal (N-t) α1 domain, which is required for storage of the pilins in the inner membrane and *in vivo* assembly (10-12). Conservation of this reduced structure is apparent in other *Geobacter* species and in

some members of the Desulfuromonadales order (3, 4). This evolutionarily distinct structure makes the pilins predominantly α-helical, a secondary structure that promotes electronic coupling and charge transfer in peptides (19, 20). This helix suggests that the GS pilins are also conductive, a property that could be exploited to develop pilin-based conductive materials (8). Indeed, the helical conformation contributes greatly to the unique electronic structure of the GS pilin, which is predicted promote electron transfer in the peptide prior to assembly (11). Molecular mechanics (MM) simulations of the GS pilin reveal, for example, contributions of five aromatic amino acid residues (three tyrosines, two phenylalanines) to the Highest and Lowest Occupied Molecular Orbitals (HOMO and LUMO respectively) states, which are located in regions of the peptide that align in the assembled fibers (11). These orbitals provide pathways for intra and intermolecular electron transfer. This interaction is supported experimentally by scanning tunneling microscopy (STM), which shows extensive electronic substructures in the conductive pili matching hot spots of conductivity with sizes that could correspond to individual amino acids (21). Type IVa pilins assemble with a 10.5 Å rise (22), forming major and minor groves that align well with the electronic substructures and states near the Fermi level observed in conductive materials (21).

The α-helical structure of the GS pilin is also important to promote the hydrophobic packing of monomers in the assembled pilus, forming a strong but flexible fiber (12). This property could be harnessed to develop biosynthetic platforms that capitalize on the self-assembly of the pilins *in vitro* to manufacture biocompatible conductive materials (8). *In vitro* self-assembly could also enable the synthesis of protein nanowires for various applications. The α-helices of assembled pilins are packed

tightly to form the pilus core, from which the C-t random coils protrude at a 40° bend and are exposed to the environment (Fig. 1.3). The C-t segment is flexible and fluctuates in solution (12). This exposed region also concentrates most of the negative charges of the pilins and exposes carboxylic acid ligands that have been proposed to bind and orient cationic metal species for their reduction by a terminal tyrosine residue (Y57) (Fig. 1.4) (12). The tyrosine and carboxyl ligands match the atomic coordination environment modeled from the uranium $L_{III}$-edge Extended X-ray Absorption Spectroscopy (EXAFS) spectra collected for the uranium mineral that is bound to the pili after the reduction of the uranyl cation *in vivo* (6). This finding suggests that the pilus surface is covered with metal traps that electrostatically coordinate cationic metals for efficient extracellular reduction by respiratory electrons (8). Hence, novel biomaterials can be developed that harness the metal-binding properties of the GS pili for bioremediation of toxic metals and reclamation of cationic metals of commercial value.

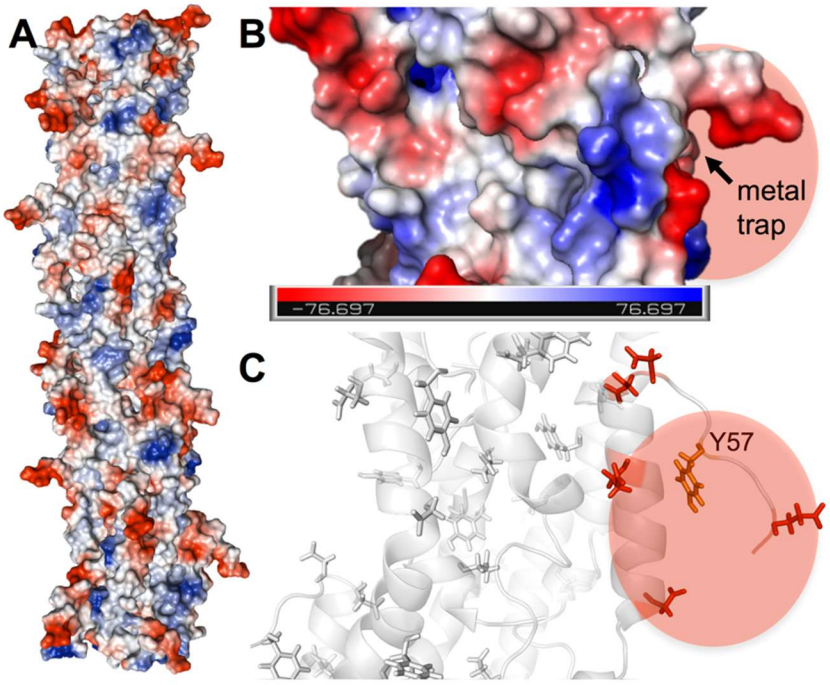


**Figure 1.4:** Metal traps in the GS pilus. (A-B) Computational model of the GS pilus showing electrostatic surface potential (blue, positive; red, negative) and location of the metal traps (B). Color bar in (B), Volts. (C) Molecular structure of the metal trap showing acidic side chains (red) and the terminal tyrosine (Y57; in orange). This figure is reproduced from open access article (8) under the terms of the Creative Commons Attribution License, which permits use, distribution and reproduction in any medium, provided the original work is properly cited.

The *in vitro* synthesis of pilin-based protein nanowires can also advance mechanistic studies of *Geobacter* pili and address controversial studies suggesting that electronic networks of pili could have metallic-like responses to temperature and pH (23). Interpretation of these studies is limited by the use of pili preparations sheared from the cells along with co-contaminants, including *c*-type cytochromes (23). Furthermore, substitutions in the GS pilin can lead to compensatory effects in

cytochrome expression that can skew electronic measurements of pili samples that retain cytochrome contaminants. This, the extensive dehydration of the samples prior to electronic probing, and limitations of the gating experiments used to measure network conductivity have raised concerns about the validity of the conclusions (24, 25). Additional experiments demonstrating ohmic conductance of pili spin-coated onto interdigitated electrodes (26) utilized pili samples hampered by impurities, as indicated by AFM images containing significant 'globular debris' which the authors acknowledge could be *c*-type cytochrome proteins and other cellular material (26). These studies highlight the critical role that sample purity plays in electronic studies, which are needed to characterize the materials' properties of the GS pili and targeted applications. Achieving the level of purity needed for electronic probing is challenging when using bacterial cultures. Lampa-Pastirk *et al.* (13) developed a purification protocol that isolated pili free of redox cofactors and metals. The purity of the pili samples enabled the reproducible measurement of molecular charge transport along individual pilus fibers and the application of genetic engineering to demonstrate the contribution of aromatic contacts to the measured conductivity (13). The purity of the samples also permitted the resolution of the pilus electronic structure with an unprecedented level of detail and the probing of conductivity as a function of temperature (13). These studies demonstrated that pilus conductivity is thermally activated at biologically relevant voltages (±400 mV), supporting an incoherent (hopping or hybrid) mechanism rather than a coherent (metallic-like) mechanism of electron transfer (13). Furthermore, the charge mobility estimated for individual fibers was orders of magnitude lower ($3.2 \times 10^{-2}$ $cm^2\ V^{-1}\ s^{-1}$) (13) than needed to support a mechanism of band conduction, as would be

found in a metallic wire (>1 $cm^2 V^{-1} s^{-1}$) (27). Single molecule probing of pilus conductivity is however limited by the many steps that are needed to purify fibers from biological cultures with the cleanness required for electronics. Moreover, pili yields are often low (in the mg range) and not sufficient for many electronic studies. However, *in vitro* protocols could be developed to mass-produce pilin-based protein nanowires to investigate their conductivity and define applications in electronics. *In vitro* nanowires could also help advance structural studies. With no experimentally verified structure, inter-aromatic distances and specific configurations of aromatic contacts in the pilus have been derived from computational modes constructed on the assumption of structural homology with canonical pilus structures from other bacteria (10, 12, 28, 29). Although none of these models show aromatic geometries that could promote π-π stacking and metallic conductivity, structural information could provide definitive proof to rule out this controversial model. Structural information could also ascertain whether aromatic amino acids, as predicted computationally, cluster in T-shaped geometries optimal for charge hopping (12, 29). These configurations are unsuited for extensive delocalization of electrons, as small displacements of the aromatic ring from the specific π-π stacking geometry can cause significant reductions in tunneling rates (30).

## Objectives and chapter description

The complex and contentious nature of electron transfer in the GS pili requires pure, easily manipulated samples to facilitate mechanistic studies. Isolation of GS pili from the native host, while possible, is a difficult process that relies on anaerobically grown microorganisms. Further, native fibers tend to interact strongly with each other, forming extensive supramolecular structures that challenge controlled integration of the biomaterials into electronic devices for electronic probing and functionalization (13). A system for mass-production could alleviate many of these concerns, while providing a convenient platform for genetic manipulation of the peptide and scalable production of novel biomaterials. As part of a team of investigators comprised of Dr. Rebecca Steidl and Dr. Angelines Castro-Forero, we developed recombinant approaches to produce peptides derived from the GS pilin. Fig. 1.2C shows a recombinant pilin carrying an N-t truncation of 19 amino acids of the GS pilin ($PilA_{19}$), which I used to synthesize planar and fibrous nanostructures described in the next three chapters of this dissertation, as follows:

### *Chapter 2*

This chapter describes the team's effort to develop methods for the recombinant production of a thiolated $PilA_{19}$ peptide and its self-assembly as densely packed monolayers on gold electrodes. I used atomic force microscopy (AFM) to investigate the mechanical properties of the pilin film and developed conductive probe AFM (CP-AFM) methods to describe its hybrid mechanism of conductivity based on the different distance dependence behavior of charge hopping and tunneling. The results described

in this chapter were published in the journal *Physical Chemistry and Chemical Physics* in 2016 (31).

AFM is a powerful scanning probe technique that employs a sharp tip (often with a radius of curvature in the tens of nanometers) suspended on a flexible cantilever to image surface topography. This technique is not limited resolution wise in the same manner as spectroscopic measurements, and facilitates physical interrogation of surfaces, providing information on the mechanical properties such as stiffness, elasticity, and plasticity, which are important when defining the suitability of pilin assemblies for specific applications. CP-AFM, on the other hand, uses a conductive AFM tip to investigate the conductive properties of the surface, collecting current-voltage (*I*-*V*) plots that inform about electron transfer kinetics and that provide mechanistic insights into charge transport through the material. When linked to structural properties, the conductivity of the film under increasing load unmasked a two-step mechanism of electron transfer that is relevant to the pilus fibers as well. Additionally, this study provided experimental evidence supporting the prediction that the structure of the GS pilin has evolved to promote the efficient transfer of electrons (10-12). It also provided critical knowledge needed to understand pilin's self-assembly and established the foundation of a bioplatform to interrogate the metal-binding abilities of the pilus metal traps, as described in the next chapter.

## *Chapter 3*

Planar assembles of thiolated pilins on gold electrodes attach the peptide to the substrate in tilted configurations that are predicted to be maintained by the same salt bridges that align pilins in the pilus fiber (31). This configuration clusters the N-t

aromatic amino acids near the gold substrate, promoting hopping followed by interchain tunneling through the aromatic-free upper stratum of the film (31). This assembly is also predicted to expose the C-t random coil of the pilins to the analyte, concentrating the metal traps on the film's surface. In this chapter, I tested the suitability of this pilin platform to investigate redox transformations of iron metal species (ferricyanide and ferric chloride) that are soluble in both their oxidized and reduced forms and could serve as electron acceptors *in vivo*. I also used this platform to test the hypothesis that the pilus metal traps promote electrostatic interactions with divalent cationic metals for their reductive precipitation. As analyte I chose cobalt chloride ($CoCl_2$), an electron acceptor that is considered too toxic to be reductively precipitated *in vivo* (32). These studies highlight the suitability of the pilin planar platform to investigate the spectrum of metals that could be potentially investigated for reductive precipitation *in vivo* and to develop novel biomaterials for the remediation of toxic metals or the reclamation of precious metals.

For these studies I used cyclic voltammetry (CV, Fig. 1.5), a powerful electrochemical technique for investigating electron transfer reactions at the surface of a working electrode (33). Typically, CV experiments are done in a three-electrode system comprised of a working electrode (where the reaction of interest occurs), a counter electrode (which facilitates the opposite redox reaction as the working electrode and the redox cycling of the chemical species in the analyte), and a reference electrode with a stable, well known potential against which other potentials can be measured. The reference and counter electrode determine the potential that is applied to the working electrode, where the current is measured. The applied potential is swept, starting at a

positive potential and moving towards the negative (forward scan) until one or more cathodic peaks are recorded that inform about the reduction of the species under investigation (e.g., the reduction of $Fe^{3+}$ to $Fe^{2+}$, Fig. 1.5A). The potential is then swept back, from negative to positive (reverse scan) to record anodic peaks, which inform about the reoxidation of the chemical species (e.g., the oxidation of $Fe^{2+}$ back to the soluble $Fe^{3+}$ species, Fig. 1.5A).

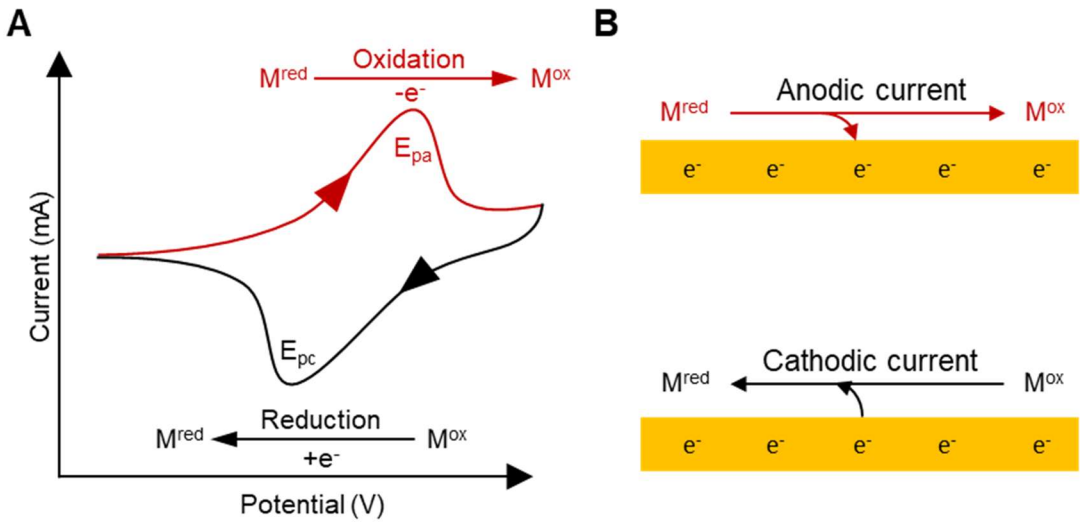


**Figure 1.5**: Cyclic Voltammetry. (A-B) Simplified labeled model of a reversible cyclic voltammogram. (A) Single electron redox reaction of soluble metal species M being reduced in the forward sweep towards negative potentials followed by oxidation as the voltammogram reverses and scans towards positive potentials. (B) Illustration of the redox reaction occurring at the working electrode surface.

The direction of the forward and reverse scans, from positive to negative first and then reversed, follows the International Union of Pure and Applied Chemistry (IUPAC) convention to report CV data as cathodic peaks on the left (low potentials, reduction of the redox species) and anodic peaks on the right (high potentials, oxidation of the redox

species) (33). When scanning to negative potentials, the metal species is reduced at the working electrode surface, resulting in current production and the depletion of the oxidized metal species at the electrode. Current production at the cathodic peak is influenced by the diffusion of freshly oxidized metal to the surface of the working electrode. In its most simple form, reversing the potential will reoxidize the metal species and produce an anodic peak symmetrically opposite to the cathodic peak (Fig. 1.5A). This voltammogram, typical of reversible redox reactions, will have a “duck” shape. In this chapter, I optimized the CV conditions to reproducibly generate “duck” shape voltammograms with bare and pilin-functionalized gold electrodes using potassium ferri/ferrocyanide, a standard analyte for reversible redox reactions (equation 1).

$$Fe(CN)_6^{4-}{}_{(aq)} - e^- \quad \Leftrightarrow \quad Fe(CN)_6^{3-}{}_{(aq)} \qquad (eq.\ 1)$$

With the optized conditions, I then investigated significantly more complex redox reactions mediated by the pilin assemblies and electrochemical features that could unmask specific interactions between the pilins’ metal traps and metals. In the case of the reduction of $Co^{2+}$ to $Co^0$, for example, the low solubility of the elemental $Co^0$ species causes it to precipitate on the electrode surface (equation 2).

$$CoCl_{2\ (aq)} - 2e^- \quad \Rightarrow \quad Co^0{}_{(s)} + 2Cl^- \qquad (eq.\ 2)$$

The $Co^0$ atom then acts as a nucleation site to promote the reductive precipitation of more $Co^{2+}$ from solution and the growth of a layer of $Co^0$ on the electrode surface, which slows the rate of diffusion of the oxidized metal to the surface and decreases the measured current as the scan continues. Larger cathodic peaks are, therefore, expected due to electrodeposition of the metal. The same diffusion limitations also

affect the current measured during the reverse sweep to anodic potentials. As the $Co^0$ layer is slowly reoxidized to the soluble $Co^{2+}$ species, the current diminishes and a crossover with the cathodic peak is often observed before the anodic peak is recorded.

By varying the scan rate, differences between the bare and pilin-functionalized gold electrodes can be revealed that unmask the strength of binding of the metal to the pilin metal traps from the complex voltammogram features caused by first the electrodeposition and then mineral resolubilization (stripping) of the Co metals species. Two types of current are produced in CV, the capacitive current, which is due to ion rearrangement in solution and can be related to working electrode area and scan speed, and the faradaic current, which is a measurement of the redox reactions occurring in the system (33). As the chemical event we are most interested in is the binding and reduction of cationic metals at the metal traps, this chapter includes a detailed description of the cathodic peaks and calculations that reveal information about the kinetics of these reactions. The application of electrochemical methods such as CV to planar assemblies of pilins also allows us to gain insights into its intrinsic conductive properties. For example, when a metal in solution is being reduced, electrons flow from the N-t to C-t of the pilins, and in opposite direction when the metal in solution is being oxidized. This allows us to investigate whether a direction (e.g., the biological direction from the N-t to the C-t) is favored, a behavior termed rectification.

## *Chapter 4*

This chapter harnesses the recombinant pilin biosynthetic platform to manufacture protein nanowires with conductive properties similar to those of the native pili. To accomplish this, I developed a protocol for the *in vitro* assembly of recombinant pilins as fibers that relied on the presence of a non-standard hydrophobe and controlled evaporation to induce fiber formation. The hydrophobe was provided as silica particles functionalized with octadecane, which elute from a reverse phase C18 column during a buffer exchange step that simultaneously resuspends the pilins in assembly buffer. The controlled evaporation step increases molecular crowding to promote efficient nucleation on the hydrophobe 'primer' and fiber elongation to micron lengths.
This relatively simple *in vitro* synthesis contrasts with the biological assembly process, which requires post-translational modifications and a complex protein apparatus spanning the multilayered cell envelope to assemble the pilins (Fig. 1.1). The recombinant pilins used for *in vitro* assembly carry a truncation in the N-t region that is required for biological assembly, but the peptides retain the helical structural and charged residues that are essential for self-assembly and to form salt bridges, respectively. The truncation also increases the solubility of the peptide and enables its recombinant production at high yields once expressed and purified as a fusion protein followed by cleavage.

The *in vitro* methods described in this chapter resulted in high yields of fibers for electronic characterization using scanning probe techniques (CP-AFM and STM) previously used to characterize the conductivity of the native pili (13). STM imaging proved invaluable in identifying fibers with good electronic contact with the underlying

substrate (highly oriented pyrolytic graphite, HOPG) and in conjunction with CP-AFM demonstrated the conductivity of the protein nanowire. We took advantage of the *in vitro* platform to demonstrate that chemical fixation does not affect the conductivity of the protein nanowires, a property that is particularly useful for future device applications. This work has catalyzed a new collaboration with nanotechnologists, who are integrating the protein nanowires into electrode designs to investigate the electronic properties of nanowire networks and other properties of the biomaterial that can be harnessed for various electronic applications.

## *Chapter 5*

This final chapter presents the conclusions of the research I carried out for my dissertation. Here I describe the major findings and I identify aspects of the work that are in my opinion most critical to harness the unique properties of pilins and protein nanowires in biotechnology.

# Chapter 2.

# Electronic characterization of *Geobacter sulfurreducens* pilins in self-assembled monolayers unmasks tunneling and hopping conduction pathways

This chapter was published previously in the journal *Physical Chemistry and Chemical Physics* from the Royal Society of Chemistry. The Society grants permission to the authors to reprint the whole article in a thesis (http://www.rsc.org/journals-books-databases/journal-authors-reviewers/licences-copyright-permissions/).



The material presented in this chapter was generated with contributions from Dr. Rebecca Steidl (genetic engineering) and Dr. Angelines Castro-Forero (optimization of recombinant production). These two authors also contributed to the preliminary optimization of pilin self-assembly on gold electrodes.

## Abstract

The metal-reducing bacterium *Geobacter sulfurreducens* produces protein nanowires (pili) for fast discharge of respiratory electrons to extracellular electron acceptors such as iron oxides and uranium. Charge transport along the pili requires aromatic residues, which cluster once the peptide subunits (pilins) assemble keeping inter-aromatic distances and geometries optimal for multistep hopping. The presence of intramolecular aromatic contacts and the predominantly $\alpha$-helical conformation of the pilins has been proposed to contribute to charge transport and rectification. To test this, we self-assembled recombinant, thiolated pilins as a monolayer on gold electrodes and demonstrated their conductivity by conductive probe atomic force microscopy. The studies unmasked a crossover from exponential to weak distance dependence of conductivity and shifts in the mechanical properties of the film that are consistent with a transition from interchain tunnelling in the upper, aromatic-free regions of the helices to intramolecular hopping via aromatic residues at the amino terminus. Furthermore, the mechanistic stratification effectively "doped" the pilins at the amino terminus, favoring electron flow in the direction opposite to the helix dipole. However, the effect of aromatic dopants on rectification is voltage-dependent and observed only at the low (100 mV) voltages that operate in biological systems. The results thus provide evidence for a peptide environment optimized for electron transfer at biological voltages and in the direction needed for the respiration of external electron acceptors. The implications of these results for the development of hybrid devices that harness the natural abilities of the pilins to bind and reduce metals are discussed.

## Introduction

The fundamental property of all living organisms is energy conservation in reactions that mobilize electrons from donor to acceptor molecules. During respiration, for example, electron transfer (ET) to the electron acceptor relies on the sequential reduction of membrane-bound electron carriers and the simultaneous generation of a transmembrane ion gradient, which provides the energy for ATP formation (34). Mineral-reducing, Gram-negative bacteria such as *Geobacter sulfurreducens* (GS) face unique challenges during respiration due to the insoluble nature (35) and/or toxicity (6) of the electron acceptors. Indeed, these microorganisms can reduce iron and manganese oxide minerals using a complex respiratory system that spans the cell envelope (35). In GS, abundant *c*-type cytochromes facilitate ET across the inner and outer membranes and the periplasmic space formed between the two membranes (35). In addition, the cells synthesize a peptide (the precursor of the GS pilin or PilA), which is proteolytically processed and assembled as a conductive protein filament or pilus by a dedicated protein apparatus spanning the multi-layered cell envelope (4). The pili increase the redox active surface of the cell and facilitate the binding and extracellular reduction of electron acceptors such as iron oxides (4) and the uranyl cation (6). Furthermore, the pili also promote the formation of biofilms and the generation of electrical currents, (9) effectively enhancing the reductive capacity of the cells once embedded into an electrochemically-active matrix of pili and cytochromes (36). GS pili are also dynamic appendages that alternate cycles of protrusion and retraction energized by dedicated ATPase motors (PilB and PilT, respectively) of the pilus apparatus (5, 9). The coordinated cycles of polymerization and depolymerization recycle

the pilins in the inner membrane and enable repeated discharges of electrons onto the extracellular electron acceptors (5).

A structural model of the GS pilus refined by Molecular Dynamics (MD) identified on its surface pockets of acidic residues that could function as metal traps (12). The coordination of these carboxyl groups matched well the atomic environment of pilus-bound uranium modelled from the Extended X-ray Absorption Fine Structure (EXAFS) spectra (12). The electrostatic interactions between the acidic side chains of the metal traps effectively bind the metal acceptor close to the pilus surface to facilitate its reduction (12). The MD model also predicts the clustering of aromatic side chains in the pilus fiber and the formation of axial and transversal paths for ET (12). Indeed, the aromatic residues are required for optimal charge transport along the pilus fiber (13) and for metal respiration (12). The predominantly $\alpha$-helical conformation of the GS pilin (11) also allows for tight, hydrophobic interactions between neighbouring helices in the assembly, reducing inter-aromatic distances and promoting the formation of aromatic dimers with geometries optimal for multistep hopping (12). Consistent with this model, scanning tunnelling microscopy demonstrated the thermal dependence of incoherent conductivity at the low voltages that operate in biological systems (13).

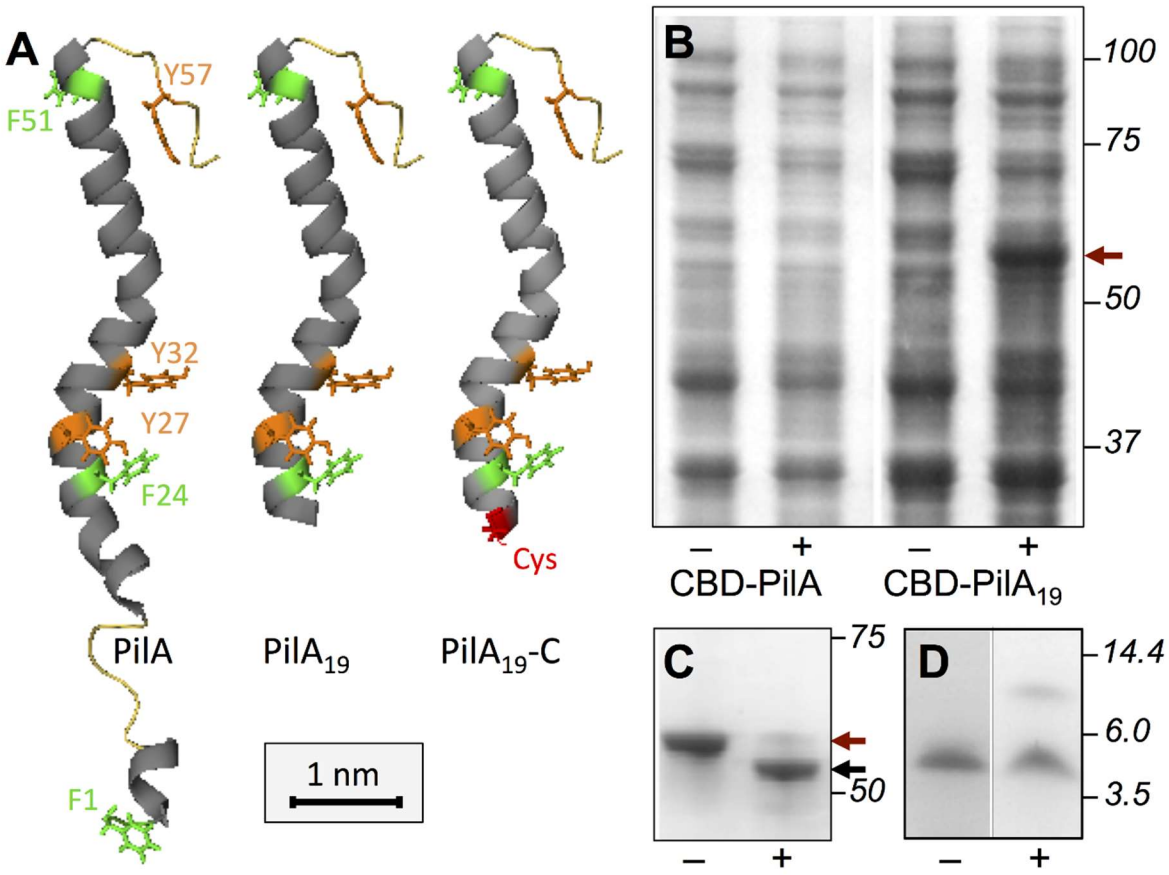


**Figure 2.1**. Structure (A) and recombinant expression (B-D) of PilA, PilA19, and PilA19-C. (A) Pilin structure showing phenylalanines (green), tyrosines (orange) and/o cysteine tag (Cys, in red). (B) Recombinant expression of CBD-PilA19 (red arrow), but not CBD-PilA, upon IPTG induction (+). (C) Column-bound CBD-PilA19 and CBD module (red and black arrows, respectively) before (–) and after (+) DTT treatment. (D) Recombinant PilA19 (–) and its thiolated form PilA19-C with cysteine tag (+) eluted after in-column DTT treatment. Numbers at right in B-D are molecular weight standards in kDa.

In addition to intermolecular aromatic contacts, the pilus' multistep hopping pathway contains intramolecular contacts between three (F24, Y27, and Y32) of the six aromatic residues of the GS pilin (Figure 2.1A) (12). Replacing just one of these

residues (Y27) with an alanine reduced the pilus' aromatic contacts in half and its conductivity, more than five-fold (13). Intramolecular charge transport in the GS pilus is also predicted from the pilin's reduced size, the absence of a globular head with β-strands, and the predominantly α-helical conformation of the peptide (19, 20, 37). The amide groups of a peptide's α-helix can, for example, mediate charge hopping (38, 39). Electron tunneling can also be promoted in helical peptides depending on the coupling strength of bonding contacts, such as covalent bonds and H-bridges, and by through-space jumps (40). The contribution of electron tunneling to protein ET depends on the degree of electronic coupling, which, in turn, is influenced by the protein's structure and dynamics (41) and is predicted to be high once the pilins assemble (11, 12). Interchain electron tunneling provides, for example, the fastest path for ET in well-ordered self-assembled monolayers (SAMs) of helical peptides, which, like the GS pilus, (12) pack the helices close to each other and at a tilt angle (42).

Tunneling and hopping mechanisms can also operate concomitantly to overcome the distance limitation (~2 nm) imposed by the tunneling regimes (43). The two mechanisms can be differentiated by their distance dependence, which is exponential in tunneling but only weakly dependent on distance in hopping (41). As a result, tunneling is limited to short (<2 nm) bridges and a crossover to the hopping mechanism is observed for longer distances (44). Thus, for the GS pilin, which is structured as a bent helix approximately 7.5 nm tall (Figure 2.1A), tunneling and hopping regimes may act coordinately to mechanistically stratify the peptide. Hopping regimes are predicted to operate in the aromatic-rich region at the pilin's amino-terminus (N-t). However, tunneling regimes could prevail in the upper, aromatic-free regions of the helices closer

to the carboxy-terminus (C-t). The rates and directionality of the pilin's electronic pathways could also be influenced by the helix dipole. The vertical alignment of peptide bond dipoles in $\alpha$-helices generates an electrostatic potential that accelerates ET from the more electronegative C-t to the more electropositive N-t (45). The concentration of acidic residues at the pilin's C-t (11) is predicted to strengthen the dipolar moment along the pilin's helix axis. This, in turn, could control the rates and directionality of ET (46). Based on these considerations, we investigated the conductive properties of GS pilins in confluent, pilin self-assembled monolayers (pSAMs) fabricated on a planar gold substrate. For these experiments, we genetically engineered a thiolated pilin derivative that retained the structural and redox features that are critical to charge transport in the pilin assembly (11, 12). Using atomic force microscopy (AFM) methods, we demonstrate the conductivity of the pilin assembly and provide evidence for a two-pathway model involving tunneling and hopping regimes. We also demonstrate voltage-dependent rectification that allows the GS pilin to conduct electrons against the natural helix dipole at the low voltages (~100 mV) that operate in the cell environment. This allows the pilin to transport charges towards the peptide's C-t region, where metal binding and reduction occurs (12). The implications of these findings for the development of pilin-based electronic devices and their use in the bioremediation of metals are discussed.

## Materials and methods

### Bacterial strains and culture conditions

*Geobacter sulfurreducens* strain PCA was routinely grown in NB medium (47) with 20 mM acetate as electron donor and 40 mM fumarate as electron acceptor to provide cells for genomic DNA extraction, using protocols described elsewhere (47). The *Escherichia coli* strains used for genetic manipulations and recombinant expression of pilins and thiolated pilins, and the culturing conditions used for their growth are described below.

### Molecular visualization

The pilins' structural models were constructed with the MacPyMOL: PyMOL v1.8.2.2 software enhanced for Mac OS X (Schrödinger LLC) using the MD-optimized structural model of the PilA pilin (pilin-WT.pdb) reported elsewhere (12).

### Recombinant expression of full length and truncated pilins

The IMPACT$^{TM}$-CN system (New England Biolabs) was used to fuse a chitin-binding domain (CBD) with an intein linker to the N-t region of the PilA peptide or truncated derivatives ($PilA_{19}$ and $PilA_{19}$-C). The sequence of the mature PilA (lacking the signal peptide) or truncated pilin ($PilA_{19}$) was PCR-amplified from the *pilA* gene in genomic DNA with a Herculase II Fusion DNA Polymerase (Agilent Technologies). The primers, which carried plasmid sequence with Sap*I* or Pst*I* restriction sites (underlined) for cloning, were: 5'-GGTGGTTGCTCTTCCAACTTCACCCTTATCGAGCTGCT-3' and

5’-GGTGGTCTGCAGTCATTAACTTTCGGGCGGATAGGT-3’ (*pilA*) and 5’-GGTGGTTGCTCTTCCAACGCGATTCCGCAGTTCTCGGC-3’ and 5’-GGTGGTCTGCAGTCATTAACTTTCGGGCGGATAGGT-3’ (*pilA*$_{19}$). The sequence encoding PilA$_{19}$-C was generated by replacing the N-t alanine (codon GCA) in the plasmid-encoded *pilA*$_{19}$ with a cysteine codon (TGC) using the QuikChange Lightning Site-Directed Mutagenesis kit (Agilent Technologies), as described elsewhere (12). The replacement used forward primer 5’-GGTTGTTGTACAGAACTGCATTCCGCAGTTCTCGG-3’ (cysteine codon is underlined) and reverse primer 5’-CCGAGAACTGCGGAATGCAGTTCTGTACAACAACC-3’. The PCR products were gel-purified (Zymoclean™ Gel DNA Recovery Kit, Zymo Research), digested with Sap*I* and Pst*I* enzymes (Life Technologies), and purified again from agarose gels prior to ligation into plasmid pTYBII (previously linearized at the Sap*I* and Pst*I* cloning sites) with the T4 DNA ligase (New England Biolabs Inc.). The plasmid vectors were then transformed into chemically competent cells of *E. coli* DH5α for long-term storage or into competent Rosetta™ 2 (DE3) pLysS cells (Novagen) for their recombinant expression.

*E. coli* strain carrying pTYB11 plasmid or derivatives with cloned peptides were grown to an $OD_{600}$ of ~0.4 at 37°C in 1L Luria Bertani (LB) broth (Sigma) with 100 μg/ml ampicillin and 20 μg/ml chloramphenicol. When indicated, 50 mM of isopropyl β-D-1-thiogalactopyranoside (IPTG) was added to the cultures to induce the expression of the recombinant fusion protein overnight at 16°C. Cells were harvested by centrifugation at 4,000 x *g* for 10 min and the cell pellet was stored at -80°C. Prior to protein purification, the cell pellets were thawed and lysed via tip sonication in lysis buffer (20 mM Tris-HCl,

100 mM NaCl, 1 mM EDTA, 1% CHAPS) before centrifugation (4,000 x *g* for 1 h at 4°C). The supernatant with the cell extract was loaded onto a 40-ml chitin bed (New England Biolabs) equilibrated with 5 column volumes of column buffer (20 mM Tris, 100 mM NaCl, 1 mM EDTA, pH 7.4) before incubation with the cell extracts at room temperature for 20 min to promote the binding of the CBD-fusion protein to the chitin matrix. The column was then washed with 5 column volumes of a buffer containing increasing concentrations of salt (20 mM Tris, 1 mM EDTA, 0.6/1 M NaCl pH 7.4) to remove unbound material. The reducing agent 1,4-dithiothreitol (DTT) was freshly added to a buffer stock to make cleavage buffer (20 mM Tris, 100 mM NaCl, 50 mM DTT, pH 9), and two column volumes were added to the chitin column to induce peptide cleavage for 24 h at room temperature.

After in-column cleavage, the peptide was eluted in 1 ml aliquots using cleavage buffer prepared without DTT. The aliquots with the highest protein content (UV absorption at 280 nm) were pooled together and the resulting peptide solution was incubated with DTT (5 mM) for 1 h at 37°C to break disulphide bonds. The peptide solution was then transferred to an anaerobic enclosure (COY glove bag; $H_2$:$CO_2$:$N_2$ [7:10:83] atmosphere) for buffer exchange in a reverse phase C18 column (3-ml column volume, Waters). The column was equilibrated with 1.7 column volumes of acetonitrile followed by the same volume of dd$H_2O$. Approximately 3-4 column volumes of the peptide solution were passed through the column by gravity flow to promote peptide retention in the column matrix. The column was then washed with 1.7 column volumes of dd$H_2O$ before eluting the peptide with 3.4 column volumes of acetonitrile. The peptide mass was confirmed by MALDI-TOF using a Matrix Assisted Laser Desorption-

Ionization-Time of Flight Voyager-DE Pro-MALDI-TOF mass spectrometry (Applied Biosystems).

**Denaturing polyacrylamide gel electrophoresis (SDS-PAGE)**

Recombinant protein expression and in-column cleavage efficiency from the CBD module was evaluated in 12% Tris-glycine (cell extracts and CBD fusion proteins) or 10-20% Tris-Tricine (pilin peptides) polyacrylamide gels (Bio-Rad). Cell extracts or chitin matrix with bound proteins were mixed with an equal volume of loading buffer (100 mM Tris pH 6.8, 20% glycerol, 8 M urea, 2% [w/v] sodium dodecyl sulfate [SDS], 0.02% bromophenol blue) to solubilize the proteins. The buffer mix was then loaded onto 12% Tris-glycine gels. The gels were run for 30 min at 200 V in Tris-glycine-SDS buffer (25 mM Tris, 192 mM glycine, 0.1% w/v SDS) using a Mini Trans-Blot cell system (Bio-Rad). Proteins in gels were stained with Bio-safe Coomassie (Bio-Rad, Hercules, CA) for 1 h and de-stained in dd$H_2O$ until bands were visible.

Peptides eluted from the column were mixed with a same volume of Tricine sample buffer (Bio-Rad) and loaded onto 10-20% Tris-tricine gels. The gels were run for 120 min at 100 V in Tris-tricine-SDS buffer (100 mM Tris, 100 mM tricine, 0.1% w/v SDS) using a Mini Trans-Blot cell system. Proteins in gels were fixed for 30 min with an aqueous solution of 50% methanol and 10% acetic acid prior to Coomassie staining and de-staining with dd$H_2O$, as described above.

**Fabrication of functionalized gold electrodes**

Gold electrodes (LGA Thin Films, with 150 Å Cr and 1,000 Å Au evaporated onto the surface of silicon wafers) were cleaned with a Piranha solution (70% concentrated sulfuric acid and 30% hydrogen peroxide) for 1 min and thoroughly rinsed with dd$H_2O$ before functionalization with self-assembled monolayers of $PilA_{19}$-C (pSAMs) or undecanethiol (uSAM). Fabrication of pSAMs started with the application of a solution of $PilA_{19}$-C in acetonitrile onto freshly cleaned gold electrodes inside an anaerobic enclosure (COY glove bag) and incubation at room temperature for up to 48 h. When indicated, the gold electrodes were insulated with uSAMs by depositing a solution of 1 mM undecanethiol in ethanol on freshly piranha-etched electrodes inside the anaerobic enclosure for 48h. The excess solution was then removed, and the electrodes were rinsed with acetonitrile or ethanol, dried with $N_2$, rinsed thoroughly with dd$H_2O$ and dried again with $N_2$ prior to AFM analysis.

The deposition of the $PilA_{19}$-C peptides on the electrode was monitored in real time with a research quartz crystal microbalance (RQCM, Inficon) controlled by a RQCM logging data system to detect changes in crystal frequency (*f*) due to the attachment of the peptide's cysteine linker to the electrode via sulphide linkages. Changes in the viscoelastic properties of the adsorbed mass translate in changes in the dissipated energy (*D*), which was calculated from the measured resistance (*R*) with the equation:

$$D = \frac{32 f_f^2 Z_q d_{fq}^2}{\pi} RA \qquad (eq.\ 1)$$

where $f_f$ is the fundamental frequency of the quartz crystal (5 x $10^6$ Hz), $Z_q$ is the acoustic impedance for AT-cut quartz (8.8 x $10^6$ kg $m^2$ $s^{-1}$), $d_q$ is the piezoelectric strain

coefficient for AT-cut quartz (3.1 x $10^{-12}$ $mV^{-1}$), and *A* is the electrode area (34.19 $mm^2$). The RQCM was equipped with a 0.1 ml flow cell and an AT-cut polished sensing crystal, 5 MHz Ti/Au (Inficon). A PHD standard infusion syringe pump (Harvard Apparatus) was used to fill the flow cell with buffer (10 mM potassium phosphate buffer, pH 7.0 with 50 mM $Na_2SO_4$). After equilibration of the crystal, the $PilA_{19}$-C solution was introduced into the flow cell at a flow rate of 0.2 ml/min to monitor changes in the frequency and resistance during the formation of the pSAMs.

**Ellipsometry**

The thickness of the pSAM was measured with an M-44 rotating analyzer ellipsometer (J.A. Woollam Co., Inc.) controlled by WVASE32 software. The incident angle was set at 75° using 44 wavelengths of light between 414.0 and 736.1 nm. The refractive index (*n*) and extinction coefficient (*k*) were assumed to be $n = 1.5$ and $k = 0$, respectively. The pSAM thickness was probed at three spots for each of five electrode samples functionalized with the thiolated pilins.

**Atomic force microscopy**

All AFM analyses were conducted in tapping or contact mode using an Asylum Research Cypher S system equipped with ASYELEC-01 tips. Tip quality was routinely tested in point conductivity measurements on freshly cleaned gold electrodes at 1 nN forces. Topographic images of bare gold electrodes or pSAMs were collected for 500 x 500 nm fields scanned with the AFM tip in tapping mode. When indicated, the thickness of the pSAM was measured using an AFM nanoshaving procedure (48) applied to

SAMs of α-helical peptides immobilized on gold electrodes via sulfide linkages (42). The method applied a high force (50 nN) to the AFM tip during scans in contact mode to remove a 50 x 50 nm area of the peptide film from the electrode surface. Fields approximately 500 x 500 $nm^2$ were then imaged in tapping mode and 5 scan lines were collected before and after nanoshaving. Scan lines from the undisturbed and nanoshaved areas were then compared to estimate the monolayer thickness from the AFM height.

The mechanical properties of four pSAMs were also probed by AFM to determine the average range of tip forces that triggered the transition from elastic to inelastic film deformation (42). A 500 x 500 $nm^2$ field was first scanned in tapping mode to identify a flat terrace at least 50 x 50 $nm^2$. The smaller area was scanned in tapping mode at least five times to minimize drift before rescanning in contact mode at a rate of 1 Hz while applying a tip force of 1 nN. The procedure was repeated while increasing the tip force in 1-2 nN increments (up to 12 nN). The same large (500 x 500 $nm^2$) field scanned initially was then rescanned in tapping mode to control and correct for drift. Line scans were extracted for each of the forces probed and superimposed on to the tapping mode reference scans to estimate changes in film thickness before and after applying the tip force.

Conducting probe AFM (CP-AFM) was used to collect current-voltage (*IV*) plots for pSAMs, and, when indicated, for bare gold or uSAM controls, while applying a bias voltage to the gold substrate. To reduce the effect of surface curvature on peptide secondary structure and packing, the conductive tip was positioned in flat areas of the pSAM. Current flow was then measured at the lowest tip force (1 nN) while applying a

bias voltage (±0.6 V). The tip force was then increased progressively in 1-2 nN increments and without withdrawing the tip between measurements. Five or more *IV* plots were collected for each tip force applied per spot of three pSAMs to account for technical and biological variability. The conductivity of the AFM tip was checked routinely in point measurements on bare gold electrodes at 1 nN, as described above. The ohmic portion of the *IV* plots in the ±0.2 V range was fitted to a linear regression line using the Igor Pro 6 software. The pSAM conductance (in siemens, *S*) was calculated as the inverse of the slope of the linear fit.

The tip-film contact area was also calculated to normalize the conductance values and obtain pSAM conductivity values. The contact area between the tip and the peptide film was calculated using the Johnson-Kendall-Roberts (JKR) model of solids adhesion.(49) The model estimates the radius *a* of the area of the half-spherical contact region between the tip and the film for each tip force applied according to the equation:

$$a^3 = \frac{R}{K}\left[L + 2L_a + 2\sqrt{L_a L + L_a^2}\right] \qquad (eq.\ 2)$$

where *R* is the radius of curvature of the AFM tip (28 nm for the ASYELEC-01 tip); *L* is the applied tip force; and $L_a$ is the adhesive force of the film (7 ± 1 nN; calculated from the jump-off deflection distances in a minimum of ten force curves acquired for each of three random spots probed per pSAM). The effective modulus constant *K* in *eq. 2* is defined by the equation:

$$K = \frac{4}{3}\left[\frac{\left(1-\nu_t^2\right)}{E_t} + \frac{\left(1-\nu_s^2\right)}{E_s}\right]^{-1} \qquad (eq.\ 3)$$

where $\nu_t$ is the Poisson's ratio for the iridium coated AFM tip (0.26); $\nu_s$ is the Poisson's ratio reported for helical peptide samples (0.33); (50) and *E* is the Young's Modulus of the iridium-coated probe tip ($E_t$ = 232 GPa)(51) or the helical peptide sample ($E_s$ = 1.2

GPa) (52). This equation gives the effective modulus (1.8 GPa) of the system and allows the calculation of the radius *a* (*eq. 2*) of the contact area for each tip force.

The asymmetry of the *IV* curves was also evaluated. The current density was first calculated as the current measured under load at ±100 mV and ±600 mV divided by the tip-film contact area calculated as described above. A rectification score was then calculated for each voltage and load as the ratio of the absolute value of current density at positive over negative voltages. A rectification score above 1 corresponds to asymmetric current flow that favours the tip-to-electrode direction (i.e., inward peptide conductivity, from the C-t to the N-t). Similarly, a rectification score of less than 1 indicates that ET from the electrode to the tip is favoured (i.e., outward peptide conductivity, from the N-t to the C-t).

## Results and discussion

### Recombinant production of *Geobacter* pilins

Electrodes functionalized with SAMs of helical peptides are useful *in vitro* systems to study the conductivity of peptides such as the GS pilin, yet require production systems that generate substantial amounts of the pure peptide. Reaching such high yields from GS cultures is difficult because of the limited amount of pili that can be purified from GS cell cultures and the strong denaturation protocols that are required to depolymerize the peptides (6). Recombinant expression systems provide a rapid and inexpensive tool for high-yield peptide production, (53) yet are difficult to apply to helical peptides because their inherent hydrophobicity promotes their aggregation and formation of inclusion bodies in the heterologous host (53). Similar challenges have been described for the recombinant production of other bacterial pilins, even though these peptides carry a large globular head at the C-t that increases their solubility (54) compared to the predominantly helical conformation of the GS pilin (Figure 2.1A). Indeed, the grand average hydropathy (GRAVY) score calculated with the Kyte and Doolittle hydropathy test (55) for the mature PilA peptide (> +0.5) (Table 2.1) is within the ranges reported for some membrane proteins (55). However, the peptide's hydrophobicity was reduced substantially with stepwise truncations of just a few amino acids at the N-t (Table 2.1). Truncations of 19 to 22 amino acids reversed the sign of the GRAVY score, an indicator of hydrophilicity, (55) while preserving all of the aromatic residues of the pilin involved in ET (9, 12). $PilA_{19}$, which carried the least aggressive truncation producing a GRAVY score below the mean score of soluble proteins (-0.4), (55) was chosen for recombinant expression.

To maximize production yields, we designed a recombinant strategy that expressed $PilA_{19}$ fused to a chitin-binding domain (CBD), which functioned as a solubility enhancer and a self-cleavable purification tag (56). As a control, we also expressed a fusion protein of the mature PilA peptide (CBD-PilA). The approach enabled the recombinant expression of CBD-$PilA_{19}$, but not CBD-PilA, upon induction with IPTG and the purification of the fusion proteins in a chitin column (Figure 2.1B). In-column incubation with DTT was used to induce the self-cleavage reaction at the CBD's intein linker and the elution of $PilA_{19}$ in pure form (Figure 2.1C). The migration of the $PilA_{19}$ peptide on an SDS-PAGE gel (Figure 2.1D) and the molecular weight estimated from MALDI-TOF mass spectrometry (MS) analysis (4,592.793 Da) confirmed its predicted mass (4,595 kDa). The method routinely eluted 40 mg or more $PilA_{19}$ peptide from a 1-L culture of *E. coli*. This is more than twice the levels reported for high-yield expression of comparable helical peptides using synthetic methods (57).

**Table 2.1.** Hydropathicity (GRAVY score) of PilA and truncated pilins $PilA_{10}$, $PilA_{19}$, $PilA_{20}$, and $PilA_{22}$. Truncated residues are shown in gray font and aromatic amino acids are shaded. The GRAVY value was calculated as the sum of hydropathy values (positive for hydrophobic residues; negative for hydrophilic residues) of all the amino acids in the peptide divided by the number of residues in the sequence.

| Peptide | Amino acid sequence | GRAVY |
|---|---|---|
| PilA | FTLIELLIVVAIIGILAAIAIPQFSAYRVKAYNSAASSDLRNLKTALESAFADDQTYPPES | +0.510 |
| $PilA_{10}$ | FTLIELLIVVAIIGILAAIAIPQFSAYRVKAYNSAASSDLRNLKTALESAFADDQTYPPES | +0.073 |
| $PilA_{19}$ | FTLIELLIVVAIIGILAAIAIPQFSAYRVKAYNSAASSDLRNLKTALESAFADDQTYPPES | -0.550 |
| $PilA_{20}$ | FTLIELLIVVAIIGILAAIAIPQFSAYRVKAYNSAASSDLRNLKTALESAFADDQTYPPES | -0.607 |
| $PilA_{22}$ | FTLIELLIVVAIIGILAAIAIPQFSAYRVKAYNSAASSDLRNLKTALESAFADDQTYPPES | -0.713 |

**Formation of pilin self-assembled monolayers (pSAMs) on gold**

We used the same recombinant method described above to synthesize a $PilA_{19}$ derivative carrying a cysteine replacement at the N-t alanine ($PilA_{19}$-C; Figure 2.1A) and confirmed its molecular weight by MALDI-TOF (4,632.26 Da) and SDS-PAGE (Figure 2.1D). A quartz crystal microbalance (QCM) was then used to monitor the deposition and self-assembly of the thiolated pilins on the electrode in real time (58, 59). Figure 2.2A shows the changes in energy dissipation observed during deposition due to the strong coupling of the peptides with the fluid and the frequency shift measured after the introduction of the solution containing the thiolated pilins into the flow cell. These shifts reflect changes in the electrode's mass as the peptides attach to the gold substrate. Energy dissipation and frequency then decreased steadily until reaching a steady state after approximately 60 minutes. The kinetics match well those described for other SAMs, which include a fast initial step of chemisorption followed by a slow phase of spontaneous lateral bonding that organizes the monomers as a monolayer (60).

Overnight incubation to allow the pSAMs to mature and stabilize resulted in a film with an average ellipsometry thickness of 3.6 ± 0.9 nm. Incubation for 48 h, the deposition time used for undecanethiol SAMs (uSAMs) controls, did not affect the monolayer thickness (3.7 ± 0.8 nm). This indicates that the pilins self-assembled rapidly to form a stable monolayer on the gold electrode. AFM images of gold electrodes before (Figure 2.2B) or after (Figure 2.2C) pilin deposition for 48 h revealed a confluent, homogenous film on the pilin-treated substrates. Furthermore, the surface roughness of the electrode (measured as the peak-to-valley height standard deviation in 500 x 500 $nm^2$ AFM scans) decreased from 1.6 to 1.01 nm after pSAM formation. Such decreases

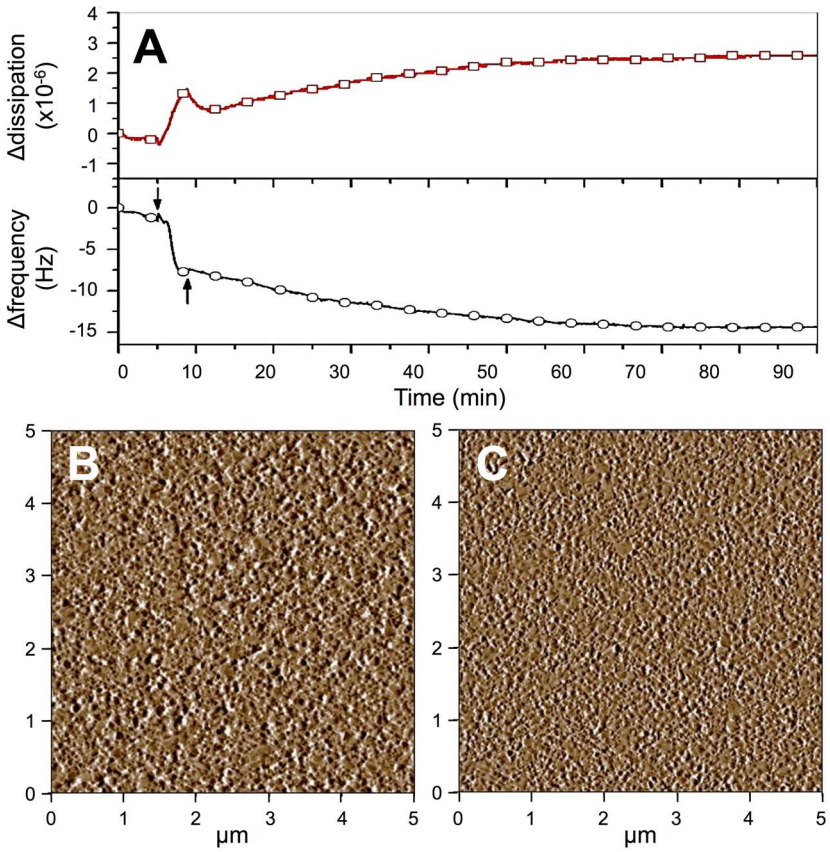


**Figure 2.2** (**A**) Changes in dissipated energy (red plot) and frequency (black plot) of a gold electrode by QCM after the introduction of thiolated pilins into the flow cell (arrows). (**B-C**). AFM tapping mode image (amplitude retrace) of a gold electrode before (B) and after (C) pSAM deposition.

in surface roughness are consistent with a well-ordered, densely packed peptide SAM free of defects or pinholes (61). As a reference, control electrodes covered by a uSAM had a reduced surface roughness of 1.4 nm.

We also subjected flat areas of the pSAMs to an AFM nanoshaving procedure to more accurately estimate their average thickness. Figure 2.3 shows representative AFM scans of a pSAM imaged in tapping mode before and after nanoshaving. The average thickness extracted from 25 scan lines over five different nanoshaved areas was 4.0 ±

0.5 nm, matching well the ellipsometry estimates. This average thickness (4 nm) is about 71% of the length (~5.6 nm) of the $PilA_{19}$-C helix (Figure 2.1A). Thus, the thiolated pilins are not oriented vertically but, rather, are tilted at a 45° angle towards the gold support. This tilt angle is within the ranges reported for SAMs of α-helical peptides immobilized on gold electrodes (42, 62). But unlike most other peptide SAMs, which use short (15-mer or less) synthetic helical peptides, the pSAMs were fabricated with recombinant GS pilins containing a 34-mer $\alpha$-helix. Furthermore, the pilins in the pSAMs also have an 8 residue-long random-coiled segment at the C-t (Figure 2.1A), which does not participate in the self-assembly but remains exposed to the solvent (11).

**Conductivity and mechanical properties of pSAMs on gold**

Electrical transmission across the pSAM was measured while applying a bias voltage (±0.6 V) (Figure 2.4A-B). The current-voltage (*IV*) plots recorded at increasing loads demonstrated current flow through the pSAM even at the low voltage ranges (±0.1 V) that operate in biological systems (Figure 2.4A). Moreover, the electrical response was ohmic, as indicated by the linearity of the *IV* plots in this voltage range. As controls, we also performed electrical measurements on bare gold and on insulating uSAM controls at low (1 nN) forces (Figure 2.4B). Despite the low loading force applied, we measured ohmic electrical currents through pSAMs at 1 nN as well.

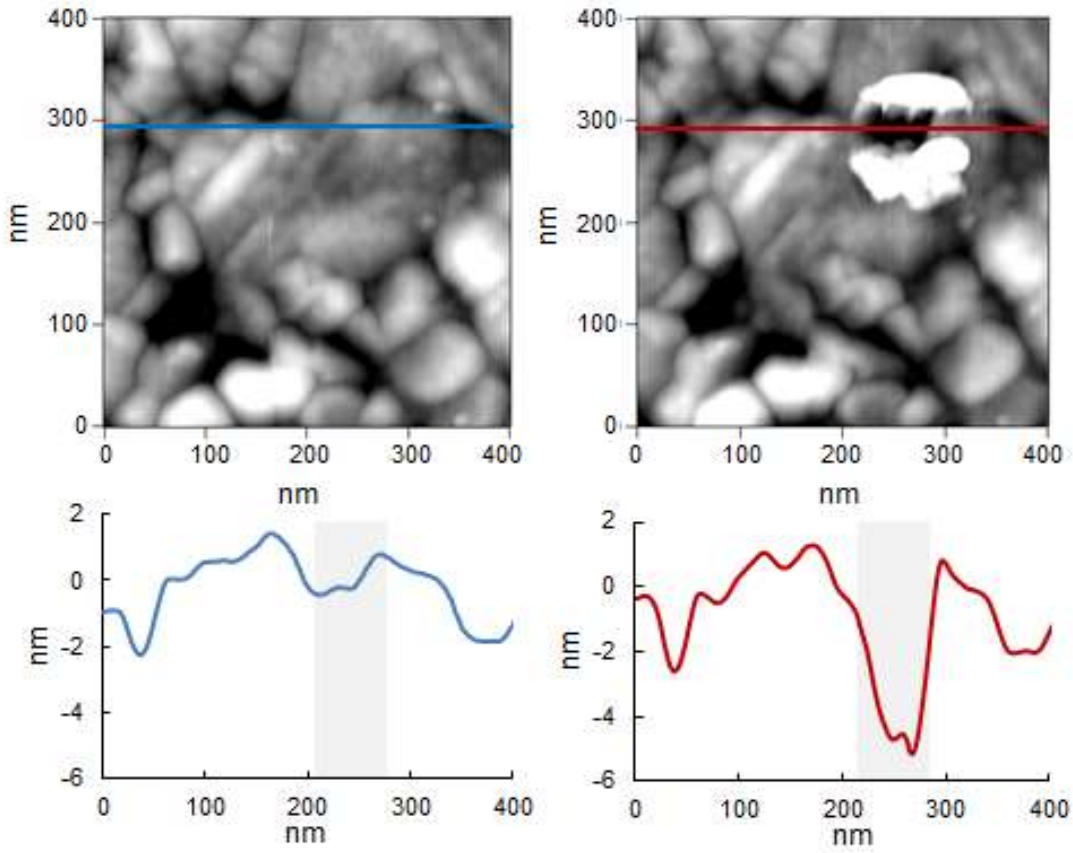


**Figure 2.3.** pSAM thickness by AFM nanoshaving**.** AFM images acquired in tapping mode (top) and cross-section (bottom) of pSAM monolayer before (left) and after (right) nanoshaving. The cross-sectional area shaded in gray points at the region subjected to nanoshaving.

Electrical transmission through the pSAM can be affected by the structure of the peptides, which in turn influences the mechanical properties of the film (42). Thus, we gained insights into the mechanical properties of the pilin monolayer as a function of the tip force applied to the film (Figure 2.4C). Force-induced compression was calculated by comparing the thickness of the pilin monolayer in scans recorded before and while applying a force to the AFM tip. The flexible nature of helical conformations in peptide

SAMs permits considerable elastic deformation under load. This is because, as the loading force increases, the helices tilt closer to the underlying gold substrate until a threshold force is reached that cannot longer be elastically tolerated and triggers a structural transition to random-coiled conformations (42). As expected of compression forces that are tolerated by changes in the helices' tilt angle only (elastic deformation), the pSAM thickness was only weakly dependent on the applied tip force at 1-7 nN (Figure 2.4C). Thus, these are loads that preserve the helical structure of the pilins in the film. However, the film thickness decreased significantly and proportionally to the applied load at > 7 nN (Figure 2.4C). This inflection point marks the transition from elastic to inelastic deformation of the pSAM, when the pilin helices cannot tilt any further and transition to random-coiled conformations (42). As a reference, SAMs formed by shorter helical peptides (15-mer or less) undergo a similar structural transition at loads exceeding 4 nN (42).

The transition from elastic to inelastic deformation at forces above 7 nN also interrupted the force-dependent increases in pSAM conductance, yet only transiently (at 8-9 nN) (Figure 2.4D). This transient behaviour is expected as the helices, or parts of the helices, transition to a more disordered random-coiled conformation. At these loads, the pSAM is still 2.6-3 nm thick (Figure 2.4C). Thus, the inelastic deformation may be limited to the top region of the film only. Further supporting a local inelastic deformation, the pilin peptide is bent in its mid region (Figure 2.1A), a structure that allows the helices to tolerate elastic deformations by tilting their C-t portion only. As the tip force increases (8-9 nN), this C-t region can only tolerate the load by transitioning to a random-coiled conformation, transiently preventing further increases in conductance. Higher forces

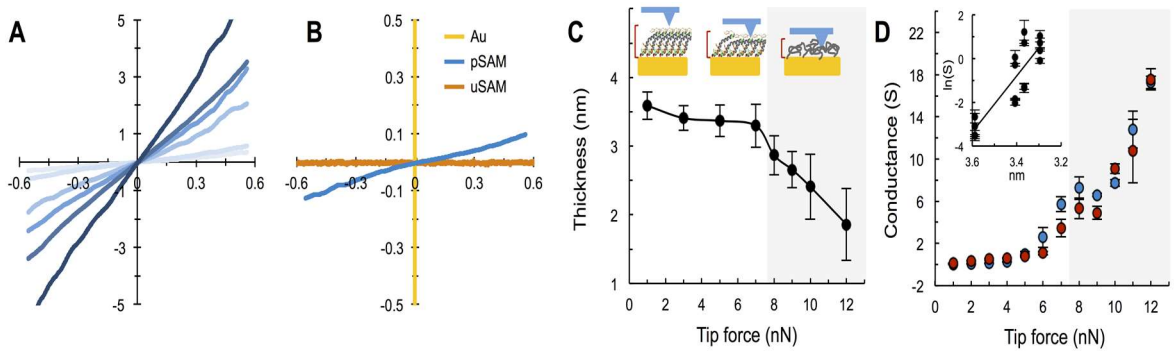


**Figure 2.4.** Conductivity and mechanical properties of pSAMs. (A-B) Representative current−voltage (*IV*) plots of pSAMs probed at loads of 3 to 12 nN (A) or at 1 nN in reference to bare gold (Au) and insulating uSAMs (B). Y axis, current (in nA); X-axis, voltage (in V). (C-D) Thickness (C) and conductance (D) of pSAMs as a function of tip force. Shaded areas show force-induced inelastic deformation of the pSAM, as depicted in the cartoon in (C). Inset in (D) shows the exponential fit of conductance (ln[S]) with pSAM thickness (nm) during elastic deformation in four film replicates ($R^2$=0.75).

compress this inelastic region and/or force the tip to penetrate through it, so force-dependent conductance is recorded again (Figure 2.4D).

**Distance-dependence of pilin conductance in pSAMs**

The distance-dependence of pSAM conductance during elastic deformation (1-7 nN) was also investigated to gain insights into the prevailing mechanism of ET. The increases in conductance at these loads were exponentially dependent on distance (Figure 2.4D, inset), consistent with a mechanism of conductance dominated by electron tunneling (43). From the exponential fit of four replicate films (Figure 2.4D, inset) we calculated a tunneling decay constant of 14.9 ± 5 $nm^{-1}$. This value is within the

upper ranges reported for other SAMs of helical peptides (0.2 to 9.0 $nm^{-1}$) (42, 44, 63-66). However, whereas these other peptide SAMs are less than 2 nm thick, a distance range optimal for electron tunneling, (67) the thickness of the pSAMs under elastic compression is 3.2-3.6 nm. It is unlikely that the dense packing of the pilins in the pSAM permits peptide motions that can provide high enough activation energies so as to cross such a large tunneling barrier. A more plausible explanation is that the aromatic residues at the pilin's N-t (Figure 2.1A) electronically couple the peptides to the underlying electrode. This, and the natural tilt of the helices in the upper C-t region (Figure 2.1A), could effectively reduce the tunneling bridge to its ~ 2-nm vertical span.

As the electrical current that flows through the pSAM can also be influenced by the contact area between the tip and the monolayer, (42) we also calculated the film's conductivity at each tip force. The conductivity values were then plotted against the thickness of the film at each force to unmask distance dependence responses due solely to the mechanism of ET operating in the pilin monolayer (Figure 2.5A). We observed a biphasic response of conductivity to distance (pSAM thickness) with an inflection point at approximately 8 nN (Figure 2.5A). The conductivity plots reproduced the exponential distance dependence at 1-7 nN loads previously observed for conductance (Figure 2.4D, inset), consistent with a tunneling mechanism. Yet they also revealed a transition at > 7 nN to a phase where the conductivity is only weakly dependent on distance (Figure 2.5A), a distinctive signature of hopping regimes (41). At these high loads (> 8 nN), the pSAM has a thickness of about 2.5-3 nm (Figure 2.4C) and has transitioned to random-coiled conformations, at least in the upper region of the film that interacts with the tip (Figure 2.5A, inset). This restricts the helical conformation

to the N-t region of the pilins, where three aromatic residues reside (Figure 2.1A). Inter-aromatic distances in this region promote the formation of intramolecular aromatic contacts critical for multistep hopping through the GS pilus (12). This hopping pathway is also present in pSAMs. Yet the weak distance dependence of conductivity through the hopping path is only unmasked once the upper tunneling bridge has been compressed and deformed sufficiently to directly probe electron transmission between the tip and the aromatics residues (Figure 2.5A, inset).

The results presented above support a hybrid model of conductivity dominated by tunneling in the upper region of the pSAM and by hopping in the N-t region of the pilins' helices (Figure 2.5A, inset). The natural bend of the pilin's $\alpha$-helix in its mid region (Figure 2.1A) could spatially separate the two pathways. Indeed, the C-t region of the helix spans 2.8 nm but is tilted. The vertical drop of the helices in this region at the 45$^{o}$ tilt angle calculated experimentally is ~ 2 nm, which is within the tunneling ranges (67). According to the two-pathway model, electron tunneling through SAMs can involve through-bond coupling (electron tunneling along the molecular backbone) and/or through-space coupling (interchain electron tunneling) (68). The second pathway is favored in well-ordered peptide SAMs because the dense packing and tilted orientation of the helices minimizes interchain backbone separation and provides a shorter vertical path for electrons to tunnel (65). Thus, the initial exponential distance-dependence of pSAM conductivity likely reflects the contribution of interchain tunneling between neighbouring helices in the top, 2-nm thick region of the film. Increasing the tip forces on the pSAM further tilts the helices in this upper region, reducing the tunneling bridge and exponentially increasing the measured conductivity (Figure 2.5A).

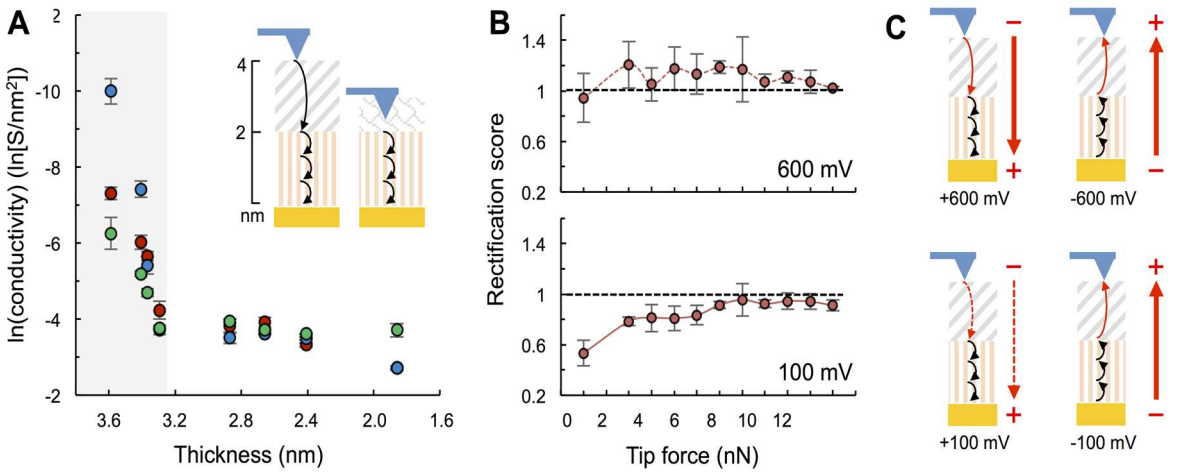


**Figure 2.5.** (A) Force-induced transition from exponential (1, 3, 5 and 7 nN, shaded region) to weak (8, 9, 10 and 12 nN) distance dependence (pSAM thickness) of conductivity. Inset depicts ET (arrows) from the tip (blue) to the underlying electrode (yellow) through the film. Electrons first tunnel through the top stratum of the film (diagonal gray lines, representing tilted helices) and then hop via aromatic residues at the pilins' N-t (vertical orange lines). At higher loads the tip compresses the top stratum and induces random coil conformation (gray wavy area on top), unmasking the multistep hopping path. (B) Representative plot of rectification scores obtained at increasing tip forces at 600 and 100 mV. Shown are average and standard deviation of triplicate pSAMs. (**C**) Cartoons depicting voltage-dependent ET across the pSAM in the inward or outward direction, as indicated by the direction of the arrows. Arrow thickness is used as a proxy of current flow across the pSAM.

Once this top region undergoes inelastic deformation, tip compression unmasks the contribution of aromatic residues at the pilin's N-t (F24, Y27, and Y32) to the measured conductivity (Figure 2.5A, inset). Aromatic residues, particularly if positioned close to the linker, introduce energy levels in the peptide close to the electrode's Fermi level. This

effectively “dopes” the helical peptide and accelerates the rates of ET (69). Thus, the N-t aromatic residues electronically couple the peptide to the gold substrate, creating a short path for multistep hopping. Film compression at high loading forces positions the AFM tip closer to this aromatic region and a crossover from a tunneling to a hopping mechanism is expected. This is observed as a transition from an exponential to weak distance dependence in conductivity (Figure 2.5A).

**Voltage-dependent rectification through pSAMs**

The asymmetry of the *IV* plots was also investigated (Figure 2.5B). For these studies, the current measured at the positive over negative voltage was used to generate a rectification score, which is above 1 in helix-driven peptide systems (i.e., when current preferentially flows from the C-t to the N-t). Asymmetric conductance is often observed in $\alpha$-helical peptides (45). This is because the dipole moments of the peptide bonds are oriented in the same direction along the helix axis, effectively producing a net negative charge at the C-t and a positive charge at the N-t. This generates an electric field along the $\alpha$-helix that can promote the flow of electrons from the more electronegative C-t to the more electropositive N-t. The presence of negatively charged amino acid residues at the pilin’s C-t enhances the dipole moment of the helix (11). The rectification scores at ±600 mV fluctuated slightly above 1 but not strongly and subjected to significant variability (Figure 2.5B). This suggests that helix-driven ET is not particularly strong at these voltages. This result is not unexpected because the tilted orientation of helical peptides in SAMs also tilts the helices’ dipoles and reduces or

suppresses their effect (42). Furthermore, salt bridges form during the assembly of pilins that can reduce the helix dipole and minimize its contribution to ET (11, 12).

In contrast to the symmetry at high (±600 mV) voltages, the *IV* plots extracted at the low voltages that operate in biological systems (±100 mV) were asymmetric. The asymmetry was such that current was higher at -100 mV than at +100 mV when using tip forces (1-7 nN) that preserved the structural integrity of the pilins in the film. As a result, rectification scores at these loading forces were consistently less than 1 (Figure 2.5B). Figure 2.5C illustrates how the mechanistic stratification of the pSAMs can explain voltage-dependent rectification. When a positive voltage is applied to the electrode, electrons flow from the tip to the gold substrate. High enough voltages (±600 mV) provide the activation energy needed to efficiently cross the tunnelling barrier. However, at low, biologically relevant voltages (±100 mV) the activation energy available to overcome the tunnelling bridge is low and current flow in the inward direction is rate-limiting. This effect is not observed during a voltage reversal because the electrons now flow from the substrate to the aromatic-rich region (Figure 2.5C). The aromatic side chains introduce energy levels close to the electrode's Fermi level, reducing the energy barrier required to initiate electron flow (69). As a result, ET in the outward direction is efficient at low and high potentials. Thus, the spatial stratification of the tunneling and hopping regimes controls the directionality of ET at low voltages, favoring the biological (outward) direction.

Local electrostatic effects involving charged amino acids can also influence the directionality of ET (46). Two of the positively charged amino acids of the pilin (R28 and K30) are interspersed with the aromatic residues of the hopping pathway (Table 2.1).

Applying a negative bias voltage to the gold substrate can attract the positively charged side chains and compress the aromatic-rich region at the bottom of the pSAMs, as reported for other peptide SAMs (42). Even slight compressions in this N-t region can reduce inter-aromatic distances and accelerate the rates of electron hopping in the outward direction. Such effects are likely to be masked at high voltages due to the high activation energy available for ET in each direction. However, low voltages unmask their influence on the aromatic dopants and the directionality of ET.

## Conclusions

We used recombinant techniques to produce high yields of a truncated, thiolated GS pilin that retained the ability to self-assemble via hydrophobic interactions while carrying all of the aromatic residues required for efficient ET (Figure 2.1) (12). The hydrophobic nature of the pilin's $\alpha$-helices promoted the self-assembly of the peptides on gold electrodes and the formation of a well-ordered monolayer (Figure 2.2) approximately 4-nm thick (Figure 2.3). The packing of pilins in the pSAM and the tilted orientation of the upper portion of the helices creates a short path for ET in this upper region that is optimal for interchain tunneling (42). Indeed, we demonstrated the exponential distance dependence of tunneling when probing pSAMs under elastic compression (Figure 2.4). At these loads, the upper regions of the pilins tilt progressively, reducing the tunneling bridge to less than 2 nm, a distance optimal for electron tunneling (67). Such tunneling pathway is also expected to operate in the GS pilus fiber, where portions of the helices are tilted and packed tightly (12). This minimizes interchain distance and creates short paths for intermolecular tunneling through the pilin helices.

To overcome the distance-limitation of tunneling, the pilins in the assembly rely on hopping regimes mediated by clusters of aromatic amino acids. The weak distance dependence of electron hopping was revealed in pSAMs probed at forces high enough (> 8 nN) to induce the inelastic deformation of the tunneling bridge (Figure 2.5). This structural transition unmasks the contribution of the intramolecular aromatic contacts located at the pilin's N-t, which are close enough to the gold substrate to electronically connect the peptide to the electrode. These intramolecular aromatic contacts are also

required for charge transport in the GS pilus (13). Furthermore, aromatic contacts also form between neighboring subunits in the pilus fiber that could promote interchain hopping (12). Thus, tunneling and hopping regimes likely alternate in the GS pilus to provide the fastest pathway for ET depending on the local environment. Such hybrid mechanism is analogous to the two-pathway model proposed for 'tour wires' (molecular wires of oligo(*p*-phenylene ethynylene) and derivatives), which transition between tunnelling and hopping regimes at ca. 2.75 nm lengths to maintain the efficiency of charge transport throughout long distances (70).

We also provide evidence for voltage-dependent rectification in the pSAMs (Figure 5B). Asymmetric conductance was only observed at the low voltages (±100 mV) that operate in biological systems. Furthermore, rectification was not helix-driven but, rather, favored the in vivo direction of electron flow from the peptide's N-t to its C-t (Figure 2.5C). The assembly of pilins in the GS pilus orients the peptide subunits in the N-t to C-t direction (12). Thus, pilin rectification at biological voltages promotes the outward flow of electrons from the base of the pilus (N-t) to the electron acceptor, which is bound to pilus ligands exposed at the C-t random-coiled segment of the pilins. The base of the pilus is embedded in the periplasmic space of the cell envelope, a gel-like environment that is rich in *c*-type cytochromes and could directly discharge electrons onto the base of the pili (4). Moreover, the cytochromes can act as capacitors, (7) storing electrons and increasing the differential voltage across the pilus length to promote fast discharges of respiratory electrons. Based on conductivity measurements to individual pili, such discharges could reach one billion electrons per second at 100 mV (13).

The directionality of ET through the pilus could also be modulated by the distribution of aromatic and positively charged residues of the pilin. Aromatic side chains closer to the N-t form intramolecular contacts that effectively dope the peptides and promote the flow of electrons through the tunneling bridges in the upper regions of the helices. The aromatic doping effect can be enhanced by positively charged side chains from neighboring amino acids, which can trigger a voltage-dependent compression of the pilins in this region. This would effectively reduce inter-aromatic distances and accelerate the rate of ET in the outward direction. The flexible nature of the pilus (12) and its dynamic cycles of protrusion and retraction (5) are also predicted to promote electronic coupling. Such dynamics could enhance the doping effect of the aromatic contacts and facilitate through-chain tunneling.

The exposure in pSAMs of the pilin's random-coiled segment also exposes the peptide's metal trap to the solvent. This suggests that the surface of the pSAMs concentrates carboxyl ligands needed for efficient binding of cationic metals, a configuration that could be harnessed to develop biosensors and devices for the immobilization of toxic metals. Furthermore, many cationic metals, such as the uranyl cation that the GS pili bind and reduce, (6) are soluble in their oxidized form but sparingly soluble once reduced. Thus, the metal-binding and conductive properties of the pSAMs could be harnessed to develop hybrid devices for the bioremediation and reclamation of cationic metals.

# Chapter 3.

# Electrochemical characterization of planar assemblies of *Geobacter* nanowire pilins

## Abstract

Extracellular electron transfer in Geobacter bacteria is mediated by conductive protein appendages or pili comprised of a structural divergent Type IVa pilin subunit that has inspired conductive peptide designs for electrode functionalization. Controlled self-assembly of thiolated recombinant pilins is of special significance for bioremediation applications, because the peptides self-assemble as dense films that expose and concentrate the same metal traps that enable the native pili to bind and reductive precipitate cationic metals. Here we apply two electrochemical techniques, cyclic voltammetry and step potential experiments, to investigate the electrochemical properties of films of thiolated pilins on gold and the electron transfer kinetics with cationic metals ($Fe^{3+}$ and $Co^{2+}$) of environmental relevance. We demonstrate the reversibility of redox reactions with iron species (ferricyanide and ferric chloride), in Nernstian fashion, with midpoint potentials of 0.31 V and 0.61 V vs Ag/AgCl, respectively. We also show voltammograms with $CoCl_2$ as the analyte that reveal a complex electrodeposition process, with underpotential deposition occurring near a potential of -0.2 V and -0.5 V, as in bare gold controls, and another around -0.4 V that is unique to the pilin films and is revealed only at slow scan speeds that could facilitate the binding of cobalt atoms to the pilin's metal traps. Step potential experiments were consistent with a diffusion-controlled mechanism of $Co^{2+}$ electrodeposition characterized by three-dimensional growth. Fast binding kinetics and efficient charge transfer promoted cobalt deposition but slowed down the stripping process, making pilin films effective treatments for the reductive precipitation of cationic metals that, like $Co^{2+}$, are too toxic for bacteria to immobilize in vivo.

## Introduction

The hallmark of the physiology of bacteria in the genus *Geobacter* is their ability to discharge respiratory electrons to extracellular metals, both soluble and insoluble, using conductive protein pili of the Type IVa subclass (4, 6). Iron, the natural electron acceptor of *Geobacter* bacteria, is abundant in many soils and sediments as ferric (Fe[III]) oxides, which the pili bind and reduce to solubilize some of the iron as Fe(II) and generate a magnetic mineral (magnetite) of mixed Fe(III)/Fe(II) valence (8). The pili expand the redox active surface of the cell beyond the confines of the outer membrane and allow the cells to access the iron minerals, which are often dispersed in soils and sediments and rapidly transform abiotically into more crystalline and less bioavailable mineral forms. Once the pili bind the iron oxides, the pili function as protein nanowires, discharging respiratory electrons at rates (~9 x $10^8$ $e^-$/s) one hundred times faster than the cellular rates of respiration of the model representative *Geobacter sulfurreducens* (13). This fast rate of discharge ensures that the electron transfer step is not the limiting factor in respiration. The pili also bind the soluble uranyl cation and reductively precipitate it to a mononuclear mineral phase to gain energy for respiration and prevent the permeation of the toxic radionuclide inside the cell (6). To enable repeated rounds of electron discharges, cells alternate cycles of pilin polymerization and depolymerization to grow the pilus prior to metal binding and reduction and to retract it in order to shed off pili-bound minerals (5).

While many studies have focused on how the pili conduct electrons (8), less is known about how the pili bind metals to promote their reduction during respiration. The extended X-ray absorption fine structure (EXAFS) spectrum of pili-bound uranium

revealed an atomic coordination around the pilus-bound uranium atom comprised of two opposite bidentate carboxylate and one distal monodentate tyrosine ligands (6). An atomic resolution model of the pilus of *G. sulfurreducens* optimized via molecular dynamics identified acidic residues on the fibers whose side chains match well with the bidentate and monodentate ligands that trap the uranium to the pilus *in vivo* (12). Anionic ligands form pockets of negative charge on the pilus surface that could function as metal traps, coordinating cations via their carboxylic acid groups in bidentate configurations (12). Some of these ligands reside on a short (8 amino acid long) region at the pilin's carboxy-terminus (C-t), which protrudes from the fiber's core and has the flexibility and exposure needed to facilitate metal binding in solution (12). The C-t random coil also contains the tyrosine at position 57 (Y57) that has been proposed to mediate the last step in electron transfer from the aromatic contacts inside the fiber's core to the extracellular metal acceptor (12). This tyrosine could provide the monodentate ligand that coordinates the uranium atom within the pilus metal traps. In this model, the carboxyl groups of negatively-charged amino acids in the metal traps bind cationic metals with high affinity and position the atom close to the terminal tyrosine to facilitate its reduction (12). Because metal binding is dominated by electrostatic interactions, the metal traps could potentially bind many other cationic metals. If so, *Geobacter* pili may be able to catalyze redox transformations of metals other than iron and uranium cations. For example, *Geobacter* bacteria can reduce soluble species of $Co^{3+}$ to $Co^{2+}$ (71), but the divalent cobalt species is considered too toxic to be reduced biologically (32). Yet the pilus metal traps could coordinate $Co^{2+}$

based on charge and size in the metal trap and reductively precipitate $Co^{2+}$ to $Co^{0}$, effectively immobilizing the toxic metal and preventing its spread.

Harnessing the metal-binding and reductive properties of the pili will ultimately require platforms that enable their mass-production and integration with electronic materials suitable for bioremediation and environmental sensing applications (8). Recombinant pilins are particularly promising because they can be synthesized at high yields in heterologous hosts such as *Escherichia coli* and can be designed with functional tags to functionalize specific materials (31). Thiolated pilins have been designed that are truncated and carry a cysteine tag at the amino terminus (N-t) to enable their recombinant production and targeted self-assembly on gold electrodes, respectively (31). These thiolated pilins spontaneously self-assemble into well-ordered planar films approximately 4-nm thick and reversibly conduct electrons by alternating the hopping of electrons via aromatic contacts with interchain tunneling regimes through the aromatic-void helical portions of the peptides (31). The tight packing of the pilins' $\alpha$-helices on the electrodes is predicted to expose the peptide's C-t random coil, where metal ligands are located, to the solvent (31). The exposure of these ligands suggests that the surface of the pilin films, like the native pilus nanowires, are decorated with electrostatic traps, which could bind and reduce cationic metals with a similar mechanism as *in vivo*. To test this, we electrochemically characterized the catalytic properties of the pilin films via cyclic voltammetry (CV), an electrochemical technique that varies the potential voltage applied to a working electrode to monitor changes in the current measured for a redox reaction. Here we describe the application of CV to demonstrate the reversible cycling of iron species (provided as ferricyanide and ferric

chloride analytes) that can serve as electron acceptors for cellular respiration *in vivo*. We also show electrochemical studies that demonstrate the ability of the pilin films to bind and reductively precipitate the toxic divalent cobalt species as $Co^0$. These studies unmask electrochemical features consistent with the binding of the $Co^{2+}$ metal species to pilin-specific ligands and highlight the suitability of pilin-based molecular assemblies for the development of hybrid devices for the bioremediation and reclamation of toxic cationic metals such as $Co^{2+}$.

## Materials and Methods

### Recombinant expression of truncated thiolated pilins

The recombinant production and purification of a thiolated $PilA_{19}$ derivative ($PilA_{19}$-C) is as described elsewhere (31). Briefly, the truncated $PilA_{19}$-C was expressed in *E. coli* as an N-t fusion protein with the intein linker and chitin-binding-domain (CBD) of the IMPACT$^{TM}$-CN recombinant system (New England Biolabs). For recombinant expression, *E. coli* LB cultures (1 L; 100 µg/ml ampicillin and 20 µg/ml chloramphenicol) grown at 37°C to an $OD_{600}$ of ~0.5 were induced with 50 mM isopropyl β-D-1-thiogalactopyranoside (IPTG) during overnight incubation at 16°C. Cells were harvested, lysed by sonication in 20 mM Tris-HCl buffer (100 mM NaCl, 1 mM EDTA, 1% CHAPS) and centrifuged to collect the clarified lysate, which provided the protein sample with the fusion protein for purification in a chitin column (New England Biolabs) equilibrated with 20 mM Tris (100 mM NaCl, 1 mM EDTA, pH 7.4). Incubation of the chitin column with protein lysate at room temperature for 20 min promoted binding of the fusion protein. A column was with increasing salt concentration (20 mM Tris, 1 mM EDTA, 0.6/1 M NaCl pH 7.4) removed non-specifically bound molecules. Cleavage buffer was freshly prepared by addition of 1,4-dithiothreitol (DTT) to a concentration of 50 mM to 20 mM Tris, 100 mM NaCl, pH 9 and added to the column, which was incubated for 24 h at room temperature to induce the self-cleavage of the recombinant pilin peptide from the intein linker and CBD. The cleaved pilins were eluted from the column with the same buffer sans DTT.

The column eluent was collected in 2 ml aliquots and fractions containing the peptide were identified by UV absorption at 280 nm and pooled together. The peptide

solution was transferred to an anaerobic chamber (Coy glove bag; $H_2$:$CO_2$:$N_2$ [7:10:83] atmosphere) and incubated with freshly prepared 5 mM DTT for 1 h at 37°C to reduce disulfide linkages. The buffer was then exchanged to acetonitrile using a reverse phase C18 cartridge column (3-ml column volume, Waters) inside the anaerobic chamber.

**Self-assembly of thiolated pilins onto gold electrodes**

Pilin self-assembly as a monolayer on gold electrodes was carried out as previously described (31) and used gold electrodes (LGA Thin Films, with 150 Å Cr and 1,000 Å Au on silicon) freshly cleaned with piranha solution (70% concentrated sulfuric acid and 30% hydrogen peroxide). Electrode functionalization was with conductive pilin self-assembled monolayers (pSAMs) of thiolated $PilA_{19}$ pilins ($PilA_{19}$-C) or with insulating 1-undecanethiol self-assembled monolayers (uSAM) and assembly proceeded for 48 h inside a Coy glove bag (31). When indicated, freshly formed pSAMs were rinsed thoroughly with fresh acetonitrile after 48-h assembly and dried before incubation with 1 mM 1-udecanethiol in ethanol for an addition 48 h to cover any dispersed regions of the pSAMs with insulating uSAMs (pSAM-uSAM control). After incubations were complete, all of the SAMs were removed from the glove bag, rinsed thoroughly with acetonitrile or ethanol, dried under a stream of Argon gas and stored in a 6-well cell culture plate in a dark drawer until analyzed with cyclic voltammetry.

**Cyclic voltammetry and step potential experiments**

A conventional three-electrode cell was used to conduct cyclic voltammetry experiments. The working electrode was bare gold or gold electrodes functionalized with pSAMs, uSAMs or hybrid pSAM-uSAM surfaces and the counter electrode was a platinum wire. The third electrode was a 3M Ag/AgCl reference electrode. The redox analytes (1 mM $K_3Fe(CN)_6$, 10 mM $FeCl_3$, and 10 mM $CoCl_2$) were dissolved in a 20 mM tris-HCl buffer with 100 mM NaCl at pH 7. Experiments were performed aerobically using a potentiostat (Bio-Logic USA, VSP model) connected to a lab computer equipped with the EC-Bio labs software for data acquisition. Individual voltammograms were then analyzed with the Igor Pro 6 software, which was used to estimate peak potentials and peak current. Scans were always started at a positive potential and proceeded in the negative direction. Step potential experiments were performed with 10 mM $CoCl_2$ in 20 mM tris-HCl buffer with 100 mM NaCl at pH 7, with the first step at 0.8 V to ensure no cobalt was deposited prior to stepping to the deposition potential of -0.8 V for 40 sec. After deposition, surfaces were stepped to a variety of cobalt stripping potentials, as indicated.

## Results and Discussion

### Reversible redox cycling of iron redox species by pilin monolayers (pSAMs)

We investigated the kinetics of electron transfer through the pSAMs in cyclic voltammograms using 1 mM potassium ferricyanide ($K_3Fe(CN)_6$) in 50 mM tris-HCl at pH 7 with 100 mM NaCl in reference to bare gold and insulating uSAM control working electrodes (Fig. 3.1). As the potential *E* sweeps from positive to negative at a defined scan rate (100 mV/s), the redox species in the analyte is reduced at the surface of bare gold or electrodes functionalized with the pSAM but not with an insulating uSAM (Fig 3.1A). The reduction reaction on bare gold and pSAMs produced a distinctive cathodic peak in the forward scan and an anodic peak was recorded when the scan direction was reversed from negative to positive potentials (Fig 3.1A) as expected for a reversible redox reaction. By contrast, no current was measured on gold electrodes treated with 1-undecanethiol, which self-assembles as an insulating monolayer (uSAM) on the electrode surface (Fig. 3.1A). Treating the pSAMs with 1-undecanethiol (pSAM-uSAM), however, did not have a significant effect on the voltammograms (Fig. 3.1A). This in agreement with atomic force microscopy studies (31), which showed that the thiolated pilins self-assemble on gold electrodes as a dense, confluent monolayer.

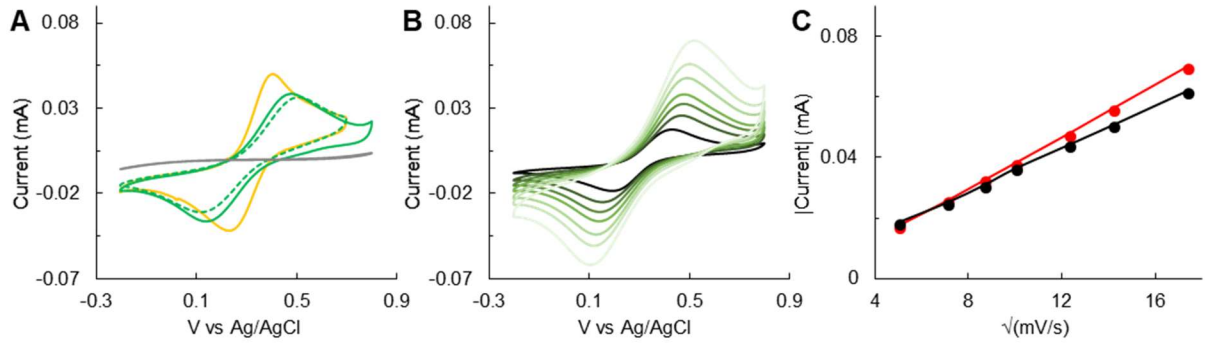


**Figure 3.1:** (A) Cyclic voltammograms collected at 100 mV/s in 50 mM Tris HCl buffer (pH 7, 100 mM NaCl) with 1 mM $Fe(CN)_6$ for bare gold (yellow), pilin monolayers (pSAMs, solid green), pSAMs treated with 1-undecanethiol (pSAM-uSAM, dashed green), and undecanethiol monolayers (uSAMs, grey). (B) Effect of scan rate (25-300 mV/s, darkest to lightest green) on cyclic voltammograms collected for pSAMs under the conditions described in (A). The absolute value of the peak current as a function of the square root of scan rate is shown in (C), with anodic values in black and cathodic values in red.

The midpoint potential of the reaction with each working electrode was calculated by taking the mean of the potential of the anodic peak current ($E_{pa}$) and of the potential of the cathodic peak current ($E_{pc}$) recorded at a scan rate of 100 mV. The midpoint potential calculated for $Fe(CN)_6$ on bare gold was 0.32 V vs Ag/AgCl electrode. A similar value (0.31 V) was calculated for gold electrodes functionalized with pSAM or with pSAM capped with uSAM (hybrid pSAM-uSAM control). The mid-potential value for the bare gold electrode is higher than values, estimated from voltammograms reported for other gold electrodes, of 0.26 V (72), and 0.28 V (73). These differences likely reflect the different buffer conditions and redox species concentration used in our study.

Although the mid-potential of the pSAM was similar to bare gold, peak-peak separation was notably larger when the pSAM is added. This effect indicates a slower electron transfer process at the pSAM compared to the bare gold (33, 74) and unmasks the transport of charges across the 4 nm thick peptide film. Increasing the scan rates from 25 to 300 mV/s resulted in higher currents recorded at the anodic and cathodic peaks for both the bare and pSAM-funcitonalized gold electrodes (Fig. 3.1B). Furthermore, current increased linearly as a function of the square root of scan rate (Fig 3.1C). This linearity agrees well with the Randles−Sevcik equation for a reversible electron transfer process with freely diffusing redox species (33).

The redox activity of the pSAM-functionalized gold electrodes was also tested using $FeCl_3$ in the analyte (Fig. 3.2). As with ferricyanide, the voltammograms had symmetric cathodic and anodic peaks consistent with a diffusible and reversible redox reaction. The midpoint potential for $FeCl_3$ was 0.62 V with bare gold electrode and similar (0.61 V) for pSAMs. However, unlike ferricyanide voltammograms, peak-peak splitting did not increase in the presence of the pSAM. Thus electron transfer with the pSAM proceeded at rates similar to those at the gold electrode surface. This could indicate a more efficient binding at the pilin metal traps with monoatomic metal acceptors (e.g., Fe3+) compared to the chelated ferricyanide species, as predicted from the computational models of the pilus fiber (12). Yet the kinetics of binding of the pSAM traps to the monoatomic iron species are unlikely to be rate-limiting, based on the linearity of the measured anodic and cathodic current as a function of the square root of scan rate (Fig. 3.2B-C), which is indicative of a freely diffusing redox species (33).

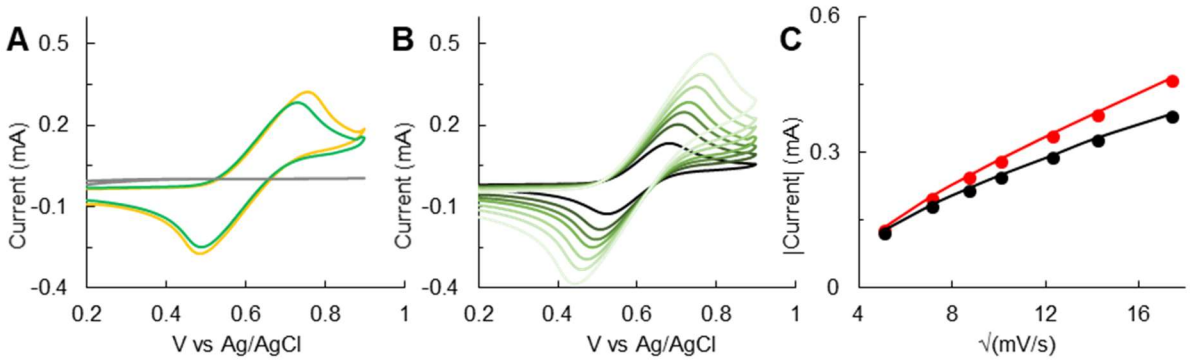


**Figure 3.2: (A)** Cyclic voltammograms collected at 100 mV/s in 50 mM Tris HCl buffer (pH 7, 100 mM NaCl) with 10 mM $FeCl_3$ for bare gold (yellow), pilin monolayers (pSAMs, solid green and insulating monolayers of undecanethiol (uSAMs, grey). (B) Effect of scan rate (25-300 mV/s darkest to lightest green) on cyclic voltammograms collected for pSAMs under the conditions described in (A). The absolute value of the peak current as a function of the square root of scan rate is shown in (C), with anodic values in black and cathodic values in red.

These electrochemical experiments demonstrate the conductivity of pSAMs and suitability of CV under these buffer conditions to examine redox reactions mediated by the pilins in the monolayer. Indeed, the larger peak-peak splitting of pSAM voltammograms with ferricyanide compared to bare gold is likely due to both the size and the negative charge of the $Fe(CN)_6^{-3}$ molecule. Although the pilin metal trap is located on the flexible carboxy-terminal random coil of the pili, the larger size of the electron acceptor is expected to slow down the binding kinetics. Furthermore, the concentration of anionic ligands on the pilins' metal traps is expected to electrostatically repel the ferricyanide species. In contrast, $FeCl_3$ easily dissociates into $Fe^{3+}$ in aqueous systems. The monoatomic species is small in size and positively charged, facilitating

interactions with anionic amino acid ligands of the pSAM and electron exchanges at rates similar to gold electrodes. Not surprisingly, pSAM voltammograms with $FeCl_3$ as the analyte showed no increases in peak splitting compared to bare gold electrodes.

**CV demonstrates the electrodeposition of $Co^{2+}$ on pSAMs.**

Although *Geobacter* bacteria and other metal-reducing bacteria can reduce chelated forms of $Co^{3+}$ to $Co^{2+}$, the divalent cobalt cation is considered too toxic to be reduced biologically (32). Yet $Co^{2+}$ can acquire hexahedral configurations in solution (e.g., $[Co(H_2O)_6]^{2+}$) similar to those of the uranyl cation, which are predicted to be bound with high affinity by the pilin's metal traps (12). Thus, we used CV to investigate the kinetics of the reduction of the divalent $CoCl_2$ species by pSAMs at a neutral pH. Control voltammograms of bare gold with $CoCl_2$ at various voltage ranges consistently show a maximum cathodic peak at about -0.7 V. Lower potentials can cause molecular deformations and affect the integrity of peptide films (42). Potentials below -1 V can also result in the reductive desorption of the thiol-linked peptides (75). Thus, we recorded voltammograms for bare gold and pSAM electrodes at a maximum negative potential voltage sweep of -0.8 V (Fig. 3.3). Voltammograms recorded at a scan rate of 100 mV/s within this voltage range show similar responses of bare gold and pSAMs to the applied potentials yet a complex redox behavior inconsistent with a reversible redox reaction (Fig 3.3A). Indeed, the cathodic peak had a cross-over feature that is characteristic of the formation of a solid phase material on the surface of the electrode, in this case, the electrodeposition of $Co^{2+}$ as the elemental $Co^0$ species (Fig. 3.3) (76).

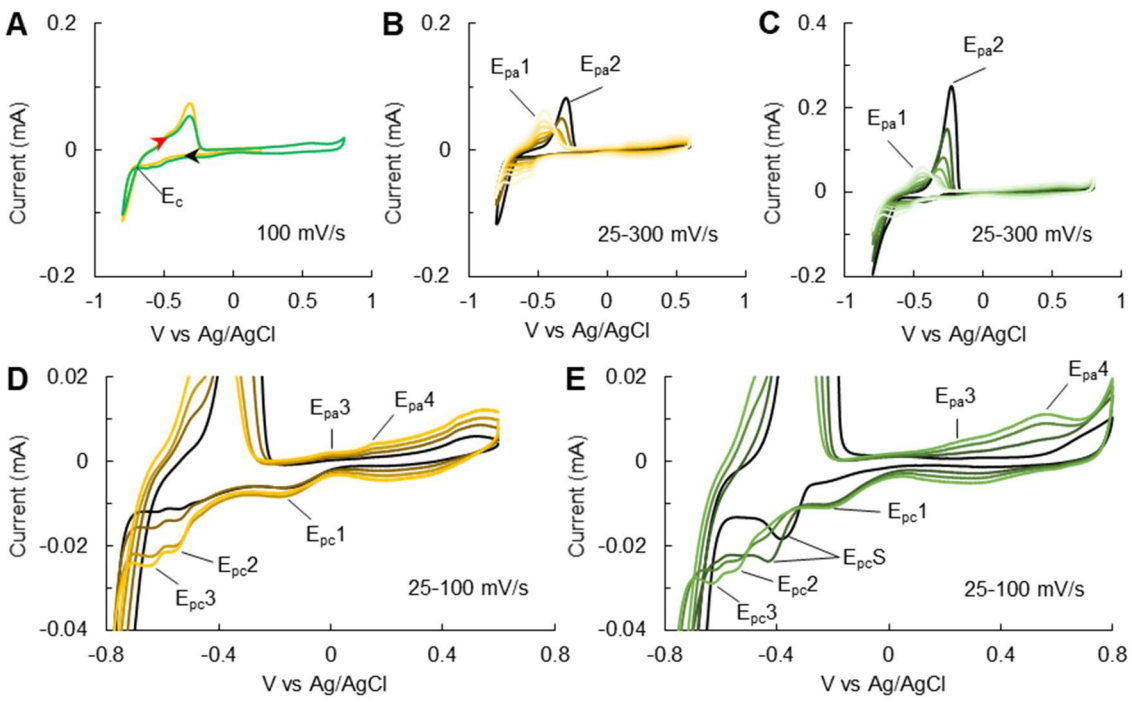


**Figure 3.3:** (A) Cyclic voltammograms collected with a maximum negative potential of -0.8 V on bare gold (yellow) and pSAMs (green) in 50 mM Tris HCl buffer (100 mM NaCl, pH 7) with 10 mM $CoCl_2$ at 100 mV/s. (B-C) Effect of scan rate (25-300 mV/s, darkest to lightest shade) on cyclic voltammograms collected for bare gold (B) and pSAMs (C) with anodic peaks labelled. (D-E) Expanded view of cathodic peaks for both substrates for scan speeds 25-100 mV/s.

The electrodeposition of cobalt occurs on both bare gold and pSAM surfaces is evidenced by a sharp increase in current production (cathodic peak) during the forward scan from positive to negative values (Fig 3.3A). This sharp current increase marks the reduction of $Co^{2+}$ to the sparingly soluble $Co^0$, the reductive precipitation of more $Co^{2+}$ on the $Co^0$ atom (nucleation or crystal growth) and the increase density of nuclei forming on the surface (77-79). As a result, a cobalt layer is formed on the electrode

surface during the forward scan that sharply increases the current of the cathodic peak but also influences the current generated during the reverse scan. As the scan direction reverses, cobalt deposition is still occurring, because the $Co^0$ crystal catalyzes cobalt-on-cobalt deposition. This is a homodeposition process that generates more current than the process of depositing cobalt onto a gold or pSAM surface (heterodeposition) (78). This results in a crossover event, where the higher current generated by the forward scan compared to the reverse scan causes the scan lines in the voltammograms to cross at the overcrossing potential, $E_c$ (Fig. 3.3A) (78). The voltammograms revealed only one cross-over event for both gold and pSAMs at 100 mV/s, but the crossover potential $E_c$ became progressively more negative at faster scan rates (Fig. 3.3 B-C). For bare gold electrode the crossover disappeared at scan rates greater than 150 mV/s (Fig. 3.3B and Table 3.1). For pSAMs, the crossover feature was present in voltammograms recorded at scan rates between 50 and 200 mV/s (Fig. 3 C and Table 3.1).

**Table 3.1**. Peak and crossover potentials (V) measured from cyclic voltammograms on bare gold and pSAMs at a maximum negative potential sweep of -0.8 V. Absence of a value indicates that no peak was present.

**Bare gold**

| mV/s | Epc1 | Epc2 | Epc3 | Epa1 | Epa2 | Epa3 | Epa4 | Ec |
|---|---|---|---|---|---|---|---|---|
| 25 | -0.12699 | -0.53567 | -0.6196 | | -0.29574 | | | -0.64133 |
| 50 | -0.14794 | -0.53926 | -0.62953 | -0.49494 | -0.32698 | -0.01067 | 0.1563 | -0.67828 |
| 75 | -0.16033 | -0.54646 | -0.63746 | -0.49049 | -0.361 | -0.00961 | 0.15353 | -0.71442 |
| 100 | -0.17127 | -0.54614 | -0.65113 | -0.47893 | -0.38002 | -0.00734 | 0.15485 | -0.73107 |
| 150 | -0.17383 | -0.55115 | -0.6611 | -0.456 | | -0.013619 | 0.14931 | -0.77078 |
| 200 | -0.19122 | -0.55804 | -0.67104 | -0.45793 | | -0.00815 | 0.1559 | |
| 300 | -0.19448 | -0.56528 | -0.68019 | -0.45202 | | -0.00544 | 0.15567 | |

**pSAM**

| mV/s | Epc1 | Epc2 | Epc3 | EpcS | Epa1 | Epa2 | Epa3 | Epa4 | Ec |
|---|---|---|---|---|---|---|---|---|---|
| 25 | | | | -0.37789 | | -0.23206 | | | |
| 50 | -0.19585 | -0.52228 | -0.6051 | -0.42933 | | -0.26291 | | 0.53675 | -0.66726 |
| 75 | -0.19448 | -0.53015 | -0.62216 | -0.43223 | -0.48133 | -0.29024 | | 0.54378 | -0.67912 |
| 100 | -0.19104 | -0.53581 | -0.62892 | | -0.4708 | -0.29124 | 0.24502 | 0.551 | -0.69569 |
| 150 | -0.20931 | -0.54713 | -0.63929 | | -0.4579 | -0.35386 | 0.23949 | 0.55497 | -0.72603 |
| 200 | -0.21139 | -0.55133 | -0.64824 | | -0.43907 | -0.34918 | 0.26768 | 0.55572 | -0.75821 |
| 300 | -0.23582 | -0.55854 | -0.65854 | | -0.44002 | | 0.26947 | 0.5584 | |

The voltammograms recorded with the $CoCl_2$ analyte also revealed multiple, small cathodic peaks in both bare gold and pSAMs that preceded the maximum cathodic peak (Fig. 3.3D-E). These secondary peaks mark underpotential deposition (upd) processes, that is, they are potentials that favor stronger interactions between the $Co^{2+}$ metal ion and the electrode surface. This energetic preference causes the metal to deposit from solution into an electrode at a more positive potential (underpotential) (80). Voltammograms with bare gold and pSAMs consistently recorded three small upd

events ($E_{pc}$1-3) (Fig. 3.3D-E). For gold surfaces, these peaks likely correspond to several instances of upd that are related to the surface roughness of the electrode. A rougher surface provides more step edges, which can serve as nucleation sites for the underdeposition of metals (81). These multiple nucleation sites do not have the same energy, and thus we see multiple instances of upd, with the energetically easiest nucleation sites becoming occupied early in the forward sweep ($E_{pc}$1), followed by the less energetically favorable nucleation sites ($E_{pc}$2 and 3) before the surface-wide deposition at sufficiently negative voltages ($E_c$). The current measured at the first upd potential, $E_{pc}$1, responded linearly to the square root of the scan rate in pSAMs, indicating a diffusion limited process, but best fitted a polynomial curved for $E_{pc}$2 and $E_{pc}$3 (Fig. 3.4A, C), indicating these later peaks may be transferring electrons via surface-adsorbed species (33). It is possible then to construct a model in which the cobalt deposited in the first upd event serves as seed sites for the later deposition events, with the current behavior reflecting the electrons passage through the previously adsorbed cobalt on the surface.

Interestingly, the potentials at which different upd events are recorded on pSAMs are more negative than on gold, indicating a higher energetic barrier to deposition on pSAMs compared to bare gold (33). Indeed, whereas voltammograms on bare gold recorded the three upd peak potentials at all scan speeds, electrodes functionalized with pSAMs only showed them at scan rates of > 50 mV/s (Table 3.1, Fig 3.3). This result is in agreement with the reductions in surface roughness measured on pSAMs compared to bare gold electrodes (31). In addition to decreasing the surface roughness of the electrode, pSAMs provide specialized surface motif for metal binding and

reduction that increase the chemical complexity of the deposition process. This effect is revealed at slow (25 mV/s) scan rates (Fig. 3.3E) as a single peak, labeled $E_{pc}S$, that is unique to the pSAMs. The slower scan speed unmasks the specific binding to and reduction of $Co^{2+}$ to $Co^{0}$ at the metal traps at $E_{pc}S$. It also increases the magnitude of the cathodic peak compared to the bare gold (Fig. 3.3 B-C), suggesting a more efficient electrodeposition at the specialized reductive sites of the pSAM. At higher scan speeds, non-specific electron transfer reactions on the film dominate instead and the pilin-specific peak $E_{pc}S$ is lost (Fig. 3.3C). The current at the pSAM cathodic peaks (Fig. 3.3 C) is also lower and more in range with that recorded on bare gold (Fig. 3.3 B). At the higher scan rates, the current behaves similarly to gold, $I_{pc}1$ increasingly linearly as the square root of scan speed, and $I_{pc}2$ and 3 fitting best to a polynomial (Fig. 3.4C). This fits our model of the first upd event seeding and modulating electron transfer for the second and third upd processes.

The current measured at the pSAM anodic peaks (Fig. 3.3C) was also higher than on bare gold, particularly at the lower scan rates (Fig. 3.3C). This is because lower scan rates promote more deposition of cobalt on the pSAMs than in bare gold during the forward scan. Thus, more reduced species are available for solubilization during the reverse scan on pSAMs at these lower scan rates, and more current is recorded at the anodic peaks (Fig 3.3C). The pSAM voltammograms also revealed complex anodic peak behaviors that were sensitive to the scan rate (Fig. 3.3). As with bare gold, pSAM voltammograms had two dominant anodic peaks at negative potentials ($E_{pa}1$ and 2) and two smaller peaks at more positive potentials ($E_{pa}3$ and 4) but the magnitude of the peak current and potential varied with the scan rate (Table 3.1). The dominant anodic

peaks transition from $E_{pa}1$ at high scan rates to $E_{pa}2$ at lower scan rates in both bare gold and pSAMs (Fig. 3.3B-C), slightly shifting towards higher ($E_{pa}1$) or lower ($E_{pa}2$) potentials as the scan rate was sequentially increased from 25 to 300 mV/s (Table 3.1). The anodic peak $E_{pa}1$ was only detected as the scan speed increased (> 75 mV/s in pSAMs and > 50 mV/s for gold), whereas $E_{pa}2$ was only revealed at lower scan rates (Fig. 3.3B-C). The magnitude of the peaks also fluctuated, with decreases in $E_{pa}1$ matching well with increases in $E_{pa}2$. These two peaks appeared to mask each other at the lowest and highest scan rates, as expected from the distinct mechanism of cobalt deposition that dominates at low versus high scan speeds (Fig. 3.3D-E). At low scan rates, cobalt deposition on bare gold is non-specific but it is mediated by the unique chemistry of the pilins in pSAMs, possibly by specific binding in the metal traps. The kinetics of metal binding to the pSAM thus affect the stripping of the cobalt deposits during the reverse scan, which is revealed by the appearance of the $E_{pa}2$ peak. At fast scan rates, however, nonspecific electron transfer reactions dominate in both bare gold and pSAM and the voltammograms become more similar and dominated by the $E_{pa}1$ anodic peak.

Two other small anodic peaks, $E_{pa}3$ and $E_{pa}4$, are also present at more positive potentials (Fig. 3.3D-E) and likely represent stripping events of cobalt minerals that are strongly associated with the surface. The potentials for these peaks are even more positive for pSAM-functionalized electrodes (Fig. 3.3E), indicating that the oxidation of surface-bound cobalt atoms requires more energy to occur in pSAMs than on bare gold. This is could reflect the rectifying behavior of the pSAMs observed at low potentials (31). The reoxidation of $Co^0$ on the pSAMs requires electrons to travel from the metal

trap at the C-t to the N-t cysteine and then to the underlying electrode, a polarity opposite to the biological direction of electron transfer that is less favored in pilin films (31). The current produced at the anodic peaks is largely linear as a function of the square root of scan speed (Fig 3.4B, D) for both pSAMs and gold, except for $I_{pa}2$, which fits best to a polynomial, and is reflective of the change in oxidation behavior as a function of scan speed.

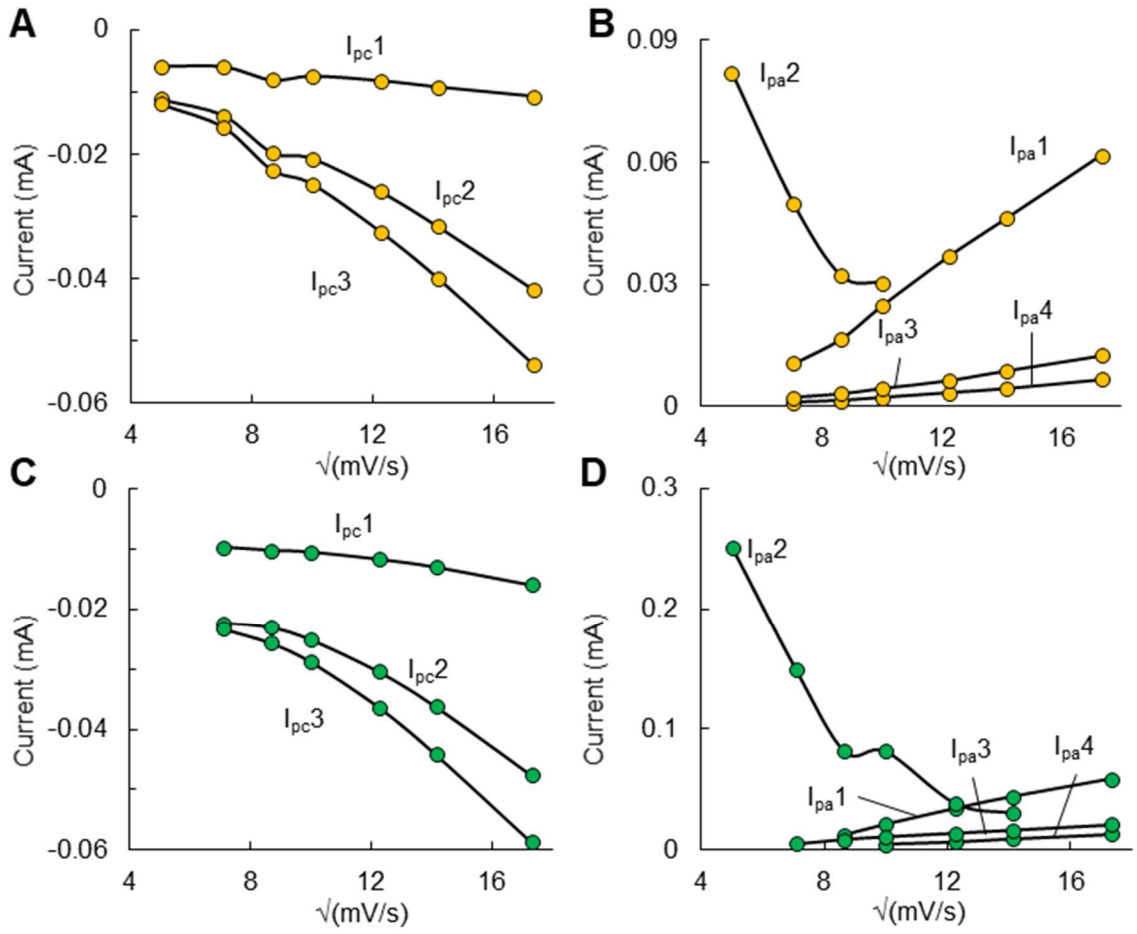


**Figure 3.4:** (A-H) Current (mA) production at cathodic ($I_{pc}$) and anodic ($I_{pa}$) peak potentials versus the square root of scan speed (√(mV/s)) for samples scanned on bare gold (A-B) and pSAM functionalized (C-D) electrodes.

**Potentiostatic experiments provide mechanistic insights into pilin-metal interactions.**

To investigate the mechanism of cobalt deposition by pSAMs compared to gold electrodes, we conducted a three-step potentiostatic experiment (Fig. 3.5) that measured transient current events related to cobalt deposition and stripping from the surface. In each experiment, a deposition potential of -0.8 V was first applied to the working electrode for 40 seconds to immobilize the cobalt (Fig. 3.5A).

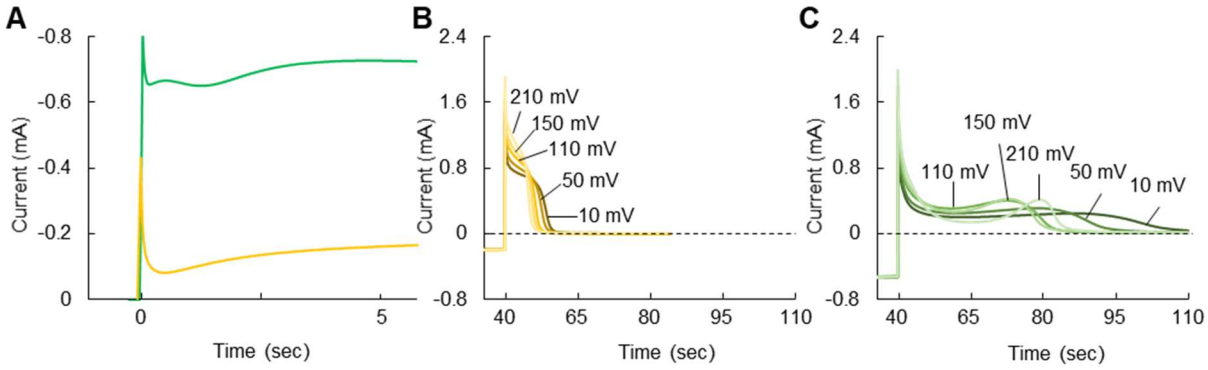


**Figure 3.5:** (A-C) Step potential experiments conducted in 50 mM Tris HCl buffer (pH 7, 100 mM NaCl) with 10 mM $CoCl_2$ on bare gold (yellow) and pSAM functionalized electrodes (green). (A) A deposition potential of -0.8 V is applied for 40 seconds, and the response of both surfaces is shown. (B-C) After 40 seconds of deposition, samples were switched to positive stripping potentials of 210, 150, 110, 50, and 10 mV, from lightest to darkest color. Return of current production to zero indicates completed stripping process.

The layer of cobalt was then stripped at positive potentials of 10, 50, 110, 150, and 210 mV for up to 70 seconds until the current returned to baseline (Fig 3.5B-C). These values were chosen because they are more positive than the most positive

dominant anodic peak, $E_{pa}2$, recorded in cyclic voltammograms (Fig. 3.3). The deposition of cobalt onto a bare gold electrode control showed a simple profile that tapers to a steady current production (Fig. 3.4A). The rapid formation of this peak could have been influenced by the surface roughness of the gold electrode, as nucleation rates increase with the number of surface defects (81). The shape of this deposition event is indicative of a 3-D deposition process with multiple nucleation sites controlled by diffusion of the metal species to the surface in the buffer conditions described (81-83). By contrast, cobalt deposition on the pSAMs requires more energy, but proceeds more efficiently compared to bare gold (Fig. 3.4A). This deposition behavior is closer to that of a surface with restricted nucleation sites (81) and is often encountered when cobalt interacts with discrete metal binding sites involved in charge transfer, an important component of the deposition process (84). The pSAM film effectively masks step edges and defects (31) that otherwise serve as non-specific nucleation sites for metal deposition on bare gold. This leads to a different current response to deposition than that of the gold electrode (Fig 3.4A). The smoother pSAM surface also increases the magnitude of the current response. This increased current production could indicate that even with less nucleation sites, the electron transfer to cobalt ions at what sites are present is much stronger, which occurs in the biologically relevant direction, is much stronger. This model is also supported by the dynamics of stripping cobalt from the surface (Fig 3.4B-C). Indeed, significantly more time is needed to fully remove the cobalt from pSAMs than for gold electrodes. The lowest potential that strips the cobalt from the bare gold surface does so in ~15 seconds, whereas the shortest time for cobalt stripping with pSAMs is ~65 seconds. Removing the cobalt film from a pSAM is also a

more complex process, as indicated by the number of secondary peaks arising depending on the stripping voltage. This behavior is likely related to the complex and flexible chemical nature of the pSAMs surface, which may influence the kinetics of metal desorption.

## Conclusions

Electrochemical techniques were applied to probe the metal binding capability of pilin films (pSAMs) on gold electrodes. Cyclic voltammetry revealed efficient redox cycling of two ferric iron species, ferricyanide and ferric chloride. Voltammograms revealed a conductive monolayer capable of interacting with both the bulky ferricyanide group and the non-negatively charged hydrated ferric ion at pH 7. The midpoint potentials of ferricyanide vs Ag/AgCl on bare gold were 0.32 V and 0.31 V for pSAMs and pSAMs capped with an undecanethiol layer. Current increased linearly as a function of the square root of the scan speed, indicating a Nernstian reversible redox process governed by diffusion (33). Similar results were obtained with the $FeCl_3$ salt, except for the midpoint potential, which was more positive with both electrodes (0.62 V vs Ag/AgCl for bare gold electrodes and 0.61 V for pSAMs). However, differences in size (monoatomic $Fe^{3+}$ rather than the large chelated form of in ferricyanide) and charge (positively charged $Fe^{3+}$ ion rather than the negative charge of the ferricyanide species) affected the kinetics of binding to the pSAMs by the two iron species, causing a separation of anodic and cathodic peaks with ferricyanide that is in agreement with a salt that is too large to bind the pilin metal traps and can electrostatically be repelled by the numerous anionic ligands in these surface motifs (12, 31).

Cobalt voltammograms however revealed an electrodeposition process, whereby the $Co^{2+}$ species is reduced to the sparingly soluble elemental $Co^0$ and the reduced species acts as nucleation site for more deposition. The cathodic peak behavior consistently revealed two or more underpotential peaks, with one consistently appearing at roughly -0.2 V and a second at roughly -0.5 V for bare gold electrodes. Slow scan

rates to pSAMs revealed an underpotential ($E_{pc}S$) peak near -0.4 V that is unique to the pilin film and may unmask the specific binding and reduction of cobalt by the pilins' metal traps at this applied potential. A mutagenic study, where the binding pocket is disrupted in various ways (e.g., to restrict access of the metal the redox-active tyrosine or to prevent electrostatic interactions with the metal pilin ligands), would give direct evidence for the validity of this model.

A step potential experiment further confirmed the ability of the pSAM to interact with and modulate the reductive deposition of cobalt on its surface, as compared to a bare gold electrode. The C-t random coil of the pilins, which is exposed to the solvent in the pSAMs, and the concentration of negatively charged amino acids in this region is predicted to promote the binding of soluble cations (31). This would facilitate the binding of the divalent $Co^{2+}$, as is reflected in the current production and kinetics of deposition and stripping of cobalt. Cobalt was deposited at a potential of -0.7 V and the transient current response matched well with a 3D-nucleation process limited by a reduced number of nucleation sites in the pSAMs compared to the bare gold electrode surface, which have greater roughness and, therefore, more defects for non-specific deposition. Yet despite having reduced nucleation sites, the pSAMs produced more current during deposition, a behavior that could reflect a more efficient process of binding but also reduction. Indeed, the polarity of electron transfer during deposition, from the amino-terminus to the carboxy-terminus of the peptide, is favored in pSAMs (31).

The step potential experiments also revealed binding and electron transfer kinetics on the pSAM that could have been influenced by the reversal of the polarity of electron transfer and binding effects. After 40 seconds of cobalt deposition the potential

was shifted to potentials more positive than the most positive cobalt stripping peak ($E_{pa}2$) in order to reoxidized and solubilize (strip) the cobalt layer. The stripping process from the bare gold electrode completes in at most 15 seconds with a simple current decay profile depending on the potential. However, stripping cobalt from the pSAM takes longer and involves a more complex process, as indicated by the current peaks that appear at different times during stripping. The longer time-frame and complexity of the stripping process, combined with the transient current data, provide compelling evidence for a model of pSAM mediated deposition and stripping reliant on restricted nucleation sites on the film surface, where the C-t metal-binding traps of the pilins are concentrated.

The results highlight the unique material properties of planar assemblies of conductive recombinant pilins that make them excellent *in vitro* tools to examine the catalytic properties of the pilus metal traps even when working with toxic metals. Results from the electrochemical studies with pilin films can also inform *in vivo* studies about the spectrum of metals that the pili can bind and reduce *in vivo*. Indeed, $Co^{2+}$ has been assumbed to be too toxic for its reduction, yet the pSAM studies show a mechanism for $Co^{2+}$ binding and reduction that could allow cells to mineralize the toxic cation extracellularly to prevent its permeation and non-specific reduction in the periplasmic space. Planar pilin assemblies could also provide the foundation of novel platforms for environmental sensing, the remediation of toxic cationic metals, and the reclamation of precious and rare metal cations.

# Chapter 4.

# Assembly and Characterization of Protein Nanowires with Recombinant *Geobacter* pilins

**Authors contributions:**

Angelines Castro-Forero performed the circular dichroism experiments with recombinant $PilA_{19}$ pilins and preliminary self-assembly studies. Krista M. Cosert optimized the recombinant pilin production system and the bottom-up fabrication of pilin-based fibers and carried out experiments to investigate the molecular and electronic properties of the recombinant pili.

## Abstract

Metal-reducing bacteria in the genus *Geobacter* produce dynamic and conductive appendages to bind and reduce extracellular electron acceptors such as Fe(III) oxides and uranium during respiration. The *Geobacter* pili are homopolymers of an unusually short pilin peptide containing aromatic amino acids that cluster in the pilus fiber to promote fast discharges of respiratory electrons. Here we describe the recombinant production and *in vitro* assembly of pilin building blocks into pilus fibers that retain the electronic properties reported for the native pili even under chemical fixation. Furthermore, we describe nucleation and elongation steps that control the efficiency of self-assembly and permit the tunability of the fiber length. The implications of these results for the design and mass-production of generations of protein nanowires for custom applications are discussed.

## Introduction

Bacteria in the genus *Geobacter* produce conductive protein appendages of the Type IVa pilus class to bind and reduce iron (Fe[III]) oxide minerals (4) and the uranyl cation (6). As in other bacteria, the *Geobacter* pili are an assembly of a single peptide subunit (the pilin or PilA) (6) that is synthesized as a precursor (prepilin) carrying the conserved Type IVa pilin recognition sequences needed for removal of the leader peptide and *N*-methylation of the mature peptide (4). A canonical Type IV pilus apparatus spanning the multilayered cell envelope assembles the pilins through the inner membrane and exposes the base of the pilus fiber to periplasmic cytochromes to facilitate the discharge of respiratory electrons (8). Each pilus fiber can transport ~ 1 billion electrons per second at biologically relevant voltages (100 mV), a rate that is two orders of magnitude greater than the cellular rates of respiration (13). Yet each cell produces several pili monolaterally (4), a biological strategy that maximizes access to the most bioavailable forms of iron oxides, which are dispersed in soils and sediments and rapidly transition into more crystalline and less bioavailable mineral forms abiotically (8). The reduction of iron oxides solubilizes part of the Fe(III) but also generates magnetite, a magnetic mineral of mixed Fe(III)/Fe(II) state that remains bound to the pilus fibers. Similarly, the pili retain the mononuclear uranium mineral phase formed during the reduction of the soluble uranyl cation (6). To enable new rounds of respiration, cells detach the reduced minerals by depolymerizing the pilins in a reaction energized by an ATPase (PilT4) of the pilus apparatus (5). The retraction of the pili stores the pilin peptides in the inner membrane, making them readily available for a new

round of polymerization energized by the PilB ATPase (5, 9). Antagonistic cycles of pilus protrusion and retraction are therefore critical for sustained respiration.

Studies in the model representative *Geobacter sulfurreducens* (GS) have helped identify structural features of the *Geobacter* pilins that are critical for fiber formation and conductivity (8). The most notable divergent feature of the *Geobacter* pilins is their reduced size (61 amino acids in the GS pilin compared to 142-175 in other bacterial pilins) (8). Because of their short size, the *Geobacter* pilins lack the conserved modular architecture of other Type IVa pilins and only retain the amino-terminal (N-t) $\alpha$-helix ($\alpha$1 domain) that is required for biological assembly (10, 11). This divergent structure, which is conserved in *Geobacter* and other members of the order Desulfuromonadales (3, 4), is predicted to favor charge transport through the pilin peptide (11). Indeed, the carboxy-terminal (C-t) globular head of Type IVa pilins, with its distinctive αβ-loop, anti-parallel β-sheet domain and D-region flanked by two conserved cysteines (85), is replaced in *Geobacter* pilins by a short, flexible random-coiled segment (10). This architecture effectively removes the insulating β-sheets and makes the peptide primarily α-helical, a conformation that promotes electronic coupling and charge transport (19, 20).
The predominantly α-helical conformation of GS-like pilins increases the hydrophobicity and flexibility of the peptides. This, in turn, promotes strong hydrophobic pilin-pilin interactions during self-assembly and the formation of a strong yet flexible pilus fiber core (12). Molecular dynamics (MD) simulations show the pilins' short C-t random coil protruding from the fibril's core at a 40° angle and exposing amino acid ligands (negatively-charged glutamic acid and a tyrosine) that could bind and reduce the electron acceptors (12). The atomic coordination predicted for these ligands (12)

matches well the atomic environment of two bidentate (anionic carboxylate side chains) and one monodendate (tyrosine side chain) ligands modeled from the uranium $L_{III}$-edge extended X-ray absorption fine structure (EXAFS) spectra of the pilus-bound uranium atom reduced *in vivo* (6). This suggests that the pilus surface is decorated with metal traps with the electrostatics needed to bind cationic metals and to position them optimally for their reduction (8).

The MD model of the pilus fiber also predicts the alignment of positively and negatively charged amino acids from neighboring $\alpha$1-domains during pilin assembly (12). This alignment enables the formation of salt bridges (D53-K30 and D54-R28), bends the peptides' mid-region, and brings the side chains of neighboring aromatic residues (phenylalanines and tyrosines) at distances optimal for charge transport (12). In the MD simulations (12), some of the aromatic rings are dynamically brought together at distances between 3 and 5 Å but the aromatic contacts never form at the same time, as in a metallic wire (12). Furthermore, the geometry of the aromatic dimers is always too displaced to support π–π stacking (8). Thus, the structural evidence provided by computational models supports a coherent mechanism of conductivity mediated by aromatic contacts. This is further supported experimentally by the thermal activation of pilus conductivity demonstrated by scanning tunneling microscopy and the charge mobility calculated for pilus fibers purified free of metal and organic contaminants, which is too low to support a metallic-like band conduction mechanism (13).

Harnessing the unique properties of *Geobacter* pili will ultimately require protocols for their purification at high yields. Direct purification from the native cells is achievable but requires many purification steps to separate the pili from other cellular

components (6, 13). Moreover, cultivation of piliated cells under anaerobic conditions is not easily scalable and yields of pure pili are low (in the mg range) (6, 13). To bypass these limitations, we recently developed a recombinant expression system in *Escherichia coli* for high-yield production of soluble GS pilin monomers (31). The recombinant pilins carry N-t truncations that preserve the predominantly helical conformation of the peptides (needed for self-assembly), the charged residues needed for salt bridge formation and metal binding, and the aromatic amino acids required for electronic coupling and charge transport in the pilin assembly (31). This construct permitted the self-assembly of a thiolated recombinant pilin as a dense and electrically conductive monolayer on gold electrodes (31). The planar assembly of thiolated pilins was mediated by hydrophobic interactions between the $\alpha$1 domains of neighboring peptides, as in the pilus fiber (12), and permitted the electronic coupling of aromatic side chains and exposure of the C-t flexible random coil to the solvent (31). This makes recombinant pilins attractive building blocks to develop bottom-up protocols for the manufacturing of novel conductive biomaterials.

Here we describe a rapid and scalable strategy to induce the self-assembly of recombinant pilin peptides and the formation of conductive fibers with structural and electronic characteristics that rival their native counterparts. Unlike the synthesis of inorganic semiconductors, the bottom-up fabrication of pilin-based nanowires does not require complex crystal growth or the use of toxic metals. It relies instead on an initial nucleation step with a hydrophobe and an elongation step that controls the length of the nanowire product. This simple process, and the genetic amenability of the recombinant

production system, offers opportunities to tune the material's properties for applications of these novel biomaterials in electronics.

## Materials and Methods

### Bacterial strains and culture conditions.

*Geobacter sulfurreducens* strain PCA was routinely grown in anaerobic NB medium (47) with 20 mM acetate as electron donor and 40 mM fumarate as electron acceptor. Genomic DNA extracted from these cultures was used as template to PCR-amplify the native *pilA* gene (GSU1496) and engineer recombinant pilin production systems in *E. coli* Rosetta™ 2 (DE3) pLysS cells (Novagen), as described below. The *E. coli* cultures were propagated in Luria Bertani (LB) medium supplemented with antibiotics, as described below. The cultures were stored in 20% glycerol at -80°C for long-term preservation.

### Recombinant production and purification of $PilA_{19}$ pilins.

The recombinant production of the $PilA_{19}$ peptide was as described elsewhere (31). Briefly, a *pilA19* genetic construct, which encoded a protein that carried an 19-amino acid truncation in the mature pilin PilA peptide of *G. sulfurreducens* (GSU1496), was cloned into the pTYB11 plasmid vector (IMPACT™-CN system, New England Biolabs) to fuse the N-t region of $PilA_{19}$ to an intein linker and a chitin-binding domain (CBD). The resulting plasmid (pTYB11*::pilA19*) was transformed into *E. coli* Rosetta™ 2 (DE3) pLysS cells (Novagen).

For recombinant expression, strains of *E. coli* carrying pTYB11*::pilA19* were grown in 1 L cultures of LB broth supplemented with 100 μg/ml ampicillin and 20 μg/ml chloramphenicol at 37°C to an $OD_{600}$ ~0.4. The expression of the fusion protein was then induced by adding 50 mM of isopropyl β-D-1-thiogalactopyranoside (IPTG) and

incubating the cultures overnight at 16°C. Cells were harvested by centrifugation (4,000 x *g* for 10 min), lysed via tip sonication in lysis buffer (20 mM Tris-HCl, 100 mM NaCl, 1 mM EDTA, 1% CHAPS) and centrifuged again (12,000 x *g* for 30 min at 4°C) to collect the supernatant fraction. The clarified lysates were loaded onto a chitin column (New England Biolabs; ca. 40 ml bed volume) equilibrated with 200 ml of column buffer (20 mM Tris, 100 mM NaCl, 1 mM EDTA, pH 7.4). After incubation at room temperature for 20 min, the column was washed with 200 ml of buffer at increasing salt concentrations (20 mM Tris, 1 mM EDTA, 0.6/1 M NaCl pH 7.4). Cleavage of $PilA_{19}$ was triggered by incubating the chitin bed with ~ 200 ml of cleavage buffer (20 mM Tris, 100 mM NaCl, 50 mM 1,4-dithiothreitol [DTT], pH 9) for 24 h at room temperature. Elution buffer (cleavage buffer without DTT) was used to elute the cleaved $PilA_{19}$ peptide and the eluent was collected in 2-ml fractions; those containing the peptide were identified by UV absorption at 280 nm and pooled together. Peptide concentration was routinely estimated as absorbance at 280 nm using a NanoDrop™ spectrophotometer (Thermo Scientific).

**Denaturing polyacrylamide gel electrophoresis (SDS-PAGE).**

Proteins in culture supernatant fluids, cell pellets, and in the pooled purified recombinant peptides were separated in 10-20% Tris-Tricine polyacrylamide gels (Bio-rad). The gels were run for 75 min or longer at 100 V in Tris-tricine-SDS buffer (100 mM Tris, 100 mM tricine, 0.1% w/v SDS) using a Mini Trans-Blot cell system. Proteins in the gels were fixed for 30 min with an aqueous solution of 50% methanol and 40% acetic acid prior to Coomassie staining and de-staining with $ddH_2O$.

**Circular Dichroism (CD).**

$PilA_{19}$ peptides purified in elution buffer were dialyzed against 10 mM potassium acetate buffer (with 50 mM $Na_2SO_4$, pH 3.8) using Spectra/Por® Biotech cellulose ester dialysis membranes (MWCO 100-500 Da). The peptide concentration was determined from the difference spectrum of the protein dissolved in 6 M guanidine hydrochloride at pH 12.5 versus pH 7.1 (86). A pH 12.5 guanidine solution (1 ml) was scanned from 320 to 270 nm in the sample compartment using as a reference 1 ml of the pH 7.1 guanidine solution to obtain difference spectrum. The concentration of the peptide in the solutions was estimated from the absorbance at 293 nm using the known amino acid composition of the $PilA_{19}$ subunit and the reported values of the molar extinction coefficients for tyrosine and tryptophan residues (87), using the equation below:

$$c = \frac{A_{293}}{2{,}357Y + 830W}$$

where $Y$ is the number of tyrosines (3 in $PilA_{19}$) and $W$ is the number of tryptophans (0 in $PilA_{19}$).

The concentration of the peptide in the buffer was adjusted to approximately 50 μg/ml. When indicated, sodium dodecyl sulfate (SDS) was added to the peptide solution at a final concentration of 1, 8 or 40 mM. The peptide solutions were dispensed in a quartz cuvette (0.1 cm path length, Starna Cells Inc.) and their CD spectrum in the 190 to 360 nm was collected at 0.5 nm increments (5 second integration time) using a Chirascan™ spectrometer (Applied Photophysics Ltd., Leatherhead, United Kingdom). The spectra were baseline-corrected and smoothed using a third order Savitsky-Golay filter. The CD instrument units (θ, millidegrees) were converted into mean residue molar ellipticity [θ] units using the Wallace and Janes equation (88):

$$[\theta] = \left( \frac{\theta \times 0.1 \times MRW}{c \times l} \right)$$

where *c* is the peptide concentration in mg/ml, *l* is the path length of the cuvette in cm (0.1 cm), and *MRW* is the mean residue weight of the sample, calculated with the equation:

$$MRW = \frac{MW}{n-1}$$

where *MW* is the peptide molecular mass in Daltons (4,524 Da for $PilA_{19}$) and *n* is the number of amino acid residues (42 for $PilA_{19}$).

The percentage of the peptide adopting an $\alpha$-helix conformation was calculated from the CD data using the program CONTINLL at the DICROWEB server (89, 90). The program is a modification of the CONTIN method developed by Provencher and Glöckner (91, 92). It uses a ridge regression algorithm to estimate the CD spectrum of unknown proteins by comparison to a linear combination of CD spectra of *N* reference proteins with known conformations (86, 93). Relatively good predictions of $\alpha$-helix and $\beta$-sheet content can be obtained with this method (86). The secondary structure components determined with CONTINLL are $\alpha$-helix (regular $\alpha_R$ and distorted $\alpha_D$), $\beta$-strands (regular $\beta_R$ and distorted $\beta_D$), turns, and unordered (93). CONTINLL has a higher predictive accuracy than other CD-analysis algorithms for small proteins (86). However, it uses reference data containing mainly globular proteins, which reduces the accuracy of conformation estimates for peptides, fibrous, and membrane proteins (86, 88, 89).

The program evaluates the goodness of fit parameter normalized mean residue standard deviation (NMRSD), which is defined as:

$$NRMSD = \left[ \frac{\sum \left( \theta_{\exp} - \theta_{cal} \right)^2}{\sum \left( \theta_{\exp} \right)^2} \right]^{1/2}$$

where $\theta_{exp}$ and $\theta_{cal}$ are the experimental and calculated ellipticity values at a specific wavelength. A NMRSD value of less than 0.1 is generally considered a good fit (88). In the analysis presented here data with NMRSD values above 0.12 were rejected.

The CD spectra were also collected for recombinant pili assembled *in vitro* and solubilized for 30 min in 10 mM potassium acetate with 50 mM $Na_2SO_4$ (pH 7). A 500 µl aliquot of a 40 µg/ml (estimated via nanodrop) pili solution was dispensed into a quartz cuvette with a 1 mm path length (Starna Cells Inc., Atascadero, CA). Samples were measured using a Chirascan™ spectrometer (Applied Photophysics Ltd., Leatherhead, United Kingdom) from 190 to 260 nm at 0.5 nm increments with a 5 second integration time with automated baseline subtraction. Scans were adjusted from θ, millidegrees, to molar ellipticity using equation (2), as described above. Control scans were also collected for native pili, purified as described elsewhere (6), and denaturing conditions (8 M urea).

***In vitro* assembly of PilA$_{19}$ pilins.**

A solution of the recombinant peptide (8-9 mg of $PilA_{19}$ in elution buffer) was applied by gravity flow to a reverse phase C18 column (3-ml column volume, Waters) that had been previously equilibrated with 5 ml of acetonitrile and 5 ml of $ddH_2O$. After washing the column with 9 ml of $ddH_2O$, the column-bound peptide was eluted in a disposable glass tube with 3 ml of a freshly prepared assembly buffer (80:20, acetonitrile:methanol). After buffer exchange, a 1-ml aliquot of the peptide solution was

transferred to an Eppendorf tube® (1.5 ml) to initiate the evaporation-induced self-assembly phase for 30 min at 45°C in a Savant™ SpeedVac™ concentrator (SPD121P model, Thermo Fisher). Four aliquots (500 µl each) of the peptide solution were added sequentially every 30 minutes. When indicated, the sample was mixed by aspiration during each refeeding step to control fiber growth. After addition of the final aliquot, the solution was dried to completion before resuspending in 200 µl of $ddH_2O$. This final aqueous solution was split into 50 µl aliquots and mixed with 200 µl ice cold acetone to precipitate the fibers overnight at -20°C. The precipitated fibers were recovered as a pellet by centrifugation (1h, 4°C in a microcentrifuge), dried under a stream of $N_2$ gas and stored at -20°C until further use.

**Scanning Probe Microscopy.**

Fibers assembled *in vitro* and stored in dried form at -20°C were suspended in 200 µl of $ddH_2O$ and incubated overnight at 4°C before depositing 10 µl aliquots on the surface of a freshly-cleaved Highly Oriented Pyrolytic Graphite (HOPG; SPI Supplies). After 10 min deposition, excess fluid was wicked off with absorbent lens paper and the HOPG surface was washed two times with 10 µl of $ddH_2O$. Samples were allowed to dry in a sealed container at room temperature for approximately 10 minutes before Atomic Force Microscopy (AFM) analyses with an Asylum Research Cypher S system equipped with AC240TS tips (Asylum Research). Several fields 10 x 10 $\mu m^2$ were scanned in tapping mode to locate areas with fibers and select representative fields for imaging. Pilus length was estimated with the free hand tool of ImageJ. The transversal conductivity of the recombinant pili was measured by conductive probe AFM (CP-AFM),

as described elsewhere (13). Controls with native pili were prepared using published purification protocols (13).

When indicated, the AFM tip was replaced with a mechanically cut Pt:Ir STM tip (Asylum Research) to image the pili in scanning tunnelling microscopy (STM) mode. The quality of the STM tip was tested in scans on the freshly cleaved HOPG surface prior to depositing and scanning the pili samples (sample voltage of 500 mV; current set point of 350 pA). Current-voltage (*IV*) plots for individual fibers were collected at a set point of 10 pA, with the tip held at ground, while sweeping the bias voltage (±0.6 V) of the HOPG substrate. The ohmic portion of the *IV* plots in the ±0.1 V range was fitted to a linear regression line using the Igor Pro 6 software and compared to the differential conductance. The differential conductance was calculated from the *IV* plots in igor using the differentiate function and smoothed with a 27-point Savitsky-Golay filter. The voltage range was restricted to ±0.4 V for clarity, as plots were quite noisy significantly outside of the ohmic region.

## Results

### Recombinant production and structural characterization of pilin building blocks.

We used a previously described *E. coli* recombinant pilin production system (31) for high-yield synthesis of $PilA_{19}$, a derivative of the GS PilA pilin that carries a 19 amino acid truncation at the N-t. The recombinant system expresses the peptide as a fusion protein with a chitin-binding domain (CBD-$PilA_{19}$) and an intein linker, which enables its purification in a chitin affinity column and in-column self-cleavage in the presence of a reducing agent (DTT), respectively (Fig. 4.1A). The molecular weight of the peptide was confirmed by MALDI-TOF mass spectrometry analysis (4,593 Da).

We used circular dichroism (CD) to investigate the secondary structure of the peptide in a hydrophobic environment reminiscent of the cell membrane, where the native pilins are stored and assembled (Fig. 4.1B). The far UV CD spectrum of the peptide in 10 mM potassium acetate buffer at pH 7 showed very low ellipticity above 210 nm and a strong negative signal around 200 nm, consistent with a disordered peptide (94). Addition of the detergent SDS shifted the spectra and revealed the characteristic maxima (at ~190 nm) and minima (at ~208 and ~222 nm) of $\alpha$-helical conformations (95). This result is consistent with the positive effect of SDS in recreating the hydrophobic membrane environment where the pilins are stored, which is needed to induce and stabilize $\alpha$-helices (96).

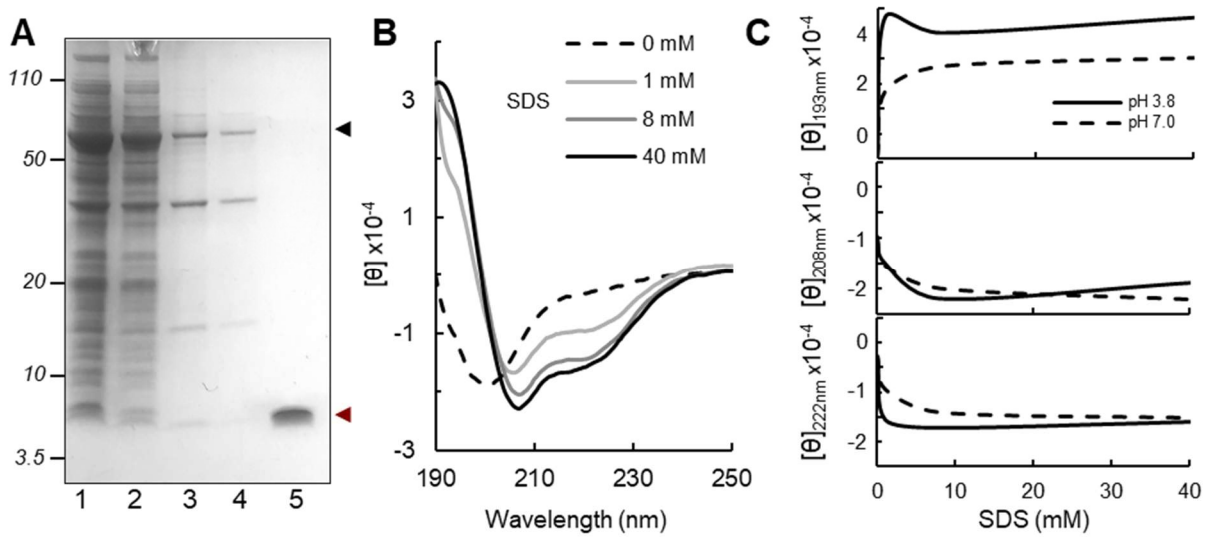


**Figure 4.1:** Recombinant production (A) and structural characterization (B-C) of $PilA_{19}$ peptides. (A) SDS-PAGE gel showing proteins in the soluble (lane 1 and 2) and insoluble (lane 3 and 4) cell extracts from two independent cultures, and pooled eluted pilin (lane 5). Arrows point at the migration of the CBD-$PilA_{19}$ (black) and the recombinant $PilA_{19}$ eluted from the column (maroon). Numbers at left are molecular weight standards in kDa. (B) Effect of SDS at pH 7 on CD spectra of $PilA_{19}$ peptides. (C) Molar ellipticities at key wavelengths for pH 3.8 and pH 7 showing the largest helical structure is induced above the critical micelle concentration of SDS.

As shown in Fig. 4.1C, the intensity of the positive (190 nm) and negative (208 nm and 222 nm) helical signals reached maxima at or above the critical micellar concentration (CMC) of SDS, which is ~ 8 mM in water (97, 98). These detergent concentrations (8 mM and 40 mM) also produced intensity ratios of 220 nm over 208 nm (~ 0.7) close to the 0.8 ratio expected for a single-stranded $\alpha$-helix (99). To minimize electrostatic effects between the peptide and SDS, we also collected CD

spectra at a pH of 3.8. At this pH, below the theoretical isoelectric point (pI, 4.86), the pilin peptide has a net positive charge of + 3.2 and electrostatic effects with the anionic detergent are minimized compared to at pH 7, where $PilA_{19}$ has a negative net charge (-1.1). As predicted, the intensity of the α-helical signature peaks was greater at pH 3.8 than at pH 7 (Fig. 4.1C). The low pH also allowed the peptide to adopt $\alpha$-helical-like conformations (~49% of the amino acids) at detergent concentrations below the CMC (1 mM). By contrast, only 27% of the peptide was $\alpha$-helical at this low SDS concentration when the pH was raised to 7. Concentrations of SDS at or above the CMC increased the helical content at both pH but were higher (56%) at pH 3.8 compared to pH 7 (43-48%), in agreement with the more favorable electrostatic interactions predicted at the lower pH. This demonstrates the critical role of hydrophobicity in modulating the folding of the recombinant pilins in the helical conformation that is required for self-assembly. Furthermore, it identifies pH as an important variable to control the peptide's electrostatics and potentially the charges of amino acids responsible for the formation of salt bridges between neighboring pilins during assembly.

**Fiber formation via self-assembly of pilin derivative.**

CD spectra of the $PilA_{19}$ pilin collected at pH 3.8 and 1 mM SDS show an intensity ratio of the 220 nm and 208 nm peaks of ~ 1, a value that has been proposed to reflect the tertiary structure of $\alpha$-helices assembled in coiled-coil configurations (99). This value suggests that the presence of a hydrophobe, even at low concentrations, can induce the self-assembly of the pilins into supramolecular structures. Based on this, we designed a protocol that recreated the hydrophobicity and molecular packing needed for

controlled self-assembly of the $PilA_{19}$ peptide in solution. The protocol included a buffer exchange step to resuspend the peptide in an assembly buffer of acetonitrile and methanol and a controlled evaporation step to induce the self-assembly of the peptide monomers (Fig. 4.2A). The assembly buffer included acetonitrile, an organic solvent with lower polarity than water that helps maintain recombinant pilin peptides in solution prior to self-assembly (31). The assembly buffer also contained methanol, an organic solvent that stabilizes helical peptide conformations (100). As the assembly buffer evaporates, molecular crowding increases, creating a hydrophobic environment that promotes the self-assembly of the peptides. Self-assembly was stimulated in the presence of a hydrophobe, which acted as nucleator to prime pilin assembly. This assembly could be achieved with octadecane-coated silica particles that co-eluted from the C18 column or with manually added octadecane (Appendix A3). Sequential steps of evaporation and peptide refeeding were optimal for self-assembly of recombinant pilins into fibers (Fig. 4.2B-G). The initial evaporation step of a 1 ml volume of assembly buffer with the peptide (~ 3 mg) stimulated nucleation and sequential feeding steps provided the necessary peptide building blocks to elongate the fibers. This protocol generated fibers approximately 1 ($\pm$ 0.5) $\mu$m long but some samples also contained amorphous assemblies (Fig. 4.2B-D). Mixing by aspiration after peptide re-feeding increased the number of nucleation sites available for peptide elongation, promoted fiber formation and prevented the formation of random assemblies (Fig. 4.2E-G).

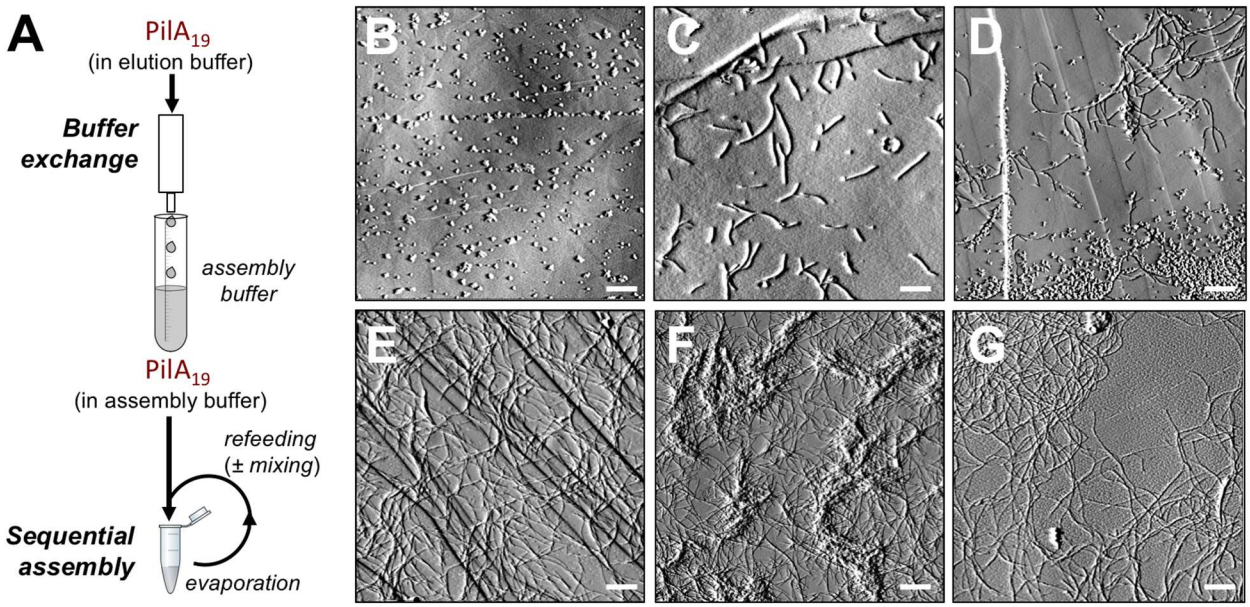


**Figure 4.2**: Evaporation-induced self-assembly of recombinant $PilA_{19}$ peptides. (A) Protocol illustrating the steps in the assembly of $PilA_{19}$ fibers. The evaporation-induced assembly included sequential additions of the peptide solution to elongate the fibers. (B-G) Supramolecular pilin structures formed in triplicate reactions without (B-D) or with (E-G) mixing the assembly buffer after peptide refeeding.

The optimized assembly protocol, with sequential refeeding and mixing steps, consistently produced long (6 ± 1 μm), flexible fibers with an average diameter (calculated as AFM height) of ~2 nm, as reported for the AFM height of the native GS pilus fibers (13). Supramolecular structures (braids and bundles) were also observed (Fig. 4.3A) but not to the extent that is routinely observed when imaging purified preparations of the native pili by AFM (Fig. 4.4). As a result, it was possible to collect less convoluted CD spectra for the recombinant fibers compared to the native ones (Fig. 4.3B and C, respectively). Furthermore, the CD profile of the recombinant pili was similar to that reported for other Type IVa pili (101), consistent with a macromolecule

that preserves the distinctive helical features of bacterial pilin assemblies. Indeed, from the spectral signatures of the recombinant fibers (Fig. 4.3B) we estimated intensity ratios of 220 nm over 208 nm (~0.75), which were close to the 0.8 ratio expected for α-helical conformations (99).

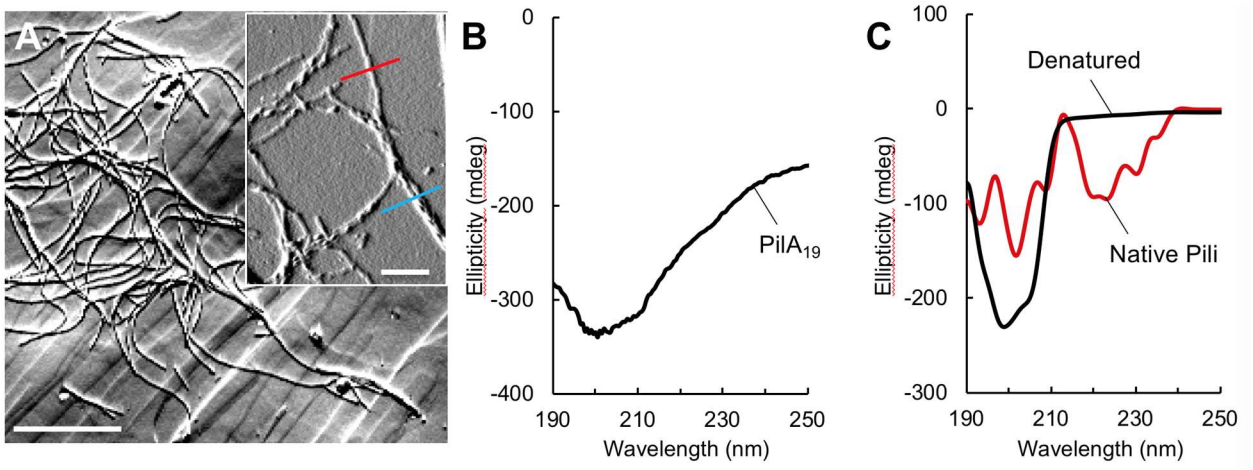


**Figure 4.3:** (A) AFM imaging of $PilA_{19}$ fibers assembled *in vitro*. Inset shows single fibers and braided supramolecular structures with line scans used to determine the AFM height (red, single fiber; blue, braided fibers). Scale, 0.2 μm. (B-C) CD spectra of recombinant pili at pH 7 (B) and native pili under non-denaturing (red) or denaturing (8M urea; black) conditions (C).

**Electronic characterization of recombinant pili by scanning probe microscopy.**

We used CP-AFM to probe the conductivity of the recombinant fibers in reference to native pili purified to homogeneity and free of organic and inorganic cofactors, as reporter previously (13). The recombinant and native pili were deposited onto a freshly cleaved HOPG surface and imaged in tapping mode (Fig. 4.4A-B) before probing their transversal conductivity with a conductive AFM tip (Fig 4.4C-D). Current-voltage (*I-V*) curves of recombinant fibers probed in different regions were similar to

those collected for the native pili (Fig. 4.4A-B). From the inverse of the slope of the *I-V* curves at the low voltages that operate in biological systems (±100 mV) we calculated an average resistance for recombinant pili of ~900 MOhms, which is within the orders reported for the native wires under the same conditions (~ 925 MOhms). Furthermore, *I-V* curves collected for the recombinant and native pili by CP-AFM were similarly asymmetric, showing a rectification behavior such that more current was measured at negative voltages than at the same positive voltages (Fig 4.4C-D). Indeed, the average rectification scores (calculated as current at positive over negative voltage) for the recombinant pili were 0.51 at biologically relevant (±100 mV) voltages and 0.71 at higher (±600 mV) voltages, whereas the native fibers had rectification scores of 0.66 and 0.74, respectively. This rectifying behavior is consistent with a preferred path for electron transfer from the substrate to the tip (more current produced at negative voltages) at 100 mV or greater voltages.

We also used scanning tunneling microscopy (STM) to image the conductive recombinant pili (Fig. 4.4E). The higher spatial resolution of the STM technique compared to CP-AFM has helped resolve distinctive real-space electronic features along cell-associated (21) and purified (13) native pili. STM images of the recombinant fibers (Fig. 4.4E) show the distinctive beadlike structural features reported for the native pili (21). The bright spots are regions of the fiber with higher local electronic density of states, and, thus, supply more tunneling current, causing these regions to appear brighter in STM. Furthermore, these molecular substructures have periodicities that match well the periodic grooves and ridges that form on the surface of Type IV pili, as reported for the native fibers (21). The pili diameter estimated for the recombinant pilus

fibers (~5–7 nm) matches that reported for the native fibers prior to deconvoluting for the broadening tunneling effect caused by the tip when scanning a nanowire (13, 21). Thus, the STM studies confirm the presence of characteristic molecular and electronic features of the native pili in the recombinant pili.

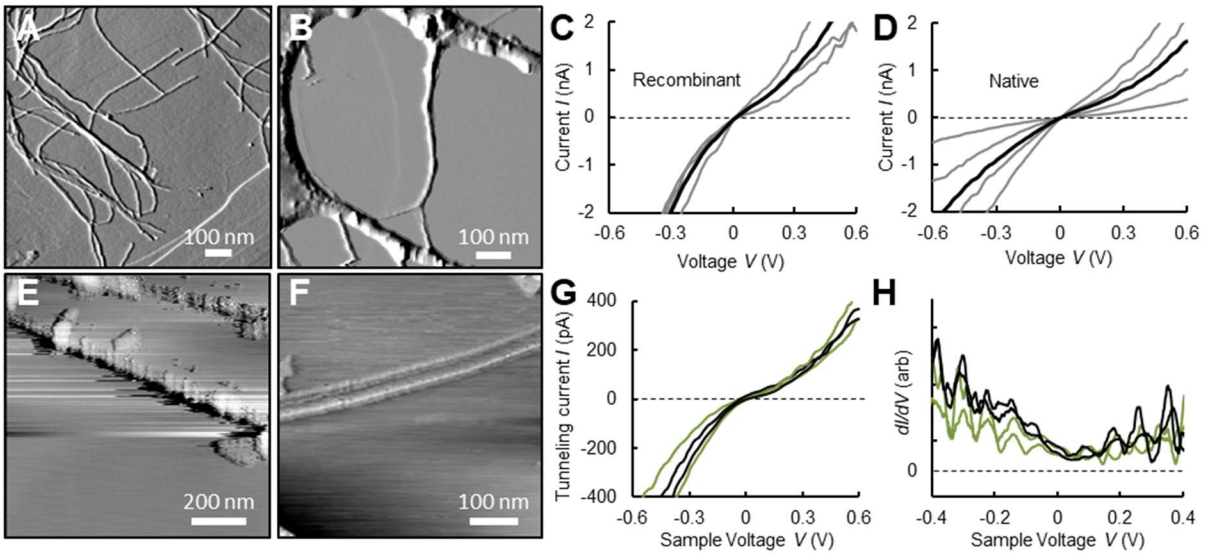


**Figure 4.4**: Electronic characterization of recombinant pili. (A-D) AFM amplitude image of recombinant (A) and native (B) pili on HOPG (scale bars, 200 nm) and (C, D) representative *I-V* curves of their respective CP-AFM transversal conductivity (average, in black). (E-H) Room temperature STM topographic image of untreated (E) or chemically-fixed (F) recombinant pili (0.5 V, 350 pA; scale bar, 100 nm) and average *I-V* tunneling spectra of 2 sequential measurements for each of two pilus regions in untreated (black) and fixed (green) samples (G). Panel H shows differential conductance (*dI/dV*) curves of the untreated and chemically treated pili, calculated as the numerical derivative of the *I-V* curves shown in **G**.

Also as reported previously (21), pili deposition on the HOPG surface improved with a chemical fixation step (Fig. 4.4F). This chemical treatment immobilizes more fibers onto the surface and removes non-pilus impurities during subsequent washing steps, a critical consideration for integration of recombinant pili in electronic devices. Chemically fixing the recombinant pili sample after deposition reduced tip instability and produced cleaner pilus topographies by STM (Fig. 4.4F). Chemical fixation did not affect the measured conductivity, producing similar *I*-*V* curves when probing fixed locations in untreated (hydrated) and chemically-treated recombinant pili while sweeping the voltage at ±600 mV (Fig. 4.4G). Furthermore, *I*-*V* curves from both samples had slopes greater than zero near the zero voltage, as reported for the native pili (13, 21). This result is more easily appreciated in plots of the differential conductance ($dI/dV$) versus the tip-sample bias voltage ($V$), which revealed in both the untreated and chemically-fixed recombinant pili electronic states at low voltages that never reach zero conductance (Fig. 4.4H). Hence, the recombinant pili, whether untreated or chemically fixed, are conductive even at low voltages (millivolts), as previously reported for native pili probed by STM spectroscopy in association with the cell or as purified fibers (13, 21). The STM differential conductance plots also revealed similar asymmetric conductance in hydrated and chemically fixed recombinant pili (Fig. 4.4H). The asymmetric dI/dV plots are consistent with a nanowire that favors current flow from negative to positive voltages, even at the low voltages (i.e., 100 mV) that operate in biological systems. Such rectifying behavior, against the natural dipole of the pilin's helix, reproduces well the conductance asymmetry reported for native pili (13, 21) and has been proposed to reflect the doping effect that aromatic contacts have in a hybrid path of conductivity that

alternates between charge hopping via aromatic residues and interchain tunneling (21, 31).

## Discussion

The availability of a recombinant production system for the production of easily manipulated peptides derived from the conductive pilin of *G. sulfurreducens* (31) permitted the production of high yields of an N-t truncated recombinant pilin ($PilA_{19}$) that removed the first 19 amino acids of the mature pilin peptide. The truncated peptide lacks amino acids required for biological assembly but retains the $\alpha$-helical conformation that is needed for pilin-pilin hydrophobic interactions and self-assembly (31). The truncation also preserves the charged residues that participate in the formation of salt bridges between neighboring peptides in the pilus fiber, which are necessary to bend the mid region of the pilins and promote the electronic coupling of aromatic amino acids in the pilus fiber (12, 13). Indeed, we were able to promote the self-assembly of the recombinant pilins into conductive fibers using an evaporation method that gradually increased molecular crowding and hydrophobicity in the peptide solution. The efficiency of the assembly depended on the availability of nucleation sites to initiate pilin assembly and the introduction of refeeding steps with mixing that promoted fiber growth from the nucleation sites. Silica nanoparticles functionalized with octadecane provided optimal seeding sites to initiate pilin assembly. The low cost and stability of silica nanoparticles and array of methods for the functionalization of their surface properties provides opportunities for optimizing and scaling up manufacturing protocols for protein nanowires using recombinant pilins as building blocks.

The recombinant pilus fibers also dispersed better in mild aqueous solutions compared to the native pili, which tend to form large supramolecular structures and bundles (6, 13). As illustrated by the less convoluted CD spectral data generated for the

recombinant pili (Fig. 4.3), their reduced aggregative nature enables structural studies not possible with the native pili. Structural information is particularly important to gain mechanistic insights into pilus conductance. For example, the inter-aromatic distances and aromatic dimer configurations predicted by computational models of the GS pili (12) are constructed using pilus fiber templates from bacteria such as *Neisseria gonorrhoeae*, which has a canonical pilin subunit with a large globular head at the C-t. There has been significant debate over the years as to the mechanism that allows the GS pili to conduct charges (12, 13, 24, 102, 103). Having similar molecular and electronic properties, reduced aggregation and higher biosynthetic yields, recombinant pili could provide critical structural information about how the pilus fibers transport charges.

The reduced aggregation and higher yields of the recombinant pili also facilitated deposition on HOPG and electronic imaging and probing by scanning probe methods (Fig. 4). However, it was important to optimize fiber formation during *in vitro* assembly through sequential refeeding steps and mixing to minimize the amount of unassembled pilins in solution, as these peptides also attached to the HOPG surface and form a monolayer with the mechanical and electronic properties reported for thiolated pilins (31). Thus, reproducible electronic probing of the recombinant fibers by CP-AFM required samples with high yields of fiber formation and low unassembled pilins but also the development of standard operating procedures that screened for fibers with adequate electrical contact with the underlying HOPG substrate. The method positions the conductive AFM tip on a hydrated fiber and generates *I-V* curves that inform of the transversal conductivity of the protein nanowire. As the measurement is sensitive to the

contact resistance between the pilus fibers and the underlying substrate, the slopes of the *I-V* curves are variable, particularly at the low voltages that operate in biologically systems (~ 100 mV). At this low voltage, for example, recombinant and native pili had a comparable average electrical resistance (~900 and 925 MOhms), but lows and highs ranged widely for both (~250 to 1600 MOhms) depending on the sample hydration and electrical contact with the HOPG substrate. By contrast, the STM technique imaged the fibers by their conductivity (Fig. 4.4), visually filtering out poorly contacting fibers during preliminary scans at a sample voltage of 500 mV to reveal only those with optimal electrical contact with the underlying substrate.

The STM measurements shown in Fig. 4.4 were performed in air, which causes tip instability and reduces imaging quality compared to the controlled vacuum environment used to image and probe native pili by STM (21). Yet despite this limitation, the STM topography of the recombinant pili reproduced the periodic topographic and electronic structure of native pili (21). The periodic substructures reflect changes in the material's response to the applied sample voltage in scans generated with a conductive tip of radius 28 ($\pm$10) nm, which is large enough to cover the roughly 10 nm periodic structures and can get close enough to the substrate to interact and broaden the tunneling effect. Such broadening effects are enhanced in nanowires, because of their tubular shape and reduced diameter. This effect leads to overestimation of the nanowire diameter, that can be corrected mathematically. Indeed, we estimated a diameter for recombinant pili of ~ 5-7 nm, as for the native pili, but the application of the deconvolution algorithm to the latter reduced the STM diameter to 2-3 nm, as estimated by AFM (21). Chemical fixation improved the quality of the images, consistent with an

improved deposition process that anchors the fibers more firmly to the surface and improves electrical contact. However, the chemical treatment did not affect the conductive properties of the fibers, a property that could be harnessed to integrate the recombinant protein nanowires with inorganic nanomaterials in electronic devices.

The CP-AFM and STM *I-V* curves also revealed rectifying behavior at biological (±100 mV) and higher (±600 mV) voltages (Fig. 4.4). This rectification likely does not reflect an alignment of aromatic amino acids within the cross section of the recombinant pili that promotes electron transfer in one direction, as was observed for planar assemblies (31). Instead, surface effects need to be considered. The small dimensions of the pili compared to the vast surface of the underlying HOPG substrate can affect the rates of charge injection and influence the directionality of electron flow. Thus, when the HOPG substrate is poised at a negative voltage the large surface area can efficiently inject charge into any portion of the fiber, allowing many electrons to travel to the relatively smaller tip placed on top and recording more current at negative voltages. By contrast, when the HOPG substrate is poised at a positive voltage, electrons are injected into the pili from the tip, which is interacting with the fiber over a much smaller area. In addition, the outer surface of the pili is decorated with large regions of negative charge (12), which could influence tip-pili interaction and make charge injection, and thus current flow, more difficult at positive bias voltages. The charge of the pili is less critical when electrons are injected into the fiber from the underlying HOPG substrate, as the fiber's extensive electrical contact can involve positively charged or non-charged pilus regions. An understanding of the transversal conductivity of the fibers is important for the potential integration of these protein nanowires into electronic devices.

## Conclusions

This work demonstrates the *in vitro* assembly of protein nanowires from truncated, mass produced GS pilins that exhibit similar conductive properties to wires isolated directly from *G. sulfurreducens*. These truncated pilins retain all the amino acid residues required for electron transfer, with STM revealing a periodic bead-like structure typical of GS pili indicative of molecular substructures critical to respiration driven electron transfer. There are numerous features of these protein nanowires that are technologically attractive, including ease of manipulation and production, conductivity, rectifying behavior, and chemical robustness. Like the native pili, the protein nanowires retain the surface motifs proposed to function as metal traps *in vivo*. These metal-binding regions bind toxic metals, such as the soluble uranyl cation, with high affinity and reductively precipitated it to a mineral phase that prevents its spread (6). Protein nanowires could potentially be integrated with electrodes and other materials to make nanobrushes for the reductive precipitation of toxic cationic metals such as cadmium and cobalt and for the reclamation of precious and rare metals such as silver and gold.

# Chapter 5.

# Conclusions and Future Directions

The goal of this dissertation was to develop *in vitro* platforms that harness the conductive properties of assemblies of GS pilins. This effort is important to advance mechanistic studies of electron transfer in the pilin peptides and the assemblies but also to exploit pilins as building blocks for bottom-up fabrication of novel biomaterials.

In chapter 2, I described team efforts to develop protocols for the recombinant production of GS pilin derivatives. One of the peptides generated via recombinant techniques carried an N-t truncation of 19 amino acids ($PilA_{19}$) needed for biological assembly. We constructed a thiolated version of this pilin to promote its attachment to gold electrodes and enable their self-assembly as well-ordered monolayers that recreated in a planar configuration the aromatic-rich and aromatic-free regions of the pilus fibers. I first characterized mechanical properties of the pilin coating by atomic force microscopy (AFM) that are important for future applications. Thus, I investigated the elastic deformation of the material and the forces that induce the transition to inelastic deformation, which informs about the structural transitions from helical to disordered conformations that can modulate electron transfer through the material. I linked the mechanical properties of the material to conductive signatures identified by CP-AFM. These studies unmasked a crossover event from a distance dependent tunneling regime through tightly packed helices void of aromatic residues to a weakly distance dependent regime closer to the electrode where aromatic residues promoted charge hopping. The conductivity measurements also unmasked rectifying behavior such that electron transfer was favored in the direction opposite to the enhanced helix dipole of the pilin, which is the biological direction of electron discharge. However, rectification was only observed at the low voltages (100 mV) that mark the differential

potential between inner membrane electron carriers and extracellular iron oxides during respiration. These results provide novel insights into electron transfer through pilin assemblies and set the foundation for the functionalization of electrodes for applications that harness the biocompatibility and conductivity of pilin coatings.

Pilin assemblies on gold electrodes are predicted to expose the pilus anionic metal traps to the analyte. In chapter 3, I used cyclic voltammetry to demonstrate the ability of the film to bind and reduce cationic metals such as ferric iron species that can serve as the natural electron acceptor for cellular respiration. As these redox species are soluble in both the oxidized and reduced form, I did not observe a significant contribution of the metal traps to current production. In fact, the cyclic voltammograms were consistent with a Nernstian, diffusion-limited redox system. By contrast, the divalent cobalt cation, $Co^{2+}$, underwent reductive mineralization to $Co^{0}$. Electrodeposition was observed in bare and pilin-functionalized gold electrodes, but slow scan rates unmask the contribution of the metal traps of the pilins to the kinetics of cobalt binding. The electrochemical characterization of the pilin films confirmed their ability to transfer electrons to redox metal species in the analyte but also demonstrated the suitability of the method to screen the spectrum of cationic metals that the pilin's metal traps can bind and reductively precipitate. Divalent cobalt is particularly significant because its has been assumed to be too toxic for biological reduction. However, the ability of the pilus metal traps to bind and possibly even reductively precipitate $Co^{2+}$ could provide a mechanism for its respiration and/or cellular protections, similarly to their role in uranium reduction. From an applied point of view, the immobilization of

cationic metals by pilin assemblies could be harnessed to coat other materials suitable for bioremediation and metal reclamation applications.

In chapter 4, I used the recombinant pilin $PilA_{19}$ as building block to manufacture protein nanowires. This bottom-up fabrication approach requires a hydrophobic nucleation site to initiate the orderly assembly of the pilins. Silica particles functionalized with octadecane were effective nucleators and could be used as supports to direct fiber formation in scaled applications due to their low cost and options for packing and functionalization. I also optimized the assembly of the pilins to promote fiber elongation, a step that could be manipulated to control the length of the nanowires for specific applications. I demonstrated the conductivity of the recombinant fibers using scanning probe methods (CP-AFM and STM) and calculated resistances comparable to those of the native pili. STM images of the recombinant pili also resolved electronic substructures along the fibers similar to those in native pili. I also showed that the conductivity of the recombinant pili is not affected by chemical fixation. This finding is important because chemical treatments can reduce the contact resistance between the pili and conductive substrates and are often employed during the fabrication of electronic devices. The recombinant production of pilin building blocks also enables the application of genetic engineering to modulate the properties of the protein nanowires and their metal traps. Functional tags such as the cysteine introduced in the thiolated pilins (chapters 2 and 3) enable the specific attachment of the biomaterial to gold but other chemistries can be enabled with other functional tags. The protein nanowires can also be engineered to modulate the affinity of the metal traps for specific metals. It may be possible to influence the conformation of the C-t region by addition of proline

residues or otherwise restricting the flexibility of the C-t region to accommodate more specific sizes of ligands. When combined with modified bottom-up protocols, nanobrushes could be developed with vertically grown nanowires for the detection and remediation of toxic cationic metals or reclamation of precious and rare cationic metals.

Taken together, the results presented in this dissertation set the foundation for devices that harness the power of GS pilins and conductive pili in electronics. Other applications can be envisioned. GS pilin peptides have the biocompatibility and conductivity that is needed to develop coatings that improve the osteointegration of orthopedic and dental titanium implants. Assemblies of recombinant pilins could be used as molecular surface coatings in cell adhesion assays and biosensors. Techniques are also available to print peptides onto substrates as arrays suitable for the screening of antibodies, the study of protein-protein interactions, and drug or small molecule discovery.

# APPENDIX

## Introduction

Assemblies attempted with buffer exchange columns dependent on non-hydrophobic chemistries, such as a column that relies on ionic interactions to retain the molecule of interest, dialysis, and lyophilization, resulted in no fiber formation. The need for a specific type of buffer exchange via a reverse phase C18 column for fiber formation suggested that an unknown chemical species is eluted from the column matrix that promotes efficient pili formation. As pilin-pilin interactions are hydrophobic in nature, we hypothesize that the column's eluent contains one or more hydrophobic species that could function as nucleator, that is, as hydrophobic seeding sites for pilin assembly. The C18 column used in these studies is packed with an amorphous silica matrix functionalized with octadecane, an alkane hydrocarbon with the chemical formula $CH_3(CH_2)_{16}CH_3$. The hydrophobic nature of octadecane prompted us to investigate its suitability as a nucleator during pilus formation. In principle, octadecane could be added to pilin solutions in specific concentrations for controlled nucleation, which could provide unprecedented levels of assembly control. Furthermore, octadecane is a versatile hydrocarbon commonly used as a phase change material to coat many surfaces (104), offering opportunities to functionalize substrates for scaled up assembly of recombinant pilins. To that end, I carried out experiments to investigate if octadecane eluting from the C18 column promotes pilin assembly.

## Materials and methods

### Ultraviolet-visible spectroscopy

The presence of non-peptide analytes in the C18 column eluent was evaluated by UV-vis spectroscopy (Shimadzu UV-2401PC spectrophotometer). A solution of elution buffer with various concentrations of dithiothreitol (DTT) was used to identify the DTT peak in the eluent.

### Effect of column washes in pilin assembly

The role of analytes eluting from the C18 column in promoting pilin assembly was tested in a modified purification protocol. A solution of $PilA_{19}$ peptides cleaved from a chitin binding column after DTT induction was loaded onto three separate reverse phase C18 columns. The concentration of DTT in the peptide solutions loaded onto each of the C18 columns was estimated to be ~50 mM. The C18 columns were washed with different volumes of $ddH_2O$, 1.7 column volumes (5 ml, standard protocol) or larger (3x and 6x) column volumes. After the washing step, the peptide retained in each of the C18 columns was eluted with 5 ml of assembly buffer. The peptide solution eluted from the column was analyzed by UV-vis spectroscopy, as described above. The pilin solutions collected from each of the columns were subjected to the standard evaporation-induced assembly process with or without sample mixing during refeeding steps. Fiber formation was assessed qualitatively after depositing the samples on a freshly cleaved HOPG substrate and imaging them with an AFM.

**Assembly experiments in the presence of octadecane**

The effect of octadecane as a nucleator of pilin assembly was investigated using a solution of purified $PilA_{19}$ (~ 8-9 mg of peptide) in elution buffer with the pH adjusted to 10 with 1 N NaOH. The peptide solution was loaded onto an Oasis Max™ disposable cartridge, which had been previously conditioned with $ddH_2O$. Buffer exchange was as described for the reverse phase C18 column, except that the column wash used 3 column volumes of 0.5% $NH_4OH$ and, when indicated, the matrix-bound peptide was eluted in assembly buffer with octadecane. The octadecane was first prepared fresh as a saturated methanol solution, serially diluted 1:100 in methanol and added to the assembly buffer solution at a 20% (v/v) final concentration (final dilution, 1:500). Pilin assembly was as described for the C18 column protocol.

## Results and discussion

### Spectroscopic characterization of C18 column eluent

We investigated the potential elution of a hydrophobe from the C18 matrix in a mock purification experiment without the peptide. Thus, the C18 column was treated with cleavage buffer without the peptide, the column was washed with 5 ml (1.7 column volumes of assembly buffer, as in the standard protocol), and the eluent was analyzed by UV-vis spectroscopy. The UV-vis spectrum revealed the expected DTT peak at ~203 nm, which we calculated to correspond to a concentration of ~ 1 mM from the original 50 mM loaded into the buffer (Fig. A1A). The spectrum also contains a peak at ~ 245 nm (Fig. A1A). It was possible to remove both peaks with extended washes (6 column volumes instead of 1.7) of the C18 column (Fig. A1A).

Octadecane does not absorb in the UV range (105) but functionalized silica particles absorb at ~ 245 nm (106, 107). Thus, the peak at ~ 245 nm likely corresponds to octadecane-bonded silica particles eluting from the column with the assembly buffer. It is interesting to note that silica is more soluble at alkaline pH, and the pilin solution loaded onto the C18 column (pH 9) could be promoting the release of silica particles from the matrix (108). This outcome suggests that pH control could be an important variable to test in future experiments. Alternatively, hydrophobic molecules may be tested as nucleators for pilin assembly. Below we describe octadecane as a potential candidate for controlled pilin nucleation.

### Octadecane as a nucleator during pilin assembly

We investigated the nucleator role of octadecane-coated particles by comparing the efficiency of pilin assembly using peptide samples purified with the standard (1.7x

column wash) or modified (6x column wash) protocols. After assembly, the samples were deposited onto a freshly cleaved HOPG substrate for AFM imaging and qualitative assessment of the efficiency of pili formation. Samples eluted with the standard protocol promoted fiber synthesis even in the absence of mixing (Fig. A1B). However, extending the washing step significantly reduced the efficiency of pili formation, as evidenced by the lack of fibers in most of the HOPG fields scanned (Fig. A1C).

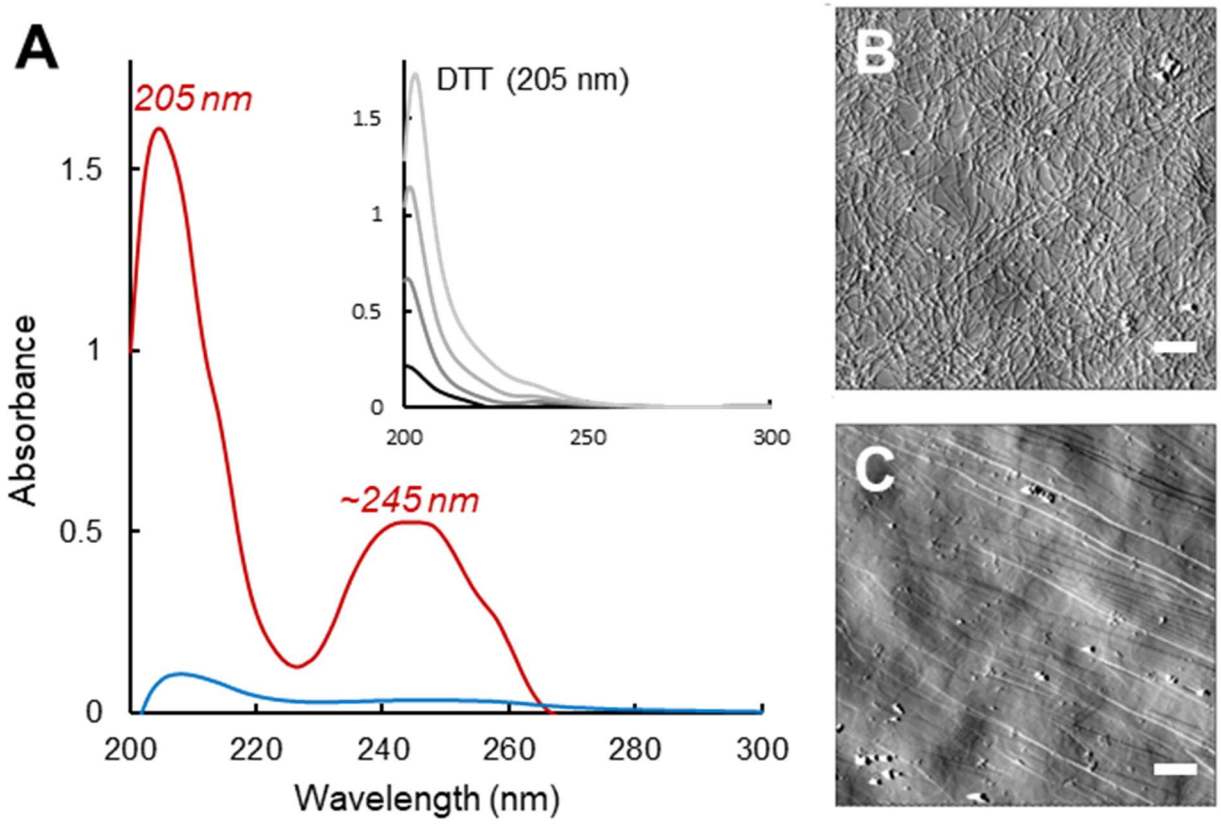


**Figure A1:** UV-Vis of C18 column eluent and assembly of pili. UV-Vis spectroscopy (A) of the eluent (in 80% acetonitrile 20% methanol) of a blank reverse phase C18 column with 1.7x (red) and 6x (blue) wash steps with a DTT standard curve inset. Assemblies of pilin samples subjected to 1.7x (B) washes and 6x (C) washes.

Mixing during assembly, which helps with fiber elongation from preformed nucleation sites, had a positive effect on pili formation in samples prepared with the standard protocol, but failed to stimulate fiber formation in the samples subjected to the extended washing (6x volume) step (Fig. A2C). Instead, mixing only stimulated the formation of heterogenous assemblies comprised of amorphous structures and short, thick fibers rather than the thin and long fibers generated in the presence of the octadecane-coated silica particles (Fig. A2). Interestingly, samples prepared with an intermediate washing step (3x column volumes instead of 1.7x or 6x) also promoted efficient fiber formation provided samples were mixed during assembly (Fig. A2B). Thus, this protocol (3x washing step, mixing), while reducing the amount of nucleator eluting from the C18 column, does not compromise the efficiency of pili formation. This point is important because hydrophobic molecules can adsorb onto conductive substrates such as HOPG and prevent conductivity measurements of the pili samples.

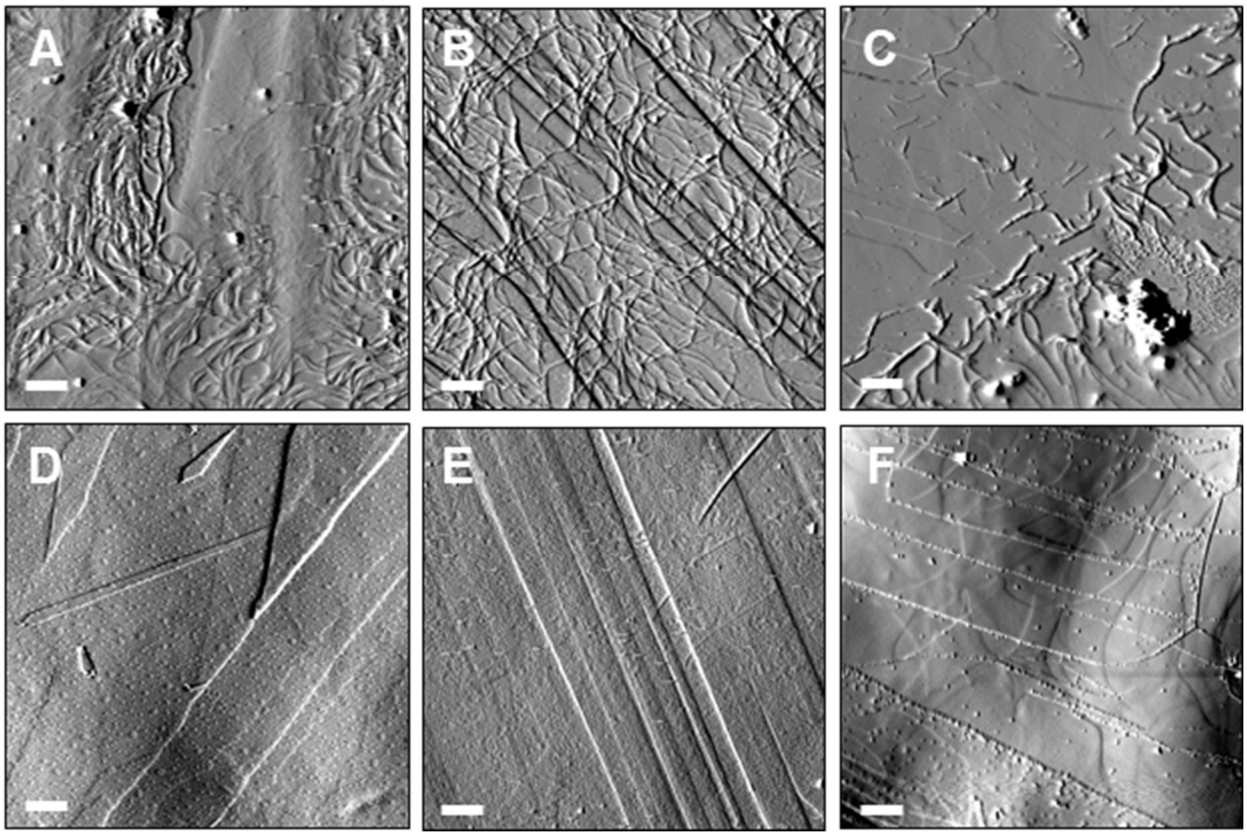


**Figure A2**: Effect of wash steps on assembly. Assemblies from peptide-containing (A-C) and blank (D-E) C18 columns subjected to 1.7x (A, D), 3x (B, E), and 6x (C, F) wash steps

.

These experiments indicate that octadecane in the silica coatings serves as hydrophobic seeding sites for the nucleation of pilins, a required step prior to fiber elongation. We demonstrated the induction of fiber formation in experiments that replaced the C18 column with an Oasis Max$^{TM}$ cartridge. This column is packed with a non-silanol polymeric sorbent functionalized with a quaternary amine and, therefore, does not release a hydrophobe that could promote pilin nucleation (Fig. A3). Consistently, buffer exchange of pilin samples using the Oasis Max$^{TM}$ column prevents pilin assembly (Fig. A3). However, supplementing the assembly buffer with octadecane

provided a nucleator for pilin assembly and permitted the formation of pilus fibers (Fig. A3). These results support the initial hypothesis that octadecane eluted as coated silica particles from the C18 column provided nucleation sites to stimulate pili-pilin assembly and fiber formation.

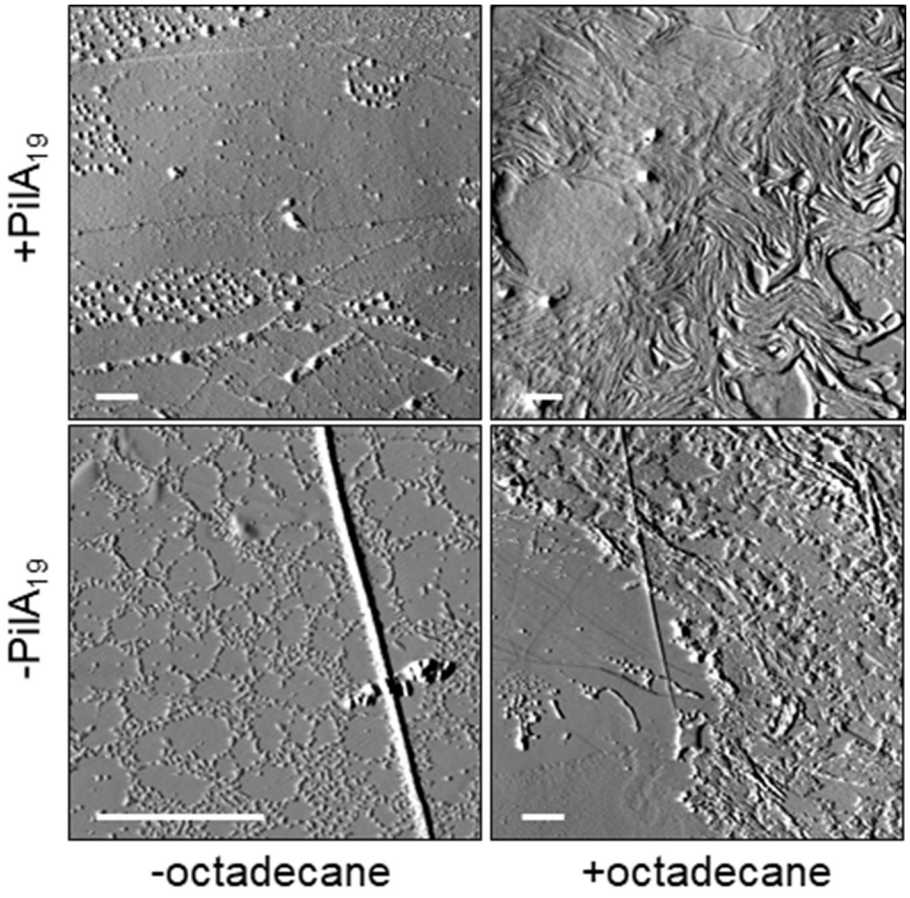


**Figure A3:** Assemblies from Oasis max buffer exchange columns. Assembled samples with and without peptide buffer exchanged with an Oasis Max cartridge supplemented with and without octadecane.

# REFERENCES

# REFERENCES


1. Butler JE, Young ND, & Lovley DR (2010) Evolution of electron transfer out of the cell: comparative genomics of six *Geobacter* genomes. *BMC Genomics* 11:40.

2. Reguera G (2018) Microbial nanowires and electroactive biofilms. *FEMS Microbiol. Ecol.*:fiy086-fiy086.

3. Holmes DE, Dang Y, Walker DJF, & Lovley DR (2016) The electrically conductive pili of Geobacter species are a recently evolved feature for extracellular electron transfer. *Microb Genomics* 2(8).

4. Reguera G*, et al.* (2005) Extracellular electron transfer via microbial nanowires. *Nature* 435(7045):1098-1101.

5. Speers AM, Schindler BD, Hwang J, Genc A, & Reguera G (2016) Genetic identification of a PilT motor in *Geobacter sulfurreducens* reveals a role for pilus retraction in extracellular electron transfer. *Front. Microbiol.* 7:1578.

6. Cologgi DL, Lampa-Pastirk S, Speers AM, Kelly SD, & Reguera G (2011) Extracellular reduction of uranium via *Geobacter* conductive pili as a protective cellular mechanism. *Proc. Natl. Acad. Sci. USA* 108(37):15248-15252.

7. Esteve-Nunez A, Sosnik J, Visconti P, & Lovley DR (2008) Fluorescent properties of *c*-type cytochromes reveal their potential role as an extracytoplasmic electron sink in *Geobacter sulfurreducens*. *Environ. Microbiol.* 10(2):497-505.

8. Reguera G (2018) Harnessing the power of microbial nanowires. *Microb. Biotechnol.* 94:fiy086.

9. Steidl R, Lampa-Pastirk S, & Reguera G (2016) Mechanistic stratification in electroactive biofilms of *Geobacter sulfurreducens* mediated by pilus nanowires. *Nature Comm.* 7:12217.

10. Reardon PN & Mueller KT (2013) Structure of the type IVa major pilin from the electrically conductive bacterial nanowires of *Geobacter sulfurreducens*. *J. Biol. Chem.* 288(41):29260-29266.

11. Feliciano GT, da Silva AJ, Reguera G, & Artacho E (2012) Molecular and electronic structure of the peptide subunit of Geobacter sulfurreducens conductive pili from first principles. *J Phys Chem A* 116(30):8023-8030.

12. Feliciano GT, Steidl RJ, & Reguera G (2015) Structural and functional insights into the conductive pili of *Geobacter sulfurreducens* revealed in molecular dynamics simulations. *Phys. Chem. Chem. Phys.* 17(34):22217-22226.

13. Lampa-Pastirk S*, et al.* (2016) Thermally activated charge transport in microbial protein nanowires. *Sci Rep-Uk* 6.

14. El-Naggar MY*, et al.* (2010) Electrical transport along bacterial nanowires from *Shewanella oneidensis* MR-1. *Proc. Natl. Acad. Sci. USA* 107(42):18127-18131.

15. Gorby YA*, et al.* (2006) Electrically conductive bacterial nanowires produced by *Shewanella oneidensis* strain MR-1 and other microorganisms. *Proc. Natl. Acad. Sci. USA* 103(30):11358-11363.

16. Kotloski NJ & Gralnick JA (2013) Flavin electron shuttles dominate extracellular electron transfer by *Shewanella oneidensis*. *Mbio* 4(1):e00553-00512.

17. Pirbadian S*, et al.* (2014) *Shewanella oneidensis* MR-1 nanowires are outer membrane and periplasmic extensions of the extracellular electron transport components. *Proc. Natl. Acad. Sc.i USA* 111(35):12883-12888.

18. Subramanian P, Pirbadian S, El-Naggar MY, & Jensen GJ (2018) Ultrastructure of *Shewanella oneidensis* MR-1 nanowires revealed by electron cryotomography. *Proc. Natl. Acad. Sc.i USA* 115(14):E3246-E3255.

19. Long YT, Abu-Irhayem E, & Kraatz HB (2005) Peptide electron transfer: more questions than answers. *Chem. Eur. J.* 11(18):5186-5194.

20. Shin Y-gK, Newton MD, & Isied SS (2003) Distance Dependence of Electron Transfer Across Peptides with Different Secondary Structures: The Role of Peptide Energetics and Electronic Coupling. *J. Am. Chem. Soc.* 125(13):3722-3732.

21. Veazey JP, Reguera G, & Tessmer SH (2011) Electronic properties of conductive pili of the metal-reducing bacterium *Geobacter sulfurreducens* probed by scanning tunneling microscopy. *Phys. Rev. E* 84(6):060901.

22. Craig L*, et al.* (2006) Type IV pilus structure by cryo-electron microscopy and crystallography: implications for pilus assembly and functions. *Mol. Cell* 23(5):651-662.

23. Malvankar NS*, et al.* (2011) Tunable metallic-like conductivity in microbial nanowire networks. *Nat. Nanotechnol.* 6(9):573-579.

24. Strycharz-Glaven SM & Tender LM (2012) Reply to the 'Comment on "On electrical conductivity of microbial nanowires and biofilms"' by N. S. Malvankar, M. T. Tuominen and D. R. Lovley, Energy Environ. Sci., 2012, 5, DOI: 10.1039/c2ee02613a. *Energ Environ Sci* 5(3):6250-6255.

25. Yates MD*, et al.* (2016) Measuring conductivity of living *Geobacter sulfurreducens* biofilms. *Nat. Nanotechnol.* 11(11):910-913.

26. Ing NL, Nusca TD, & Hochbaum AI (2017) *Geobacter sulfurreducens* pili support ohmic electronic conduction in aqueous solution. *Phys. Chem. Chem. Phys.* 19(32):21791-21799.

27. Polizzi NF, Skourtis SS, & Beratan DN (2012) Physical constraints on charge transport through bacterial nanowires. *Faraday Discussions* 155:43-114.

28. Bonanni PS, Massazza D, & Busalmen JP (2013) Stepping stones in the electron transport from cells to electrodes in Geobacter sulfurreducens biofilms. *Phys Chem Chem Phys* 15(25):10300-10306.

29. Xiao K*, et al.* (2016) Low Energy Atomic Models Suggesting a Pilus Structure that could Account for Electrical Conductivity of Geobacter sulfurreducens Pili. *Sci Rep-Uk* 6.

30. Bredas JL, Calbert JP, da Silva Filho DA, & Cornil J (2002) Organic semiconductors: a theoretical characterization of the basic parameters governing charge transport. *Proc Natl Acad Sci U S A* 99(9):5804-5809.

31. Cosert KM, Steidl RJ, Castro-Forero A, Worden RM, & Reguera G (2017) Electronic characterization of *Geobacter sulfurreducens* pilins in self-assembled monolayers unmasks tunnelling and hopping conduction pathways. *Phys. Chem. Chem. Phys.* 19(18):11163-11172.

32. Hau HH, Gilbert A, Coursolle D, & Gralnick JA (2008) Mechanism and consequences of anaerobic respiration of cobalt by *Shewanella oneidensis* strain MR-1. *Appl. Environ. Microbiol.* 74(22):6880-6886.

33. Elgrishi N*, et al.* (2018) A practical beginner's guide to Cyclic Voltammetry. *J. Chem. Educ.* 95(2):197-206.

34. Lane N & Martin WF (2012) The origin of membrane bioenergetics. *Cell* 151(7):1406-1416.

35. Shi L*, et al.* (2016) Extracellular electron transfer mechanisms between microorganisms and minerals. *Nat. Rev. Microbiol.* 14(10):651-662.

36. Cologgi DL, Speers AM, Bullard BA, Kelly SD, & Reguera G (2014) Enhanced uranium immobilization and reduction by *Geobacter sulfurreducens* biofilms. *Appl. Environ. Microbiol.* 80(21):6638-6646.

37. Galoppini E & Fox MA (1996) Effect of the electric field generated by the helix dipole on photoinduced intramolecular electron transfer in dichromophoric α-helical peptides. *J. Am. Chem. Soc.* 118(9):2299-2300.

38. Morita T & Kimura S (2003) Long-range electron transfer over 4 nm governed by an inelastic hopping mechanism in self-assembled monolayers of helical peptides. *J Am Chem Soc* 125(29):8732-8733.

39. Petrov EG, Shevchenko YV, Teslenko VI, & May V (2001) Nonadiabatic donor-acceptor electron transfer mediated by a molecular bridge: A unified theoretical description of the superexchange and hopping mechanism. *J. Chem. Phys.* 115(15):7107-7122.

40. Beratan DN, Betts JN, & Onuchic JN (1991) Protein electron transfer rates set by the bridging secondary and tertiary structure. *Science* 252(5010):1285-1288.

41. Cordes M & Giese B (2009) Electron transfer in peptides and proteins. *Chem.' Soc. Rev.* 38(4):892-901.

42. Pawlowski J, Juhaniewicz J, Tymecka D, & Sek S (2012) Electron transfer across α-helical peptide monolayers: importance of interchain coupling. *Langmuir* 28(50):17287-17294.

43. Gray HB & Winkler JR (2003) Electron tunneling through proteins. *Q. Rev. Biophys.* 36(3):341-372.

44. Kai M, Takeda K, Morita T, & Kimura S (2008) Distance dependence of long-range electron transfer through helical peptides. *J. Pept. Sc.* 14(2):192-202.

45. Lauz M, Eckhardt S, Fromm KM, & Giese B (2012) The influence of dipole moments on the mechanism of electron transfer through helical peptides. *Phys. Chem. Chem. Phys.* 14(40):13785-13788.

46. Gao J*, et al.* (2011) Electron transfer in peptides: the influence of charged amino acids. *Angew. Chem. Int. Ed. Engl.* 50(8):1926-1930.

47. Coppi MV, Leang C, Sandler SJ, & Lovley DR (2001) Development of a genetic system for *Geobacter sulfurreducens*. *Appl. Environ. Microbiol.* 67(7):3180-3187.

48. Liu GY, Xu S, & Qian YL (2000) Nanofabrication of self-assembled monolayers using scanning probe lithography. *Accounts Chem Res* 33(7):457-466.

49. Johnson KL, Kendall K, & Roberts AD (1971) Surface energy and the contact of elastic solids. *Proc. R. Soc. London. Ser. A* 324(1558):301-313.

50. Kharakoz DP (2000) Protein compressibility, dynamics, and pressure. *Biophys. J.* 79(1):511-525.

51. Hagen J, Burmeister F, Fromm A, Manns P, & Kleer G (2009) Iridium coatings with titanium sub-layer deposited by RF magnetron sputtering: Mechanical properties and contact behavior with RoHS-compliant glass melt. *Plasma Process Polym* 6:S678-S683.

52. Ptak A*, et al.* (2001) Modified atomic force microscope applied to the measurement of elastic modulus for a single peptide molecule. *J. Appl. Phys.* 90(6):3095-3099.

53. Rosano GL & Ceccarelli EA (2014) Recombinant protein expression in *Escherichia coli:* advances and challenges. *Front. Microbiol.* 5:172.

54. Audette GF, van Schaik EJ, Hazes B, & Irvin RT (2004) DNA-binding protein nanotubes: learning from Nature's nanotech examples. *Nano Lett.* 4(10):1897-1902.

55. Kyte J & Doolittle RF (1982) A simple method for displaying the hydropathic character of a protein. *J. Mol. Biol.* 157(1):105-132.

56. Chong SR*, et al.* (1997) Single-column purification of free recombinant proteins using a self-cleavable affinity tag derived from a protein splicing element. *Gene* 192(2):271-281.

57. Fisher LE & Engelman DM (2001) High-yield synthesis and purification of an alpha-helical transmembrane domain. *Anal. Biochem.* 293(1):102-108.

58. Johannsmann D, Reviakine I, & Richter RP (2009) Dissipation in films of adsorbed nanospheres studied by quartz crystal microbalance (QCM). *Anal. Chem.* 81(19):8167-8176.

59. Kotarek JA, Johnson KC, & Moss MA (2008) Quartz crystal microbalance analysis of growth kinetics for aggregation intermediates of the amyloid-beta protein. *Anal. Biochem.* 378(1):15-24.

60. Agonafer DD, Chainani E, Oruc ME, Lee KS, & Shannon MA (2013) Study of insulating properties of alkanethiol self-assembled monolayers formed under prolonged incubation using electrochemical impedance spectroscopy. *J. Nanotechnol. Eng. Med.* 3(3):031006-031006-031008.

61. Zhuravel R*, et al.* (2016) Atomic force microscopy characterization of kinase-mediated phosphorylation of a peptide monolayer. *Sci. Rep.* 6:36793.

62. Sek S, Swiatek K, & Misicka A (2005) Electrical behavior of molecular junctions incorporating alpha-helical peptide. *J. Phys. Chem. B* 109(49):23121-23124.

63. Arikuma Y, Takeda K, Morita T, Ohmae M, & Kimura S (2009) Linker effects on monolayer formation and long-range electron transfer in helical peptide monolayers. *J. Phys. Chem. B* 113(18):6256-6266.

64. Sek S, Misicka A, Swiatek K, & Maicka E (2006) Conductance of α-helical peptides trapped within molecular junctions. *J. Phys. Chem. B* 110(39):19671-19677.

65. Takeda K, Morita T, & Kimura S (2008) Effects of monolayer structures on long-range electron transfer in helical peptide monolayer. *J. Phys. Chem. B* 112(40):12840-12850.

66. Xiao X, Xu B, & Tao N (2004) Conductance titration of single-peptide molecules. *J. Am. Chem. Soc.* 126(17):5370-5371.

67. Gray HB & Winkler JR (2005) Long-range electron transfer. *Proc. Natl. Acad. Sci .USA* 102(10):3534-3539.

68. Slowinski K, Chamberlain RV, Miller CJ, & Majda M (1997) Through-bond and chain-to-chain coupling. Two pathways in electron tunneling through liquid alkanethiol monolayers on mercury electrodes. *J. Am. Chem. Soc.* 119(49):11910-11919.

69. Guo C*, et al.* (2016) Tuning electronic transport via hepta-alanine peptides junction by tryptophan doping. *Proc. Natl. Acad. Sci. USA* 113(39):10785-10790.

70. Lu Q*, et al.* (2009) From tunneling to hopping: A comprehensive investigation of charge tansport mechanism in molecular junctions based on oligo(p-phenylene ethynylene)s. *Acs Nano* 3(12):3861-3868.

71. Caccavo F, Jr.*, et al.* (1994) *Geobacter sulfurreducens* sp. nov., a hydrogen- and acetate-oxidizing dissimilatory metal-reducing microorganism. *Appl. Environ. Microbiol.* 60(10):3752-3759.

72. Alleman KS, Weber K, & Creager SE (1996) Electrochemical Rectification at a Monolayer-Modified Electrode. *The Journal of Physical Chemistry* 100(42):17050-17058.

73. Ganesh V, Pal SK, Kumar S, & Lakshminarayanan V (2006) Self-assembled monolayers (SAMs) of alkoxycyanobiphenyl thiols on gold--a study of electron transfer reaction using cyclic voltammetry and electrochemical impedance spectroscopy. *J Colloid Interface Sci* 296(1):195-203.

74. Brownson DAC & Banks CE (2014) Interpreting Electrochemistry. *The Handbook of Graphene Electrochemistry*, eds Brownson DAC & Banks CE (Springer London, London), pp 23-77.

75. Love JC, Estroff LA, Kriebel JK, Nuzzo RG, & Whitesides GM (2005) Self-assembled monolayers of thiolates on metals as a form of nanotechnology. *Chem Rev* 105(4):1103-1169.

76. Pletcher D, Greff R, Peat R, Peter LM, & Robinson J (2010) 9 - Electrocrystallisation. *Instrumental Methods in Electrochemistry*, eds Pletcher D, Greff R, Peat R, Peter LM, & Robinson J (Woodhead Publishing), pp 283-316.

77. Zafferoni C*, et al.* (2015) Synergy of Cobalt and Silver Microparticles Electrodeposited on Glassy Carbon for the Electrocatalysis of the Oxygen Reduction Reaction: An Electrochemical Investigation. *Molecules* 20(8):14386-14401.

78. Soto AB, Arce EM, PalomarPardave M, & Gonzalez I (1996) Electrochemical nucleation of cobalt onto glassy carbon electrode from ammonium chloride solutions. *Electrochim Acta* 41(16):2647-2655.

79. Fletcher S (1983) Some New Formulas Applicable to Electrochemical Nucleation-Growth-Collision. *Electrochim Acta* 28(7):917-923.

80. Mendoza-Huizar LH, Robles J, & Palomar-Pardave M (2002) Nucleation and growth of cobalt onto different substrates Part I. Underpotential deposition onto a gold electrode. *J Electroanal Chem* 521(1-2):95-106.

81. Holzle MH, Zwing V, & Kolb DM (1995) The Influence of Steps on the Deposition of Cu onto Au(111). *Electrochim Acta* 40(10):1237-1247.

82. Mendoza-Huizar LH, Robles J, & Palomar-Pardave M (2003) Nucleation and growth of cobalt onto different substrates Part II. The upd-opd transition onto a gold electrode. *J Electroanal Chem* 545:39-45.

83. Palomar-Pardave M, Gonzalez I, Soto AB, & Arce EM (1998) Influence of the coordination sphere on the mechanism of cobalt nucleation onto glassy carbon. *J Electroanal Chem* 443(1):125-136.

84. Mendoza-Huizar LH, Palomar-Pardave M, & Robles J (2001) Quantum chemical study of the electrochemical reduction of the [Co(H2O)(6)](2+) and [Co(NH3)(5)(H2O)](2+) ions. *Electrochim Acta* 46(18):2749-2755.

85. Craig L & Li J (2008) Type IV pili: paradoxes in form and function. *Curr. Opin. Struct. Biol.* 18(2):267-277.

86. Greenfield NJ (2007) Using circular dichroism spectra to estimate protein secondary structure. *Nat. Protocols* 1(6):2876-2890.

87. Mihalyi E (1968) Numerical values of the absorbances of the aromatic amino acids in acid, neutral, and alkaline solutions. *Journal of Chemical & Engineering Data* 13(2):179-182.

88. Wallace BA & Janes RW eds (2009) *Modern technices for circular dichroism and synchrotron radiation circular dichroism spectroscopy* (IOS Press Amsterdam), p 256.

89. Whitmore L & Wallace BA (2004) DICHROWEB, an online server for protein secondary structure analyses from circular dichroism spectroscopic data. *Nucleic Acids Research* 32(suppl 2):W668-W673.

90. Whitmore L & Wallace BA (2008) Protein secondary structure analyses from circular dichroism spectroscopy: Methods and reference databases. *Biopolymers* 89(5):392-400.

91. Provencher SW & Gloeckner J (1981) Estimation of globular protein secondary structure from circular dichroism. *Biochemistry* 20(1):33-37.

92. van Stokkum IHM, Spoelder HJW, Bloemendal M, van Grondelle R, & Groen FCA (1990) Estimation of protein secondary structure and error analysis from circular dichroism spectra. *Analytical Biochemistry* 191(1):110-118.

93. Sreerama N & Woody RW (2000) Estimation of Protein Secondary Structure from Circular Dichroism Spectra: Comparison of CONTIN, SELCON, and CDSSTR Methods with an Expanded Reference Set. *Analytical Biochemistry* 287(2):252-260.

94. Venyaminov S, Baikalov IA, Shen ZM, Wu CS, & Yang JT (1993) Circular dichroic analysis of denatured proteins: inclusion of denatured proteins in the reference set. *Anal. Biochem.* 214(1):17-24.

95. Holzwarth G & Doty P (1965) The ultraviolet circular dichroism of polypeptides. *J. Am. Chem. Soc.* 87:218-228.

96. Montserret R, McLeish MJ, Böckmann A, Geourjon C, & Penin F (2000) Involvement of Electrostatic Interactions in the Mechanism of Peptide Folding Induced by Sodium Dodecyl Sulfate Binding‚Ä†,,Ä°. *Biochemistry* 39(29):8362-8373.

97. Hjelmeland LM, Chrambach A, & William BJ (1984) [16] Solubilization of functional membrane proteins. *Methods in Enzymology*, (Academic Press), Vol Volume 104, pp 305-318.

98. le Maire M, Champeil P, & Møller JV (2000) Interaction of membrane proteins and lipids with solubilizing detergents. *Biochimica et Biophysica Acta (BBA) - Biomembranes* 1508(1-2):86-111.

99. Cooper TM & Woody RW (1990) The effect of conformation on the CD of interacting helices: a theoretical study of tropomyosin. *Biopolymers* 30(7-8):657-676.

100. Albert JS & Hamilton AD (1995) Stabilization of helical domains in short peptides using hydrophobic interactions. *Biochemistry-Us* 34(3):984-990.

101. Li J, Egelman EH, & Craig L (2012) Structure of the *Vibrio cholerae* Type IVb pilus and stability comparison with the *Neisseria gonorrhoeae* type IVa pilus. *J. Mol. Biol.* 418(1-2):47-64.

102. Strycharz-Glaven SM, Snider RM, Guiseppi-Elie A, & Tender LM (2011) On the electrical conductivity of microbial nanowires and biofilms. *Energ Environ Sci* 4(11):4366-4379.

103. Malvankar NS, Tuominen MT, & Lovley DR (2012) Comment on "On electrical conductivity of microbial nanowires and biofilms" by S. M. Strycharz-Glaven, R. M. Snider, A. Guiseppi-Elie and L. M. Tender, Energy Environ. Sci., 2011, 4, 4366. *Energ Environ Sci* 5(3):6247-6249.

104. Yilbas BS, Ali H, Al-Sharafi A, & Al-Aqeeli N (2018) Droplet dynamics on a hydrophobic surface coated with N-octadecane phase change material. *Colloid Surface A* 546:28-39.

105. Hintze PE, Buhler CR, Schuerger AC, Calle LM, & Calle CI (2010) Alteration of five organic compounds by glow discharge plasma and UV light under simulated Mars conditions. *Icarus* 208(2):749-757.

106. Abdelghany AM (2015) Modeling, Structural, and Spectroscopic Studies of Cobalt-doped Lithium Phosphate Glasses and Effect of Gamma Irradiation. *Spectrosc Lett* 48(9):623-630.

107. Saito M*, et al.* (2014) Spatial correlation between chemical and topological defects in vitreous silica: UV-resonance Raman study. *J Chem Phys* 140(24).

108. Eiblmeier J, Kellermeier M, Rengstl D, Garcia-Ruiz JM, & Kunz W (2013) Effect of bulk pH and supersaturation on the growth behavior of silica biomorphs in alkaline solutions. *Crystengcomm* 15(1):43-53.